

Attoseconds and the exascale: on laser plasma surface interactions



Robin Timmis
Your College
University of Oxford

A thesis submitted for the degree of
Doctor of Philosophy

Michaelmas 2014

Acknowledgements

Personal Institutional

The author thanks the Norreys Research Group, Prof. Philip Burrows and Dr. Qingsong Feng for useful discussions, the SMILEI consortium and the ARCHER2 support team. The authors also acknowledge the support of AWE plc, UKRI-EPSRC and the Oxford-Berman Graduate Scholarship program. This work used the ARCHER2 UK National Supercomputing Service (<https://www.archer2.ac.uk>) under project e674 of URKI-EPSRC grant no. EP/R029148/1 and UKRI-STFC grant no. ST/V001655/1.

Abstract

The commissioning of multi-petawatt class laser facilities around the world is gathering pace. One of the primary motivations for these investments is the acceleration of high-quality, low-emittance electron bunches. Here we explore the interaction of a high-intensity femtosecond laser pulse with a mass-limited dense target to produce MeV attosecond electron bunches in transmission and confirm with three-dimensional simulation that such bunches have low emittance and nano-Coulomb charge. We then perform a large parameter scan from non-relativistic laser intensities to the laser-QED regime and from the critical plasma density to beyond solid density to demonstrate that the electron bunch energies and the laser pulse energy absorption into the plasma can be quantitatively described via the Zero Vector Potential mechanism. These results have wide-ranging implications for future particle accelerator science and associated technologies.

Contents

List of Figures	ix
A List of Symbols and Abbreviations	xi
1 Introduction	1
1.1 High-energy-density physics	1
1.2 Electromagnetism fundamentals	4
1.3 The definition of a plasma	5
1.3.1 The Debye length	6
1.3.2 The plasma parameter	7
1.3.3 Collisionality and the plasma frequency	7
1.4 The Lawson-Woodward theorem	9
1.5 Laser-solid density plasma linear interaction	10
1.6 Relativity	11
1.6.1 Ultra-relativistic similarity theory	12
1.6.2 Relativistic lasers and plasmas	14
1.6.3 Conservation of generalised transverse momentum	15
1.7 QED effects	16
1.7.1 High-energy photon emission and radiation reaction	16
1.7.2 Multi-photon Breit-Wheeler pair production	17
1.8 Simulating the interaction	18
1.8.1 Supercomputing resources	18
1.8.2 Particle-In-Cell codes	18
2 The Zero Vector Potential Absorption Mechanism	27
2.1 Motivations and an overview	27
2.2 Introduction	29
2.2.1 ZVP electron bunch energies	36
2.2.2 ZVP bunches oblique incidence scaling and internal bunch structure	38
2.2.3 Defining characteristics of the ZVP mechanism	41
2.3 Numerical simulations of the ZVP mechanism	42

2.3.1	The ZVP mechanism in 3D3V	42
2.4	The ZVP electron bunch	49
2.4.1	Energy absorption in the ZVP regime	58
2.4.2	Unpacking the QED effects of figure 2.11	60
2.4.3	Errors	62
2.5	Planned future work	63
2.6	Conclusions	67
3	Miscellaneous notes	69
3.1	To do	69
3.2	ORION experiment	71
3.2.1	Frames of reference	71
3.2.2	ORION interaction geometry	75
3.2.3	Condition on validity of hole boring expression	77
3.3	Thinking about the ZVP calculation	78
3.4	Things I may want to include or random notes	79
Appendices		
A	General plasma physics	83
A.1	Lorentz transformations of electromagnetic fields	83
A.2	The headlight effect	84
A.3	Geometric transverse emittance	84
B	PIC simulations	87
B.1	Convergence of 3D PIC simulations	87

List of Figures

1.1	Laser systems across the globe, both commissioned and theorised.	2
1.2	Diagram to illustrate the derivation of the plasma frequency.	8
1.3	A schematic of the PIC code loop and the algorithms performed.	19
1.4	A representation of the staggered Yee grid.	20
1.5	Smilei simulation box decomposition into cells, patches and MPI patch collections.	23
1.6	Representation of the interaction of the ARCHER2 hardware and software components when running Smilei.	24
2.1	Diagram of a p-polarised laser pulse incident at angle θ specularly reflected from a solid density plasma.	31
2.2	Diagram of a <i>p</i> -polarised laser pulse incident on an ablating overdense plasma.	33
2.3	Simulation results from a 3D Particle-In-Cell (PIC) simulation of the Zero Vector Potential (ZVP) mechanism.	43
2.4	Propagation of zeroes through the ablating ZVP electron bunch.	46
2.5	Electron dynamics in 3D PIC simulation for both linear and circularly polarised relativistic laser pulses.	47
2.6	The Fourier transform of the reflected laser pulse in 3D PIC simulations.	48
2.7	2D PIC simulation results qualitatively describing typical mass-limited ZVP electron bunch structure.	51
2.8	Energy spectra for mass-limited electron bunches formed via linearly and circularly polarised laser pulses.	52
2.9	Mean mass-limited ZVP electron bunch normalised kinetic energies extracted from 2D PIC simulations.	54
2.10	The relative errors for each mean energy data point compared to figure 2.9.	57
2.11	Peak instantaneous bulk electron bunch total energy escaping to the plasma bulk rear.	58
2.12	An exploration of ZVP 2D PIC simulation stability.	63
2.13	Planned GEMINI-PW experimental setup for the measurement of ZVP electron bunches.	64

3.1	72
3.2	ORION target chamber geometry showing the location of the target (TCC) and OHREX spectrometer and the green (SP1) and infra-red (SP2) beamlines and their corresponding polarisations.	75
B.1	Comparison between the initial 3D simulation and a lower resolution version.	88

A List of Symbols and Abbreviations

Note All quantities are defined in SI units unless otherwise specified throughout the thesis.

α	Twiss parameter = $-\frac{\langle x_i x'_i \rangle}{\epsilon_{\text{rms}}^i}$
a_0	Normalised vector potential = $\frac{e \mathbf{E}_L }{m_e c \omega_L}$
A	Atomic mass number
\mathbf{A}	Three-vector potential
\mathbf{A}^μ	Four-vector potential = $(\phi/c, \mathbf{A})$
β	Normalised speed = v/c or Twiss parameter = $\frac{\langle x_i \rangle}{\epsilon_{\text{rms}}^i}$
β	Normalised velocity = \mathbf{v}/c
\mathbf{B}	Magnetic field
\mathbf{B}_L	Magnetic field of a laser pulse
c	Speed of light = $3.00 \times 10^8 \text{ m s}^{-1}$
δ	Skin depth
$\delta(\mathbf{x})$	Dirac-delta function
$d\mathbf{s}$	Vector line element
Δ	Change in a variable
D	Number of dimensions
∇	Partial derivative = $\hat{\mathbf{x}}_\mu \frac{\partial}{\partial x_\mu}$, $\mu = x, y, z$
ϵ_0	Permittivity of free space = $8.854 \times 10^{-12} \text{ F m}^{-1}$
ϵ_{rms}	Transverse geometric emittance
$\epsilon_{n,\text{rms}}$	Transverse normalised emittance
e	Absolute charge of an electron = $1.602 \times 10^{-19} \text{ C}$
e^\pm	Electron (−) or positron (+)
\mathbf{E}	Electric field
E_S	Schwinger electric field = $1.3 \times 10^{18} \text{ V m}^{-1}$

\mathbf{E}_L	Electric field of a laser pulse
f	Distribution function
\mathbf{F}_L	Lorentz force = $q(\mathbf{E} + \mathbf{v} \times \mathbf{B})$
γ	Lorentz/gamma factor = $\frac{1}{\sqrt{1-\beta^2}}$ or Twiss parameter = $\frac{\langle x_i'^2 \rangle}{\epsilon_{rms}^i}$ or high-energy photon
η	Efficiency
I	Electromagnetic field intensity
\mathcal{H}	Hamiltonian
θ	Angle of incidence of a laser pulse
\mathbf{J}	Current density
\mathbf{k}	Electromagnetic three-wave vector
\mathbf{K}^μ	Electromagnetic four-wave vector = $(\omega/c\mathbf{k})$
K	Boltzmann constant = $1.38 \times 10^{-23} \text{ J K}^{-1}$
λ_D	Debye length $\equiv \sqrt{\frac{\epsilon_0 K T_e}{n_e e^2}}$
λ_L	Laser pulse wavelength
Λ_ν^μ	Lorentz transformation matrix
L	Length
\mathcal{L}	Lagrangian
μ_0	Vacuum permeability = $1.257 \times 10^{-6} \text{ N A}^{-2}$
m_e	Mass of an electron = $9.11 \times 10^{-31} \text{ kg}$
n	Harmonic order
n, N	Number
n_c	Plasma critical density = $\frac{\omega_L^2 m_e \epsilon_0}{e^2}$
n_e	Plasma electron number density
\bar{n}_e	Normalised plasma electron number density = $\frac{n_e}{n_c}$
n_i	Plasma ion number density
\mathbf{n}	Vector normal to a surface
N_A	Avogadro's number
N_D	Number of particles within the Debye sphere = $\frac{4}{3}\pi\lambda_D^3 n$
ω	Angular frequency of an oscillation or low energy photon
ω_L	Laser pulse angular frequency

ω_p	Plasma frequency = $\sqrt{\frac{e^2 n_e}{m_e \epsilon_0}}$
ϕ	Angle of laser polarisation out of the plane of interaction or scalar electromagnetic potential
\mathbf{p}	Three-momentum
P	Pressure
\mathbf{P}^μ	Four-momentum = $(U/c, \mathbf{p})$
Q	Charge
ρ	Density
r_L	Relativistic Larmor radius = $\frac{\gamma m_e v}{e \mathbf{B} }$
\mathbf{r}	Radial vector
$\hat{\mathbf{r}}$	Radial unit vector
R	Rate
σ	Surface area
S	Relativistic similarity parameter = \bar{n}_e/a_0
$S(\mathbf{x})$	Shape function
τ	Average time or standard deviation of time
t	Time
T	Kinetic energy
T_e	Plasma electron temperature
u, v	Speed
\mathbf{u}, \mathbf{v}	Velocity
U	Energy
v_ϕ	Phase velocity
V	Potential or volume
w_L	Beam waist
w_p	Quasi-particle weight
χ_γ	Photon quantum parameter
x, y, z	Standard Cartesian coordinates in 3D
$\mathbf{x}, \mathbf{y}, \mathbf{z}$	Vectors along each axis of the Cartesian coordinate system
$\hat{\mathbf{x}}, \hat{\mathbf{y}}, \hat{\mathbf{z}}$	Unit vectors along each axis of the Cartesian coordinate system
Z	Ion charge state in units of e

Subscripts . . . The following are defined the subscripts

C	Pseudocapacitor
e	Electron
γ	Photon
L	Laser pulse or Longitudinal
T	Transvere to a laser pulse
pol	Along the polarisation vector of a laser pulse
\perp	Perpendicular
\parallel	Parallel
i, j	Indices
s	Species
x, y, z	Along the specific Cartesian axes
∞	

The hat symbol To represent a normalised vecotr

primed coordinates and reference frames

1D, 2D, 3D . . .	One-, two- or three-dimension(al)
BW	Breit-Wheeler
CLF	Central Laser Facility
CPA	Chirped Pulse Amplification
CSE	Coherent Synchrotron Emission
FDTD	Finite Difference Time Domain
HB	Hole Boring
HED	High-Energy-Density
HHG	High Harmonic Generation
HPC	High Performance Computing
OHREX	ORION High Resolution X-ray
PIC	Particle-In-Cell
QED	Quantum Electro-Dynamics
RR	Radiation Reaction
SF-QED	Strong-Field Quantum Electro-Dynamics
ZVP	Zero Vector Potential

1

Introduction

Contents

1.1	High-energy-density physics	1
1.2	Electromagnetism fundamentals	4
1.3	The definition of a plasma	5
1.3.1	The Debye length	6
1.3.2	The plasma parameter	7
1.3.3	Collisionality and the plasma frequency	7
1.4	The Lawson-Woodward theorem	9
1.5	Laser-solid density plasma linear interaction	10
1.6	Relativity	11
1.6.1	Ultra-relativistic similarity theory	12
1.6.2	Relativistic lasers and plasmas	14
1.6.3	Conservation of generalised transverse momentum	15
1.7	QED effects	16
1.7.1	High-energy photon emission and radiation reaction . .	16
1.7.2	Multi-photon Breit-Wheeler pair production	17
1.8	Simulating the interaction	18
1.8.1	Supercomputing resources	18
1.8.2	Particle-In-Cell codes	18

1.1 High-energy-density physics

We sit on the verge of the exa-scale revolution both in terms of computing [1] and laser power. With rapid adoption of the pioneering advancements of

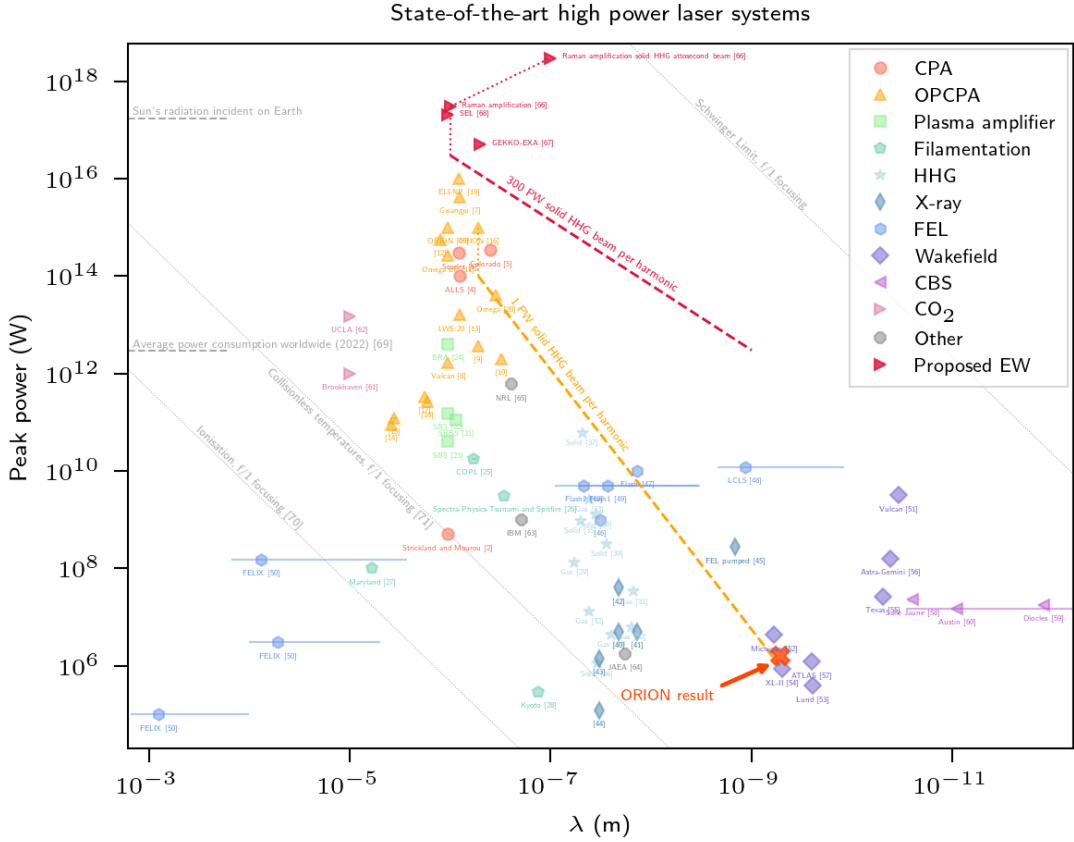


Figure 1.1: A by no means exhaustive plot of laser systems across the globe, both commissioned and theorised [umstadterRelativisticLaserPlasma2003, 2, 4–70] to provide an overview of the parameter space currently and soon to be accessible. The experimental result obtained at the ORION laser facility [16] is presented, and will be discussed in detail in chapter ???. The dashed orange line is the accompanying theoretical prediction. The red dashed line indicates the parameter space accessible via the methods discussed in this thesis when coupled with a sub-etawatt Raman amplified laser beam. Such a beam would provide intensities in the water window many orders of magnitude beyond that currently accessible in state-of-the-art facilities.

Chirped Pulse Amplification (CPA) by Strickland and Mourou [2] and of Optical Parametric Chirped Pulse Amplification [3], multi-petawatt facilities have now been commissioned and built across the globe and plans for sub-exawatt facilities are underway. Figure 1.1 details the parameter space accessible by current and proposed facilities [2, 4–68], clearly, there is no indication of wavering interest or support for the field of High-Energy-Density (HED) physics.

HED physics is the laboratory study of the behaviour of matter with a pressure above 10 GPa, approximately one million atmospheres and containing free electrons

not confined to a solid state [71], typically in the plasma state of matter. HED conditions are found for a vast range of densities and temperatures (from zero to a million million Kelvin) operating in both the quantum and relativistic realms. The applications are equally diverse, including but not limited to inertial confinement fusion, particle acceleration for scientific or medical purposes and light sources for diagnostic tools. Ubiquitous in the natural universe, beyond our solar system, all that can be observed in the sky is radiation emitted from HED plasmas [**chen**].

This thesis concerns itself with a specific interaction, that of a high-power short-pulse laser incident on a flat solid target. Through the process discussed in this thesis, using state-of-the-art 10 PW laser facilities such as [19], electron bunches and light pulse of unprecedented charge and brightness can be produced, both with attosecond duration, thus uncovering new avenues for attosecond resolution diagnostics and to access the Schwinger limit. Seemingly counter-intuitively, as the laser power increases, via relativistic effects and for certain conditions, greater coherency in the electron dynamics can be observed and the signals amplified. The red dashed line of figure 1.1 could be accessed using next generation sub-etawatt facilities. Before delving into this fascinating phenomenon, the remainder of this chapter will provide some of the relevant background information. Chapter 2 introduces the Zero Vector Potential of attosecond absorption in this laser-solid interaction. The following chapter discusses the associated process of Surface High Harmonic Generation and the results of a recent experiment at the ORION laser facility where the absolute intensity of individual X-ray harmonics was measured and compared to the theory.

1.2 Electromagnetism fundamentals

The spatio-temporal propagation of electric $\mathbf{E}(t, \mathbf{x})$ and magnetic $\mathbf{B}(t, \mathbf{x})$ fields must satisfy Maxwell's equations [72]

$$\nabla \cdot \mathbf{B} = 0, \quad (1.1a)$$

$$\nabla \cdot \mathbf{E} = \frac{\rho}{\epsilon_0}, \quad (1.1b)$$

$$\nabla \times \mathbf{B} = \mu_0 \mathbf{J} + \mu_0 \epsilon_0 \partial_t \mathbf{E}, \quad (1.1c)$$

$$\nabla \times \mathbf{E} = -\partial_t \mathbf{B}. \quad (1.1d)$$

Here, $\epsilon_0 = 8.85 \times 10^{-12} \text{ F m}^{-1}$ and $\mu_0 = 1.26 \times 10^{-6} \text{ N A}^{-2}$ are the vacuum permittivity and permeability respectively and $\rho(t, \mathbf{x})$ and $\mathbf{J}(t, \mathbf{x})$ the total charge and current densities of charged particles present.

A particle with charge q and velocity \mathbf{v} in the presence of electromagnetic fields experiences the Lorentz force,

$$\mathbf{F}_L = q(\mathbf{E} + \mathbf{v} \times \mathbf{B}). \quad (1.2)$$

The electromagnetic fields can be obtained from the scalar, ϕ , and vector, \mathbf{A} , potentials as [73]

$$\mathbf{E} = -\nabla \phi - \partial_t \mathbf{A}, \quad (1.3)$$

$$\mathbf{B} = \nabla \times \mathbf{A}. \quad (1.4)$$

The Vlasov-Maxwell system of equations

A collisionless and fully ionised plasma is fully described in the kinetic description by the Vlasov-Maxwell system of equations [74]. Each plasma species, s , of particles with mass m_s and charge q_s is described by its distribution function $f_s(t, \mathbf{x}, \mathbf{p})$ at time t , position \mathbf{x} and momentum $\mathbf{p} = m_s \gamma \mathbf{v}$. The distribution satisfies the Vlasov equation, that is,

$$(\partial_t + \frac{\mathbf{p}}{m_s \gamma} \cdot \nabla + \mathbf{F}_L \cdot \nabla_{\mathbf{p}}) f_s = 0, \quad (1.5)$$

where \mathbf{F}_L is the Lorentz force given in equation 1.2. The electric $\mathbf{E}(t, \mathbf{x})$ and magnetic $\mathbf{B}(t, \mathbf{x})$ fields that generate the force must satisfy Maxwell's equations (equations 1.1).

This self-consistent system of equations describes the dynamics of plasma particles within electromagnetic fields. The particles modify the fields via their charge and current densities,

$$\rho(t, \mathbf{x}) = \sum_s q_s \int d^3 p f_s(t, \mathbf{x}, \mathbf{p}), \quad (1.6)$$

and

$$\mathbf{J}(t, \mathbf{x}) = \sum_s q_s \int d^3 p \mathbf{v} f_s(t, \mathbf{x}, \mathbf{p}), \quad (1.7)$$

respectively.

1.3 The definition of a plasma

As outlined in F. Chen's definitive textbook 'Introduction to Plasma Physics and Controlled Fusion' [72], a plasma must fulfil three criteria, namely,

1. Ionisation: a plasma must consist of both charged and neutral particles, of course this alone cannot define a plasma, any gas will contain some degree of ionisation, however, with reference to figure 1.1, clearly, modern high power laser systems will instantaneously fully ionise a target upon incidence;
2. Quasineutrality: while locally there can be (often extreme) electromagnetic forces and charge concentrations at work, over the length scales of the plasma, such forces are screened out and the plasma bulk remains net neutral in charge;
3. Collective behaviour: unlike in a gas, where collisions will dominate the dynamics, the particles in a plasma generate electromagnetic fields that interact at a distance and thus a particle's motion depends not only on its immediate vicinity but on the surrounding plasma conditions, indeed often it is the so-called *collisionless* plasmas where collisions can be safely neglected that are of most interest, as is the focus of this thesis.

These conditions can be quantitatively described by the Debye length, the plasma parameter and the plasma frequency as laid out in the following sections.

1.3.1 The Debye length

The Debye length describes the extent to which a plasma can shield electromagnetic fields within and so remain quasineutral. Consider an infinitely extending plasma with a test charge placed at some point, then what would be the scalar potential $\phi(\mathbf{x})$ around it? If the plasma had no kinetic energy, the charged particles would arrange themselves immediately adjacent to the test charge and once this equilibrium state was reached there would be no electromagnetic fields present. More realistically, the plasma will have some temperature, likely a very large temperature and so some particles will be able to escape the potential of the test charge and thus leak electromagnetic fields into the plasma bulk. Poisson's equation (equation 1.1b in the static case) reads

$$\epsilon_0 \nabla^2 \phi = -e(Zn_i - n_e), \quad (1.8)$$

where $\epsilon_0 = 8.854 \times 10^{-12} \text{ F m}^{-1}$ is the permittivity of free space, $e = 1.602 \times 10^{-19} \text{ C}$ is the charge of an electron, Z is the plasma ion charge in units of e and n_i and n_e are the number densities of plasma ions and electrons.

Since the electrons are significantly more mobile than the ions due to their lower mass, it is in general the electrons and not the ions that respond to the test charge and the ions can be assumed to provide a constant background of positive charge density. If the number density of electrons follows a Boltzmann temperature distribution in the presence of a potential energy $-e\phi$, then

$$n_e = n_{e,0} e^{e\phi/KT_e}, \quad (1.9)$$

where $n_{e,0}$ is the electron number density far from the test charge, $n_i = n_{e,0}/Z$, $K = 1.38 \times 10^{-23} \text{ J K}^{-1}$ is the Boltzmann constant and T_e is the electron temperature in Kelvin. Note that in plasmas it is very common for different species to have differing temperatures depending on the mechanism for energy absorption and the timescales for collisions compared to the timescale of the study.

Substituting equation 1.9 into equation 1.8 and Taylor expanding the exponential term in the limit that the plasma is weakly coupled ($e\phi \ll KT_e$),

$$\nabla^2\phi = \frac{\phi}{\lambda_D^2}, \quad (1.10)$$

where

$$\lambda_D \equiv \sqrt{\frac{\epsilon_0 K T_e}{n_e e^2}}, \quad (1.11)$$

is the *Debye length* and describes the thickness of the charge sheath surrounding the test charge. For quasineutrality to hold for the plasma bulk, its spatial dimensions, L , must extend beyond a few Debye lengths, *i.e.*

$$L \gg \lambda_D. \quad (1.12)$$

1.3.2 The plasma parameter

In order for the derivation of section 1.3.1 to be statistically valid, there must be a large number of charged particles within the shielding sheath. The number of particles within the *Debye sphere* is

$$N_D = \frac{4}{3}\pi\lambda_D^3 n, \quad (1.13)$$

where, N_D is the *plasma parameter*. Note that, as discussed above, in most cases it is most suitable to choose the number density n to be the number density of electrons, n_e . To ensure the plasma is suitably ionised (criterion 1) and that the plasma engages in collective behaviour (criterion 3),

$$N_D \ggg 1. \quad (1.14)$$

1.3.3 Collisionality and the plasma frequency

Collective behaviour not only depends on the ability for large numbers of particles to interact via electromagnetic forces but also that these forces dominate over collisions in describing particle trajectories. Taking ω as the typical frequency of plasma oscillations and τ as the average time between collisions, for a plasma (as opposed to a gas)

$$\omega\tau > 1 \quad (1.15)$$

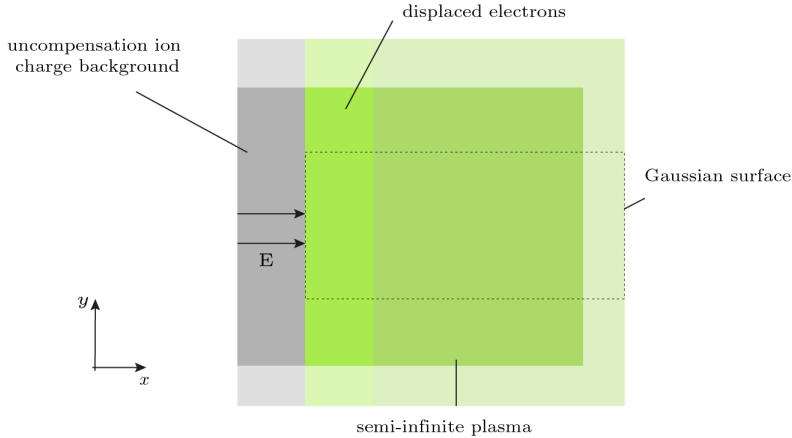


Figure 1.2: The electrons of a semi-infinite plasma are displaced inwards by some external force leaving in their wake an uncompensated space charge of ‘immobile’ positive ions. By constructing a Gaussian surface along the dashed line, using Gauss’ Law, the electric field associated with the positive space charge can be calculated.

is required. It now remains to determine what is the typical frequency of collisions in a given plasma. While the types of plasma waves and their associated frequencies of oscillation are multitudinous, the characteristic frequency, the *plasma frequency*, ω_p , is the most straightforward. It describes the response of electrons to charge imbalances within an infinite uniform plasma at rest in the absence of magnetic fields or temperature fluctuations. As noted in section 1.3.1, the ions provide a constant background of positive charge.

Consider an semi-infinite plasma existing for $x > 0$, with electron density n_e and ion density n_e/Z of charge state Z^1 . Suppose the electron fluid is displaced by some perfectly isotropic force into the plasma bulk a distance $(\Delta x)\hat{\mathbf{x}}$ as in figure 1.2. The total charge of displaced electrons within a surface area of σ is

$$Q = -en_e\sigma\Delta x. \quad (1.16)$$

Applying the integral form of Gauss’ law (from equation 1.1b) to the surface detailed in figure 1.2, the uncompensated charge leads to

$$-\sigma E\hat{\mathbf{x}} = \frac{Q}{\epsilon_0}\hat{\mathbf{x}} = -\frac{en_e\sigma\Delta x}{\epsilon_0}\hat{\mathbf{x}} \quad (1.17)$$

¹This description has direct relevance to the Zero Vector Potential mechanism which will be made clear in chapter 2.

at the electron surface. By the Lorentz force, equation 1.2, the displaced electrons will experience a restoring force, $-eE\hat{x}$, perpendicular to the surface due to the electron-ion charge imbalance. The equation of motion for electrons on that surface is therefore

$$m_e \frac{d^2\Delta x}{dt^2} = -eE = -\frac{e^2 n_e}{\epsilon_0} \Delta x. \quad (1.18)$$

Equation 1.18 clearly describes a simple harmonic oscillator with a characteristic frequency given by the plasma frequency,

$$\omega_p = \sqrt{\frac{e^2 n_e}{m_e \epsilon_0}}. \quad (1.19)$$

1.4 The Lawson-Woodward theorem

The Lawson-Woodward theorem states that there can be no net electron energy gain using laser fields [75], quite at odds with one of the primary aims of this thesis, that is, the acceleration of electrons. There are, however, several conditions that must be met, namely,

1. The interaction region is infinite;
2. The interaction occurs in a vacuum;
3. The electron is ultra-relativistic ($v \approx c$) along the acceleration gradient;
4. No electro- or magnetostatic fields are present;
5. Non-linear effects are neglected.

Several of these will be applicable to the various accelerations of electrons considered. It is this final condition that is most damning to the application of the theorem. Throughout this thesis the ultra-relativistic laser pulses under consideration ensure non-linear effects cannot be neglected. It is indeed such non-linearities that are of most interest.

1.5 Laser-solid density plasma linear interaction

Consider small transverse electromagnetic waves propagating through a plasma. Linearising equation 1.2 for a single plasma electron by assuming only small field variations and thus small velocity variation,

$$m_e \dot{\mathbf{v}}_e = -e\mathbf{E}. \quad (1.20)$$

Combining the time derivative of equation 1.1c and the curl of equation 1.1d,

$$\nabla \times \nabla \times \mathbf{E} = -\mu_0 \dot{\mathbf{J}} - \mu_0 \epsilon_0 \ddot{\mathbf{E}}. \quad (1.21)$$

Considering only fast oscillations such that ions are effectively immobile,

$$\mathbf{J} = -n_e e \mathbf{v}_e \quad (1.22)$$

and using the identity $\nabla \times \nabla \times \mathbf{E} = \nabla(\nabla \cdot \mathbf{E}) - \nabla^2 \mathbf{E}$,

$$\nabla(\nabla \cdot \mathbf{E}) - \nabla^2 \mathbf{E} = -\frac{\mu_0 n_e e^2}{m_e} \mathbf{E} - \mu_0 \epsilon_0 \ddot{\mathbf{E}}. \quad (1.23)$$

Assuming plane wave solutions of the form

$$\mathbf{E} = \mathbf{E}_0 e^{i(\mathbf{k} \cdot \mathbf{x} - \omega t)}, \quad (1.24)$$

where \mathbf{k} is the wave-vector and ω the frequency of oscillations and noting the waves are transverse $\mathbf{k} \cdot \mathbf{E} = 0$,

$$|\mathbf{k}|^2 \mathbf{E} = -\frac{\mu_0 n_e e^2}{m_e} \mathbf{E} + \mu_0 \epsilon_0 \omega^2 \mathbf{E} \quad (1.25)$$

and hence the dispersion relation for electromagnetic waves propagating in a plasma is

$$\omega^2 = c^2 |\mathbf{k}|^2 + \omega_p^2. \quad (1.26)$$

Equation 1.26 exhibits a *cutoff* dependent on the plasma density via ω_p . The *critical density*, n_c , is defined as the density above which a laser pulse of frequency ω_L cannot propagate through a plasma. This occurs for $\omega_L = \omega_p$, thus,

$$n_c = \frac{m_e \epsilon_0 \omega_L^2}{e^2}. \quad (1.27)$$

As the plane wave has a spatial dependence $\sim \exp(\mathbf{k} \cdot \mathbf{x})$, if $n_e > n_c$, \mathbf{k} is imaginary and the wave no longer propagates through the plasma and instead exponentially attenuates over a skin depth,

$$\delta = \frac{1}{|\mathbf{k}|} = \frac{c}{\sqrt{\omega_p^2 - \omega_L^2}} \quad (1.28)$$

and is reflected. For typical high power lasers with wavelengths in the visible or near-infrared, fully ionised solids tend to have densities well above the critical density and thus

1.6 Relativity

Modern high-power lasers operate in the domain of relativistic mechanics and in general interactions are highly non-linear. It is useful to introduce some of the basic principles of relativity. Note that while there has been growing interest in the curvature of spacetime by relativistic lasers [76], this effect remains undetectable at present. Thus, throughout this thesis the inner product of 4-tensors is defined using the Minkowski Metric [73].

Many useful quantities can be arranged into contravariant four-vectors that undergo a Lorentz transformation for a change of frame of reference [73], specifically,

$$\mathbf{A}'^\mu = \Lambda_\nu^\mu \mathbf{A}^\mu, \quad (1.29)$$

where Λ_ν^μ is the appropriate Lorentz transformation, and primed symbols typically denote boosted frames of reference. Without loss of generality, the coordinate system can be defined such that the boosted frame travels along the \mathbf{x} -axis with respect to the initial frame. Thus, the Lorentz transformation is defined

$$\Lambda_\mu^\nu = \begin{pmatrix} \gamma & -\beta\gamma & 0 & 0 \\ -\beta\gamma & \gamma & 0 & 0 \\ 0 & 0 & 1 & 0 \\ 0 & 0 & 0 & 1 \end{pmatrix}. \quad (1.30)$$

Generally, a *beta factor* is a normalised speed or velocity of an object,

$$\beta = \frac{v}{c}, \quad (1.31)$$

Symbol	Name	Components	Invariant
\mathbf{X}^μ	4-displacement	(ct, \mathbf{x})	$-c^2\tau^2$
\mathbf{A}^μ	4-potential	$(\phi/c, \mathbf{A})$	
\mathbf{J}^μ	4-current density	$(c\rho, \mathbf{J})$	$-c^2\rho_0^2$
\mathbf{K}^μ	4-wave vector	$(\omega/c, \mathbf{K})$	
\mathbf{P}^μ	4-momentum	$(U/c, \mathbf{p})$	$-m^2c^2$

Table 1.1: Four-vectors of relevance to this thesis. New parameters are the proper time, τ , the proper charge density, ρ_0 , energy, $U = \gamma mc^2$, three-momentum, $\mathbf{p} = \gamma m\mathbf{v}$.

here it refers to the frame velocity and its associated Lorentz or *gamma factor* is

$$\gamma = \frac{1}{\sqrt{1 - \beta^2}}. \quad (1.32)$$

Four-vectors relevant this thesis are listed in table 1.1. Transformations of electromagnetic fields under reference frame boosts are given in appendix A.1 and Maxwell's equations are Lorentz covariant.

Focusing now on the 4-potential \mathbf{A}^μ , choosing the Lorenz gauge,

$$\partial_\mu \mathbf{A}^\mu = \nabla \cdot \mathbf{A} + \frac{1}{c^2} \partial_t \phi = 0, \quad (1.33)$$

then Maxwell's equations can be written

$$\partial_\nu \partial^\nu \mathbf{A}^\mu = -\frac{1}{c^2 \epsilon_0} \mathbf{J}^\mu. \quad (1.34)$$

Equation 1.34 can then be solved to yield

$$\mathbf{A}(\mathbf{x}, t) = \frac{\mu_0}{4\pi} \int \frac{\mathbf{J}(\mathbf{x}', t_a)}{|\mathbf{x} - \mathbf{x}'|} d^3 \mathbf{x}', \quad (1.35)$$

where $t_a = t - |\mathbf{x} - \mathbf{x}'|/c$ is the advanced time.

1.6.1 Ultra-relativistic similarity theory

Consider a relativistically intense laser pulse normally incident on a collisionless plasma as in figure 1.2 and neglect ion motion. The electron distribution is fully described by the Vlasov equation (equation 1.5) with the self-consistent electric and magnetic fields satisfying Maxwell's equations (equations 1.1). Suppose the incident laser pulse has an initial vector potential

$$\mathbf{A}(t=0) = \mathbf{a}((y^2 + z^2)/R^2, x/c\tau) \cos k_L x. \quad (1.36)$$

This envelope form for the potential, $\mathbf{a}((y^2 + z^2)/R^2, x/c\tau)$, is sensible provided $k_L R \gg 1$ and $\omega_L \tau \gg 1$, where R is the focal spot radius and τ the pulse duration. For fixed laser envelope, the laser-plasma dynamics depends on just four dimensionless variables: the normalised focal spot size, $k_L R$, the normalised pulse duration, $\omega_L \tau$, the normalised laser vector potential amplitude

$$a_0 = \max \left| \frac{e\mathbf{a}}{m_e c^2} \right|, \quad (1.37)$$

in terms of the peak laser electric field amplitude \mathbf{E}_L ,

$$a_0 = \frac{e|\mathbf{E}_L|}{m_e c \omega_L}, \quad (1.38)$$

and the normalised plasma density

$$\bar{n}_e = \frac{n_e}{n_c}. \quad (1.39)$$

By normalising the system of equations, details given in appendix, and combining these last two expressions into the *relativistic similarity parameter*,

$$S = \frac{\bar{n}_e}{a_0}, \quad (1.40)$$

it is possible to show that in the ultra-relativistic limit ($a_0 \gg 1$), the dynamics of the system is similar for constant S [77] with plasma electrons following similar trajectories where

$$\mathbf{p} \sim a_0. \quad (1.41)$$

There is also a more physical meaning to the S parameter. Consider again section 1.5 on the propagation of linear electromagnetic waves through a plasma but now for the case of an ultra-relativistic laser pulse. For an electron rotating in an electromagnetic field,

$$\mathbf{F}_\perp = \gamma m_e \mathbf{a}_\perp, \quad (1.42)$$

where \mathbf{a}_\perp is the acceleration perpendicular to the motion and thus the response of the electrons is reduced by a factor of γ . While some find the *relativistic mass*

correction to be somewhat unhelpful nomenclature for the phenomenon [73], it has nevertheless become commonplace within the literature of relativistic plasma physics [**umstadterRelativisticLaserPlasma2003**]. Turning the handle, one finds that the relativistic plasma frequency is

$$\omega_p^{\text{rel}} = \sqrt{\frac{e^2 n_e}{\gamma m_e \epsilon_0}}. \quad (1.43)$$

Using equation 1.41, and taking $v \approx c$, then $\gamma \approx a_0$ and the normalised relativistic cutoff density is simply S . Thus, the ultra-relativistic similarity parameter is just a measure of the overdensity of a plasma once relativistic corrections have been applied, *i.e.* for $S > 1$, a laser pulse will be reflection, however for $\bar{n}_e > 1$ and $S < 1$, one enters the regime of relativistically self-induced transparency [78]. It is now possible to define the parameter space of interest in this thesis: relativistic laser plasma surface interactions occur for $a_0 \gg 1$ and $S > 1$.

1.6.2 Relativistic lasers and plasmas

The descriptor *relativistic* is applied liberally in this thesis. When applied to electromagnetic fields or laser pulses it refers to

$$a_0 \geq 1. \quad (1.44)$$

When applied to particles, their Lorentz factors are

$$\gamma = \frac{1}{\sqrt{1 - \beta^2}} \geq 2, \quad (1.45)$$

corresponding to a speed, $u \geq 0.87c$. *Ultra-relativistic* implies these quantities are much larger than the conditions provided. A relativistic laser pulse will accelerate electrons to relativistic velocities in a fraction of a laser pulse cycle. Consider an electron in the presence of a uniform electric field of magnitude $a_0 = 100$, an intensity accessible by current state of the art laser facilities. The work done on that particle by the field is

$$T = (\gamma - 1)m_e c^2 = \int \mathbf{E} \cdot d\mathbf{x}, \quad (1.46)$$

The field will accelerate an electron to relativistic velocities in a distance less than 1 % of a corresponding laser pulse wavelength.

1.6.3 Conservation of generalised transverse momentum

Consider a holonomic system of N relativistic particles under the influence of electromagnetic forces. A particle j with charge e_j and mass m_j experiences a scalar potential,

$$V_j = e_j(\phi - \mathbf{A} \cdot \mathbf{v}_j) \quad (1.47)$$

and hence the system is described by the Lagrangian [79]

$$\mathcal{L} = \sum_{j=1}^N \left(-m_j c^2 \sqrt{1 - \beta_j^2} - e_j(\phi - \mathbf{A} \cdot \mathbf{v}_j) \right), \quad (1.48)$$

The generalised momentum corresponding to coordinate x_j is

$$p_{j,x} = \frac{\partial L}{\partial \dot{x}_j} = \frac{m_j \dot{x}_j}{\gamma_j} + e_j A_x, \quad (1.49)$$

thus, the generalised momentum describes both the linear mechanical momentum and the momentum of the electromagnetic field. Via Noether's theorem, if L is independent of x_j , *i.e.* spatially homogeneous along x for particle j , then

$$\dot{p}_{j,x} = 0 \quad (1.50)$$

since

$$\frac{d}{dt} \left(\frac{\partial L}{\partial \dot{x}_j} \right) = \frac{\partial L}{\partial x_j}. \quad (1.51)$$

Consider a linearly polarised Gaussian laser pulse, with axis of polarisation along x incident on a solid target at rest. Then A_x is approximately constant along x near the beam centre². Integrating equation 1.52 and noting that initially there is no linear or electromagnetic momentum at the target, the generalised transverse momentum conservation equation for an electron in the laser field is

$$p_T = eA, \quad (1.52)$$

where p_T is the electron momentum along the polarisation axis of the laser pulse and A it the laser pulse 3-vector potential amplitude. As a sanity check, this expression complies with the ultra-relativistic similarity result of equation 1.41.

²Constant relative to the scale of typical electron trajectories in such an interaction.

Note that this is only valid provided the electron does not radiate along the direction of polarisation as discussed by Sokolov *et al* [80]. The implications of *Radiation Reaction* are discussed in the following section.

1.7 QED effects

Next generation laser facilities will enable the testing of decades old theoretical predictions of Strong-Field Quantum Electro-Dynamics (SF-QED). Already Fedeli *et al* have shown in simulations that current PW-class laser facilities can access the regime using an all-optical set up based on laser-solid surface interactions [81]. The Schwinger Limit **CITE** $E_S = 1.32 \times 10^{18} \text{ V m}^{-1}$ is field intensity at which the vacuum becomes non-linear. If by some means an electron can be directed towards a plane electromagnetic wave, by consideration of the Lorentz transformations of electromagnetic fields (equations A.1), it is possible that provided the electron is sufficiently relativistic, in its own frame of rest it will ‘see’ electromagnetic fields intense enough to access vacuum non-linearities. The first two frontiers of SF-QED that will be accessible are Radiation Reaction and multi-photon Breit-Wheeler electron pair production. Brief introductions to these phenomena are now presented.

1.7.1 High-energy photon emission and radiation reaction

When a charged particle undergoes an acceleration, it emits electromagnetic radiation. If the electromagnetic field is sufficiently strong, *i.e.* approaching the Schwinger Limit in the rest frame of the particle, then a non-negligible fraction of the particle momentum can be transferred to the emitted high energy photon, substantially impacting the dynamics of the accelerated particle. This back reaction is known as Radiation Reaction (RR).

Smilei (detailed in the following section) implements the process of high-energy photon emission as Inverse Compton Scattering on the basis of several assumptions [82], namely,

1. radiating particles are ultra-relativistic and therefore radiation is emitted in the direction of travel of the particle;

2. the field varies slowly over the timescale of photon emission, this is the *locally-constant field approximation* and requires ultra-relativistic field strengths;
3. but they are small with respect to the Schwinger Limit, specifically requiring the invariants $\sqrt{c^2\mathbf{B}^2 + \mathbf{E}^2}$ and $\sqrt{c\mathbf{B} \cdot \mathbf{E}} < E_S$;
4. real particles radiated independently of their neighbours, this requires the emitted wavelength being shorter than the typical inter-particle spacing.

Provided such conditions hold, the rate of photon emission depends on two invariants [83], the electron quantum parameter

$$\chi = \frac{\gamma}{E_S} \sqrt{(\mathbf{E} + \mathbf{v} \times \mathbf{B})^2 - (\mathbf{v} \cdot \mathbf{E})^2/c^2}, \quad (1.53)$$

where \mathbf{v} is the electron velocity and the emitted photon quantum parameter

$$\chi_\gamma = \frac{\gamma_\gamma}{E_S} \sqrt{(\mathbf{E}_\perp + \mathbf{c} \times \mathbf{B})^2 - (\mathbf{c} \cdot \mathbf{E})^2/c^2}, \quad (1.54)$$

where γ_γ is the normalised photon energy $= \hbar\omega_\gamma/m_e c^2$. The exact relationship is complex and in the the fully quantum domain ($\chi > 1$), is it not practical to solve the integrations required for all particles and instead values are extracted from precalculated tables and into a Monte-Carlo algorithm.

1.7.2 Multi-photon Breit-Wheeler pair production

Multi-photon Breit-Wheeler pair production, also known as non-linear Breit-Wheeler is the decay of a high energy photon, typically produced via RR, into an electron-positron pair in the presence of a strong electromagnetic field, explicitly,

$$\gamma + n\omega \rightarrow e^- + e^+. \quad (1.55)$$

The strength of the effect is dependent on the Lorentz invariant photon quantum parameter, equation 1.54 Cite Smilei and say, in a constant E-field, the rate of pair production increases rapidly up to $\chi_\gamma \approx 10$ at which point it saturates and slowly reduces.

1.8 Simulating the interaction

Modelling laser-plasma interactions is a notoriously challenging endeavour; due to the complexity of the many-bodied systems involved (a fully ionised centimetre cubed block of plastic contains on the order of 10^{23} particles) and the stochasticity of particle motion, it is frequently impossible to construct models *ab initio*. Instead, hydrodynamic simulation codes such as HYADES [84] and FLASH [85] and Particle-In-Cell simulation codes such as Smilei [74], Osiris [86] and EPOCH [87] are used to construct phenomenological models and to direct experimentation.

1.8.1 Supercomputing resources

Modern High Performance Computing (HPC) systems are poised to enter the exascale regime ($> 10^{18}$ Floating Point Operations Per Second). With limited improvements in microprocessor technologies, such power is achieved through massive parallelisation across processing units. To enable the study of the dynamics of up to billions of macroparticles, PIC codes test the limits of current supercomputing architectures. ARCHER2, the UK’s national supercomputer came online in November 2021, with it delivering over ten times the resources of its predecessor (ARCHER) [88]. An HPE Cray EX supercomputing system with a peak performance estimated at 28 Pflops s^{-1} across 5860 nodes each with dual AMD EPYCTM 7742 64-core processor for a total of 750,080 cores, ARCHER2 was able to supply the resources required to run the costly PIC simulations for this research. The substantially cheaper HYADES simulations were performed using the Rutherford Appleton Laboratory’s SCARF HPC cluster [89].

1.8.2 Particle-In-Cell codes

Discretisation of the Vlasov-Maxwell equations

Finding numerical solutions to the Vlasov-Maxwell equations is no straightforward task, while codes exist that are capable, such as Valis [90], the requirement of high resolution in both position and momentum is exceedingly costly and the use of such codes is limited with respect to their size, duration and spatial dimensions. A more

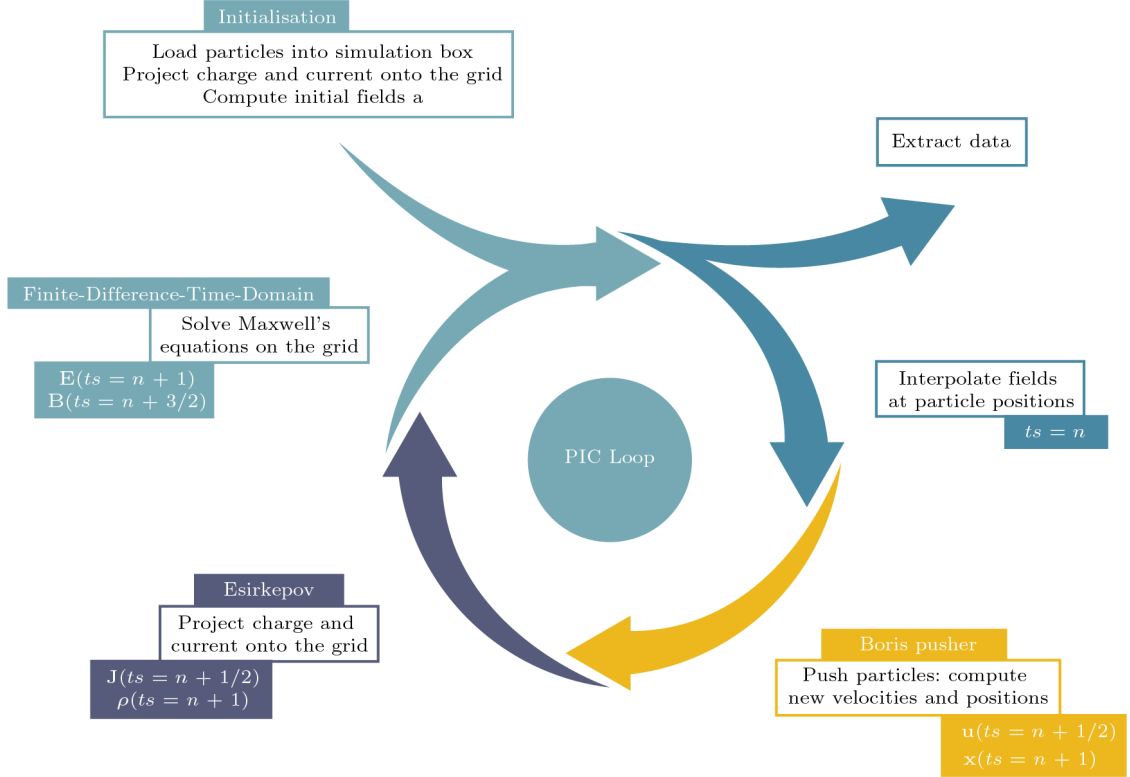


Figure 1.3: A schematic of the PIC code loop and the algorithms performed from time step, ts , from n to $n + 1$.

tractable approach is to discretise the distribution function into N_s *quasi-particles*³. These are often referred to as *macro-particles* in practice and typically represent a large number of real particles, such that

$$f_s(t, \mathbf{x}, \mathbf{p}) = \sum_{p=1}^{N_s} w_p S(\mathbf{x} - \mathbf{x}_p(t)) \delta(\mathbf{p} - \mathbf{p}_p(t)), \quad (1.56)$$

where w_p is the quasi-particle's weight, \mathbf{x}_p and \mathbf{p}_p are its position and momentum respectively, δ is the Dirac-delta distribution and $S(\mathbf{x})$ the shape-function chosen to represent the quasi-particle. The Vlasov equation is then integrated along the continuous trajectories of the quasi-particles while Maxwell's equations are solved on a discrete spatial grid of *cells*. Such a code is aptly named a *Particle-In-Cell* (PIC) code. A schematic of the standard PIC code algorithm is presented in figure 1.3. After particle and field initialisation, fields are interpolated at particle positions. The well-established momentum-conserving *Boris pusher* algorithm computes the

³Originally introduced by Langdon and Birdsall as *clouds* [91].

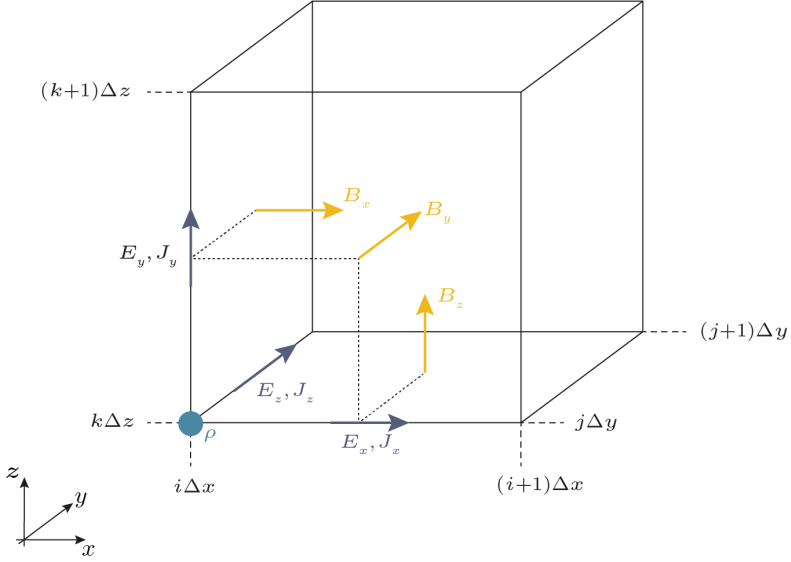


Figure 1.4: A representation of the staggered 3D Yee grid for the cell at $(i\Delta x, j\Delta y, k\Delta z)$ for spatial centering of the curl operations, including the locations where all system properties are defined.

new macro-particle velocities and positions [92]. Particles are advanced in time using a *leap-frog* scheme, where positions are defined at integer, n , time steps and momenta at half integer, $n + 1/2$. The charge conserving Esirkepov algorithm [93] projects the new charge and current densities onto the grid to then solve Maxwell's equations on the grid using the Finite-Difference-Time-Domain approach [94]. To ensure space and time centering of the electromagnetic field derivatives in Maxwell's equations, electric and magnetic fields are discretised on the staggered *Yee grid* as represented in figure 1.4. with electric fields defined at integer time steps and magnetic fields at half-integer time steps.

Smilei

Smilei (for Simulating Matter Irradiated by Light at Extreme Intensities) is a modern collaborative, massively-parallel, fully relativistic and open source plasma physics PIC code and the major workhorse for this thesis⁴. Produced by M. Grech's team(CHECK THIS) at École Polytechnique [74], its recent development was motivated by the rapid advancements of multi-petawatt facilities both globally and locally with the recent completion of the 10 PW Apollon laser facility and by the

⁴At points benchmarks against the EPOCH and Osiris PIC codes were performed.

Units of	SI units	Normalisation
velocity	m s^{-1}	c
charge	C	e
mass	kg	m_e
momentum	kg m s^{-1}	$m_e c$
energy/temperature	J	$m_e c^2$
time	s	ω_L^{-1}
length	m	c/ω_L
number density	m^{-3}	n_c
electric field	V m^{-1}	$m_e c \omega_L / e$

Table 1.2: Smilei normalisations for common quantities with the laser angular frequency ω_L set at the reference angular frequency.

availability of supercomputing power which has ‘skyrocketed’ in recent years [74]. Indeed, the 3D PIC simulations discussed in this thesis required the parallelisation of almost 20 % of the computing resources available on ARCHER2.

Reference units

Given the broad range of magnitudes linked to multi-petawatt and femtosecond laser pulses, solid density plasmas, micrometer wavelengths, and attosecond electron bunches, it becomes significantly more convenient to transform them into dimensionless normalised values. Smilei operates in such units. This normalisation is not chosen *a priori*, instead results can be scaled by an arbitrary reference angular frequency. This is extremely useful when working with boosted frames of reference. As this thesis focuses on the interaction of a laser pulse with plasma, the laser pulse angular frequency, ω_L is set as the frequency of reference. A list of the most common normalisations are given in table 1.2.

Simulation parameters

Silver-Müller boundary conditions for the simulation box edges [95] are able to absorb and inject electromagnetic waves and particles. Note that there can be non-physical reflection of electromagnetic waves at such boundaries leading to some error.

The quasi-particle shape function $S(\mathbf{x})$ determines the projection of particle charge onto the grid. It is symmetric in all dimensions with respect to \mathbf{x} and

extends over n cells of width Δx in each direction where n is the interpolation order. It can be written as a product across D dimensions,

$$S(\mathbf{x}) = \prod_{\mu=1}^D s^{(n)}(x^\mu). \quad (1.57)$$

Smilei implements orders 2, 3 and 4, the explicit shape functions are

$$s^2(n) = \begin{cases} \frac{1}{\Delta x} \left(1 - \left|\frac{x}{\Delta x}\right|\right) & \text{if } |x| \leq \Delta x, \\ 0 & \text{otherwise,} \end{cases} \quad (1.58a)$$

$$s^3(n) = \begin{cases} \frac{3}{4\Delta x} \left(1 - \frac{4}{3} \left(\frac{x}{\Delta x}\right)^2\right) & \text{if } |x| \leq \frac{1}{2}\Delta x, \\ \frac{9}{8\Delta x} \left(1 - \frac{2}{3} \left|\frac{x}{\Delta x}\right|\right)^2 & \text{if } \frac{1}{2}\Delta x < |x| \leq \frac{3}{2}\Delta x, \\ 0 & \text{otherwise,} \end{cases} \quad (1.58b)$$

$$s^4(n) = \begin{cases} \frac{2}{3\Delta x} \left(1 - \frac{3}{2} \left(\frac{x}{\Delta x}\right)^2 + \frac{3}{4} \left|\frac{x}{\Delta x}\right|^3\right) & \text{if } |x| \leq \Delta x, \\ \frac{4}{3\Delta x} \left(1 - \frac{1}{2} \left|\frac{x}{\Delta x}\right|^3\right) & \text{if } \Delta x < |x| \leq 2\Delta x, \\ 0 & \text{otherwise.} \end{cases} \quad (1.58c)$$

While the correct implementation of collisions in PIC codes remains an open problem [96], Smilei has implemented relativistic binary collisions between macroparticles using a Monte-Carlo based scheme [97]. The aforementioned QED processes of Inverse Compton scattering and non-linear Breit-Wheeler pair production are included using the built-in Smilei packages [74]. These processes can lead to cascades of many particles being added to the simulations. Macroparticle merging can increase simulation efficiency and reduce the memory footprint. Smilei implements such a scheme, inspired by that designed by Vranic *et al* [98], that is computationally efficient and conserves energy, momentum and charge within a cell. While Smilei contains modules to handle ionisation, with reference to figure 1.1 these are deemed unnecessary for the laser intensities considered in this thesis.

Parallelisation in practice

In the following discussion, where differences in language occur, objects are given as their ARCHER2 (Smilei) names. The Smilei simulation box consists of a grid of cells as in figure 1.5. The box is decomposed into *patches* consisting of many cells. Patches are arranged into *MPI patch collections* assigned contiguously along a Hilbert curve.

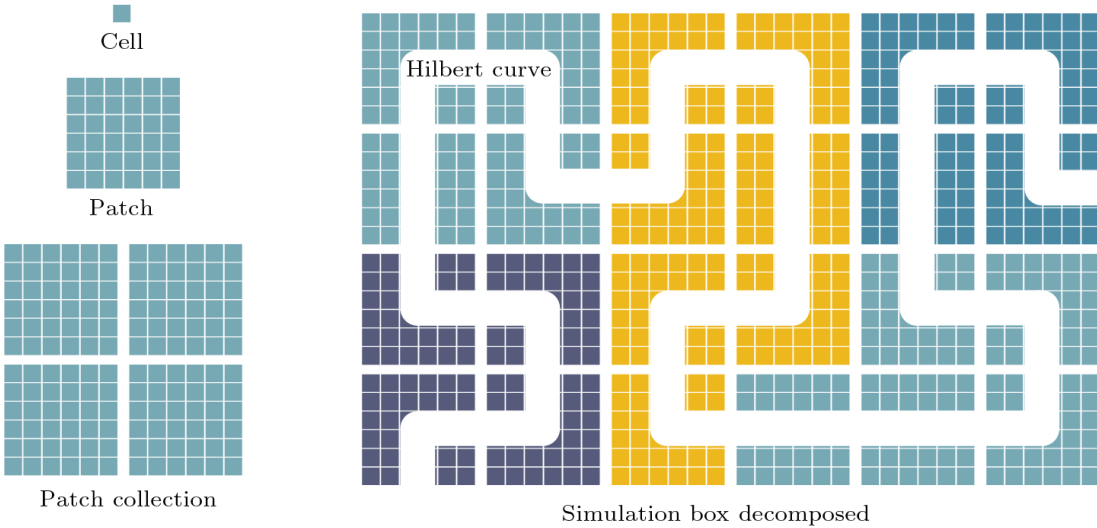


Figure 1.5: Smilei simulation box decomposition into cells, patches and MPI patch collections. Cells are grouped into patches, patches are grouped into MPI patch collections. MPI patches are assigned contiguously along the Hilbert curve.

Archer consists of many *CPUs (cores)* that can each perform computational tasks. CPUs are grouped together into *nodes*. Memory is shared within a node such that all CPUs (cores) in a node can operate on the same data. When optimised, ARCHER2's memory in each node is split into 8 *sockets*. These 8 sockets each perform a *task (MPI process)*. Each task (MPI process) has 16 CPUs (cores) assigned that each perform a *thread*. A thread is a sequence of instructions from the program.

Each task (MPI process) handles one *MPI patch collection*. Threads work through patches. Figure 1.6 represents this division of labour. Threads do not need to wait for other threads in their process to tackle new patches in their MPI patch collection. This is a form of local *dynamic load balancing*. If an MPI patch collection is overloaded, a patch is offloaded to a contiguous MPI patch collection.

There are several considerations for simulation optimisation. Tasks (MPI processes) should always be assigned more patches than threads. To apply the Hilbert curve, it is necessary that the number of patches in each dimension is a power of 2. The less cells in a patch, the more efficient the load balancing, however, the cost of synchronisation between patches increases, although generally the gain in efficiency from load balancing by increasing patch number will win out at later times with increasing efficiency for increased frequency of load balancing [74]. Note

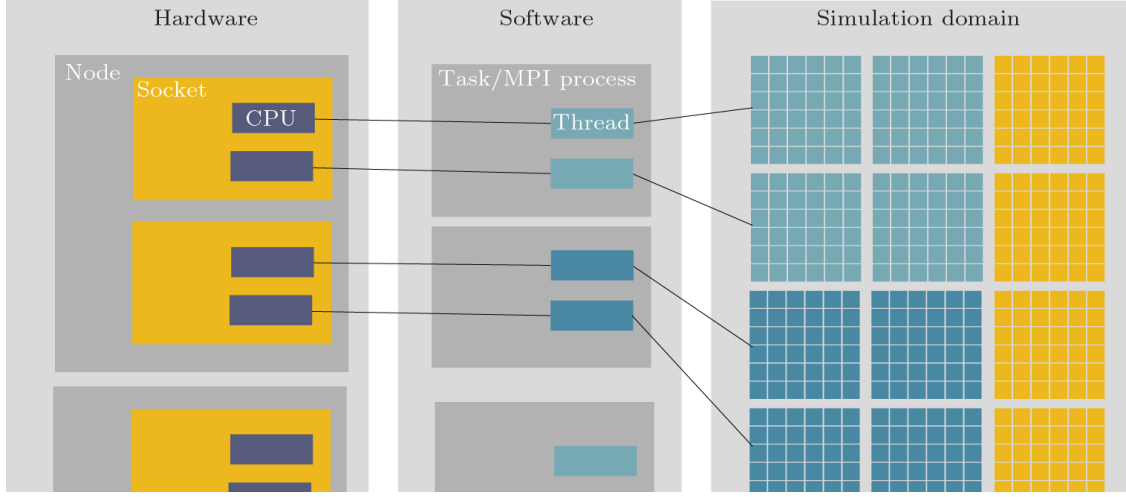


Figure 1.6: Representation of the interaction of the ARCHER2 hardware and software components when running Smilei. Each CPU is assigned a thread, each task is carried out by one socket. A task tackles one MPI patch collection with threads working through patches.

that smaller patches are preferable when there are small regions with large numbers of particles, as in laser-solid surface interactions, however, the minimum patch size is dependent on the shape function of the macro-particles.

Sources of error inherent to PIC codes

Despite their relatively intuitive interpretation, PIC codes are famously finicky and prone to errors, most notably that of numerical self heating⁵. There are three conditions required for stability.

To ensure stability, or at least to minimise instability, there are several conditions which must be met. Naturally, the time step, Δt , and cell size ($\Delta x \times \Delta y \times \Delta z$) must adequately capture all interesting features of a given simulation. Typically such features are plasma wave oscillations,

$$\Delta t \omega_p \ll 1, \quad (1.59)$$

and laser pulse electromagnetic field oscillations or higher order harmonics of the laser pulse if that is of interest, for the n th harmonic

$$\Delta t \omega_L n \ll 1. \quad (1.60)$$

⁵Standard PIC code algorithms are charge and momentum conserving but not energy conserving [74].

Note this also ensures that macroparticles are smaller than the wavelengths of the system, a requirement to ensure they mimic real particles [99]. Relativistic PIC codes must satisfy the much-acclaimed [100] Courant-Friedrichs-Lowy condition,

$$\frac{1}{c\Delta t} > \sqrt{\frac{1}{(\Delta x)^2} + \frac{1}{(\Delta y)^2} + \frac{1}{(\Delta z)^2}}, \quad (1.61)$$

thus preventing light and relativistic particles from crossing a cell in one timestep and generating numerical Cerenkov radiation [101]. As with real plasmas and real particles, to avoid numerical charge fluctuation and ensure collective behaviour of macroparticles,

$$\frac{4}{3}\pi\lambda_D^3 n_{\text{macro}} = N_{\text{D,macro}} \gg 1, \quad (1.62)$$

where n_{macro} is the macroparticle density [101]. To avoid numerical heating, the cell size must resolve the Debye length,

$$\frac{\lambda_D}{\Delta x} \geq 1, \quad (1.63)$$

failure to do so may cause plasma self-heating until the Debye length matches the cell size [101]. Interestingly, Brackbill *et al* [102] observed in their simulations that setting $\lambda_D/\Delta x = 1$ was most effective at reducing spurious heating. Arber *et al* [103] performed extensive simulations exploring this instability. If the Debye length is not resolved, after an initial period of rapid self-heating, the temperature increases linearly and can be modelled as

$$\frac{dT_{\text{eV}}}{dt_{\text{ps}}} = \alpha_H \frac{n_{23}^{3/2} \Delta x_{\text{nm}}^2}{N_{\text{ppc}}}, \quad (1.64)$$

where T_{eV} is the temperature in electron volts, t_{ps} is the time in picoseconds, n is the plasma electron number density in units of 10^{23} cm^{-3} , Δx_{nm} is the cell size in nanometres and N_{ppc} is the number of macroparticles per cell with α_H , the heating coefficient, determined from their simulations. For a top-hat macroparticle shape function they found $\alpha_H = 3000$ with an order of magnitude reduction for every increase in order of the shape function and further improvements from using current smoothing techniques. Note that the heating curves are roughly self similar at all

points and thus while equation 1.64 was established in the linear regime only, its scalings remain useful to compare simulations at all times.

The final instability that shall be discussed is the *finite grid instability*. This is the aliasing error associated with particles properties being deposited at grid points. Is most catastrophic for cold drifting plasmas and depends on the *beam Debye length*,

$$B = \frac{u}{\omega_p \Delta x}, \quad (1.65)$$

where u is the beam speed. While their theory predicts stability for $B > 0.25$, Brackbill *et al* [102] observed instability growth for all beam temperatures in their simulations, although they found the percentage error is a small fraction for $B > 10$.

2

The Zero Vector Potential Absorption Mechanism

Contents

2.1	Motivations and an overview	27
2.2	Introduction	29
2.2.1	ZVP electron bunch energies	36
2.2.2	ZVP bunches oblique incidence scaling and internal bunch structure	38
2.2.3	Defining characteristics of the ZVP mechanism	41
2.3	Numerical simulations of the ZVP mechanism	42
2.3.1	The ZVP mechanism in 3D3V	42
2.4	The ZVP electron bunch	49
2.4.1	Energy absorption in the ZVP regime	58
2.4.2	Unpacking the QED effects of figure 2.11	60
2.4.3	Errors	62
2.5	Planned future work	63
2.6	Conclusions	67

2.1 Motivations and an overview

Throughout the history of experimental science, light has been the primary tool for investigation. Through the creation of synchrotron radiation sources and more recently XFELs, electron bunches have been used to create increasingly specialised light sources for the study of matter of all kinds. At Diamond Light Source in

the UK, electron beams have been used for a diverse range of studies from new drugs to ancient paintings, while at SLAC, the United States' forefront electron accelerator, common applications hail from many disciplines: science, medicine, industry and homeland security. Hence, much research has been done to produce electron bunches with ever greater charge, energy and coherency. Multi-petawatt laser facilities are now available across the globe for the study of laser-plasma interactions at ever greater peak intensities. In the ultra-relativistic regime $a_0 \gg 1$, there is a novel method for high-charge electron bunch creation. Via relativistic effects, a laser pulse organises the electrons at the surface of a solid density plasma into coherent bunches, which are then ejected at high speeds. Those discussed in this thesis have properties rivalling those of forefront accelerators. The quality, charge and duration of the attosecond electron bunches described here would enable the study of the most fundamental interactions of our universe. Electron bunch formation from solid targets has received much interest in recent years [104–111] with some experimental evidence for attosecond electron bunches from intense laser-solid interactions [112–114]. This interest is in part due to their production of higher charge bunches at lower intensities compared to gas targets [112]. Here is proposed a new mass-limited target setup to generate electron bunches with greater charge density. Such electron bunches are fully characterised using PIC simulations to compare their quality to those of existing electron bunch production methods and their energies described via the Zero Vector Potential Mechanism, alongside the theories of the Relativistic Electron Spring [115] and Coherent Synchrotron Emission [116], this is a post-ponderomotive model of attosecond absorption and reflection. This model considers a quasi-static surface equilibrium state analogously to ion acceleration in the hole boring [117] and light sail regimes [118]. ZVP theory has direct relevance to High Harmonic Generation (HHG) due to the known intrinsic link between electron bunches and the reflection mechanism [119, 120]. The implications of ZVP for laser to plasma energy absorption are also considered including at the onset of SF-QED effects.

These results have excited the community to perform experiments to realise these electron bunches for the creation of ultra-bright X-ray pulses: having recently completed an experimental campaign at the ORION laser facility, studying high harmonic generation from such electron bunches, the author's proposal has been accepted to observe the electron bunches directly at the GEMINI PW laser at the Central Laser Facility, UK.

This chapter is organised as follows. Section 2.2 is an introduction to the ZVP mechanism including quantitative calculations of system properties, then in section 2.3.1 the first 3D PIC simulations to observe the ZVP mechanism are presented. Further PIC simulations are presented in section 2.4 focusing now on the hot electron bunches produced via the mechanism. The planned experiment to observe the ZVP mechanism at the GEMINI-PW laser facility is discussed in section 2.5 including details on preparations that must be taken and finally concluding remarks are presented in section 2.6.

2.2 Introduction

Of primary interest in this thesis is the interaction of a relativistically intense short-pulse laser interacting with a solid density plasma target with a sharp density gradient. Now is presented an explanation for this interaction: the ZVP mechanism of attosecond absorption of laser pulse energy, proposed by *Baeva et al* [121] and later developed by *Savin et al* [120, 122].

Theory for laser energy absorption in dense plasmas was first proposed by Wilks and Kruer [123], via a ponderomotive mechanism where plasma electrons are heated directly by the laser pulse via the so-called $\mathbf{J} \times \mathbf{B}$ force. This thesis is interested in the 'post-ponderomotive' regime where the frequency of the relativistic plasma oscillations ($\omega_p \sim \sqrt{S}$) are greater than the $\mathbf{J} \times \mathbf{B}$ induced plasma electron oscillations at $2\omega_L$. The plasma electrons' response is then fast enough to compensate the ponderomotive pressure of the laser pulse with the formation of electrostatic fields between electrons and ions and so respond adiabatically to the applied $\mathbf{J} \times \mathbf{B}$ force. Hence, plasma electrons cannot be heated directly by the laser pulse. Interestingly,

working through this condition suggests the criterion for the ZVP regime is $S > 4$, slightly more constraining than $S > 1$ as is typically stated for the ZVP regime [122]. The resolution comes from understanding the plasma response. The bulk plasma must have $S > 1$ to prevent relativistic transparency and so ensure a laser-surface interaction. Then the ponderomotive pressure of the laser is able to compress the front surface to densities such that the overdensity condition is satisfied, provided the target is of sufficient thickness. Note that to neglect the pre-adiabatic formation phase requires a sufficiently steep density gradient around the relativistic critical density surface (where $S = 1$) to shift the main interaction to a region where this condition on the overdensity is satisfied. Pre-plasma formation and scale length will be discussed in great detail in the following chapter. In short, the technology exists to control this phenomenon.

Provided all conditions are met, the ponderomotive pressure of the laser pulse compresses the electrons at the front surface of the plasma and so shifts the laser-plasma surface interaction to plasma densities well beyond the relativistic critical density, leaving in its wake a positive space charge. This electron-ion charge separation leads to the formation of a *pseudo-capacitor* electrostatic field. Having entered a regime of adiabaticity, the plasma skin layer is confined within a potential well consisting of the ponderomotive pressure of the laser pulse and the Coulomb potential of the pseudocapacitor field. Thus is formed a high density and spatially thin electron bunch (sometimes referred to as an electron sheath in the literature [115]) at the plasma surface.

To understand this system, consider now a relativistic linearly polarised laser pulse obliquely incident, at an angle of incidence θ , on a semi-infinite plasma, existing for $x \geq 0$ as in figure 2.1.

The Hamiltonian of a single electron confined within the potential well [79] is

$$\mathcal{H} = c\sqrt{m_e^2c^2 + |\mathbf{p}|^2} - e\Phi. \quad (2.1)$$

Here, the second term of equation 2.1 describes the contribution to the electron's energy from the electrostatic potential, Φ , of the pseudo-capacitor. The first term is

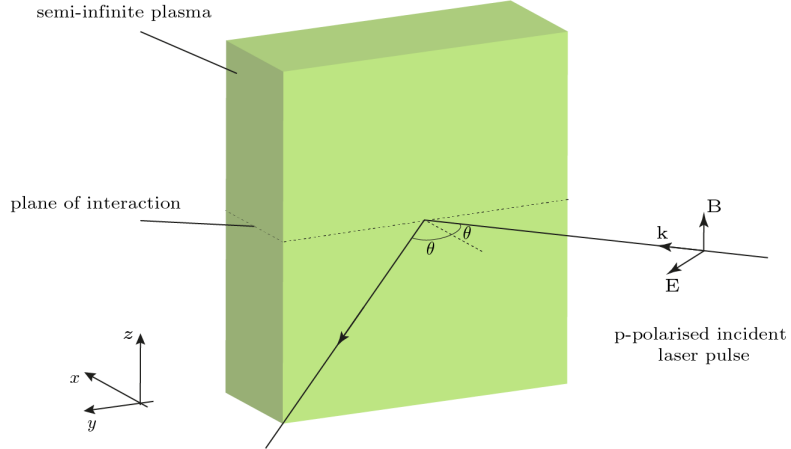


Figure 2.1: Diagram of a p-polarised laser pulse incident at angle θ specularly reflected from a solid density plasma. By considering the Lorentz force equation, it is clear that all forces and therefore all plasma particle dynamics are confined to a plane.

the electron energy, U , extracted from the invariant of the relativistic 4-momentum of the electron, $\mathbf{P}^\mu = (U/c, \mathbf{p})$,

$$\mathbf{P}_\mu \mathbf{P}^\mu = \frac{U^2}{c^2} - |\mathbf{p}|^2 = m_e^2 c^2. \quad (2.2)$$

Decomposing the electron's 3-momentum into orthogonal components: p_{prop} , along the laser propagation direction, p_{pol} , along the polarisation axis of the laser pulse and p_\perp , perpendicular to both, there are two simplifications to be made. Firstly, by canonical conservation of transverse momentum, $p_{\text{pol}} = eA$, where A is the laser vector potential amplitude. Secondly, in the case of a p-polarised laser pulse (the known optimum for ZVP electron bunch generation [120] and HHG [124]), with reference to figure 2.1 and the Lorentz force law, the forces at play confine the electron trajectory to the $p_{\text{prop}}-p_{\text{pol}}$ plane and the essential interaction geometry is two-dimensional. This is provided one considers length scales smaller than the focal spot of the laser pulse on the target, such that variation of the ponderomotive pressure with the third dimension can be neglected.

Explicitly, the Hamiltonian can be written as

$$\mathcal{H} = c\sqrt{m_e^2 c^2 + p_{\text{prop}}^2 + e^2 A^2} - e\Phi. \quad (2.3)$$

From equation 2.3 it is clear that should the vector potential pass through zero, one of the walls of the potential well is totally suppressed, allowing electrons in the skin

layer to escape the plasma, breaking adiabaticity. The necessity of vector potential zeros for this violent reconstruction of the plasma surface led Baeva *et al* [121] to coin the term ‘Zero Vector Potential’ mechanism to describe this process. Indeed, while elementary electromagnetism tells us a laser pulse will exponentially decay within a skin layer of a plasma without passing through zero, Baeva *et al* [121] were able to demonstrate in PIC simulations that for this regime, zeros do exist and do propagate through the skin layer in this non-linear regime. The explanation relies on a Doppler shift in the laser field due to the relativistic motion of the ablating plasma surface, and the mathematical formalism of this process proceeds as follows.

As the ZVP mechanism is a relativistic phenomenon, it is essential to perform a relativistic analysis. Since all electrons are accelerated by the relativistic laser pulse to approximately speed c , surface electrons undergo similar trajectories and act collectively, oscillating in the laser pulse field. Consider first a transformation to the frame of reference where the laser pulse is normally incident to the plasma surface, this frame travels at velocity $\mathbf{v} = (c \sin \theta) \hat{\mathbf{y}}$ with electrons streaming at $-\mathbf{v}$. Using equation 2.2, $U = \gamma m_e c^2$ and integrating equation 1.50 in the boosted frame noting $p_T(t = 0) = \gamma_v m_e v = m_e c \sin \theta \cos \theta$,

$$\gamma^2 = 1 + (a_0 + \sin \theta \cos \theta)^2 + \left(\frac{p_{\text{prop}}}{m_e c} \right)^2, \quad (2.4)$$

where all parameters are in the boosted frame. Using $\mathbf{p} = \gamma m_e \mathbf{v}$, the longitudinal velocity is

$$v_{\text{prop}} = \frac{\tilde{p}_{\text{prop}} c}{\sqrt{1 + (a_0 + \sin \theta \cos \theta)^2 + \tilde{p}_{\text{prop}}^2}}, \quad (2.5)$$

where $\tilde{p}_{\text{prop}} = p_{\text{prop}}/m_e c$. Thus, should the transverse vector potential pass through $-\sin \theta \cos \theta$, zero for normal incidence, the surface is able to propagate towards the laser pulse at very close to speed c . Transforming back to the laboratory frame at the peak of ablation ($\mathbf{u} \approx -c \hat{\mathbf{x}}$) and using the equations for relativistic velocity addition,

$$\mathbf{u}'_{\parallel} = \frac{\mathbf{u} - \mathbf{v}}{1 - \mathbf{u} \cdot \mathbf{v}/c^2}, \quad (2.6)$$

$$\mathbf{u}'_{\perp} = \frac{\mathbf{u}_{\perp}}{\gamma_v (1 - \mathbf{u} \cdot \mathbf{v}/c^2)}, \quad (2.7)$$

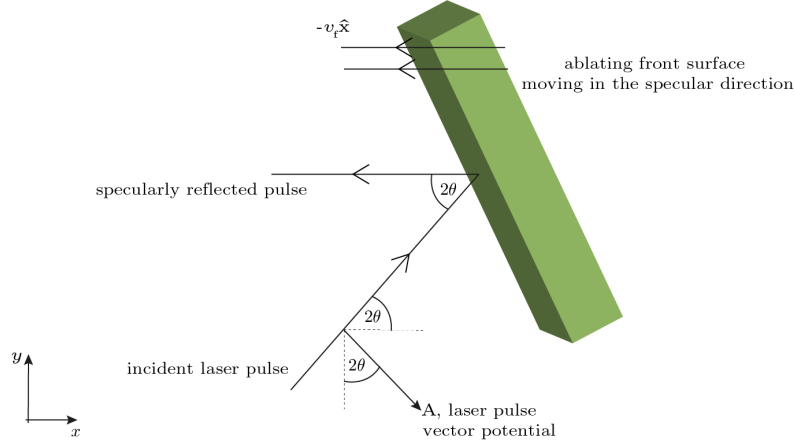


Figure 2.2: Diagram of a *p*-polarised laser pulse incident on an ablating overdense plasma. The laser is incident obliquely at an angle of θ and is reflected specularly. The plasma ablates specularly also. The interaction geometry is confined to a 2D plane.

where $\gamma_v = 1/\sqrt{1 - |\mathbf{v}|^2/c^2}$ [73], one finds that this peak ablation at speed $\approx c$ occurs now in the specular reflection direction. Simultaneity is broken and co-move along the surface with the incident laser pulse wavefronts.

Transform now to the rest frame of the ablating front. Beyond the relativistic critical density surface, the vector potential of the laser pulse decays evanescently. At the spatial centre of the laser pulse, it can be described simply by

$$\mathbf{A}'_{\text{L}}(t', r') = A'_0 \cos(\omega'_{\text{L}} t') \exp(-r'/\delta') \hat{\mathbf{r}}'_{\text{pol}}, \quad (2.8)$$

where the primed symbols indicate that these quantities are measured in the rest frame of the expanding front, A'_0 is the vector potential amplitude and ω'_{L} is the frequency of the laser pulse, r' is the propagation distance of the laser into the plasma, δ' is the skin depth and $\hat{\mathbf{r}}'_{\text{pol}}$ a unit vector defining the polarisation direction of the laser pulse. Un-primed coordinates will indicate the lab frame measurements.

While previous demonstrations of the existence of vector potential zeros assumed that the ablation occurs normal to plasma surface, it is necessary to confirm that zeros are still predicted for specular ablation. Consider a *p*-polarised laser pulse confined to the x - y plane incident with an angle of incidence θ on an ablating overdense plasma expanding with velocity $-v_f \hat{x}$ in the lab frame, as in figure 2.2.

The direction of polarisation is

$$\hat{\mathbf{r}}_{\text{pol}} = \hat{\mathbf{x}} \sin 2\theta - \hat{\mathbf{y}} \cos 2\theta \quad (2.9)$$

and the velocity of the rest frame of the ablating front relative to the lab frame is $-v_f \hat{\mathbf{x}}$.

Applying the Lorentz transformation to the electromagnetic 4-potential, \mathbf{A}^μ , where Λ_μ^ν is given by equation 1.30, immediately from the y -coordinate transformation,

$$A'_L \cos 2\theta' = A_L \cos 2\theta. \quad (2.10)$$

Applying the headlight effect for a source moving at an angle 2θ to the boosted frame (a full derivation is given in Appendix A.2),

$$\cos(2\theta') = \frac{\cos(2\theta) - \beta}{1 - \beta \cos(2\theta)} \quad (2.11)$$

and rearranging equation 2.10, the vector potential in the lab frame is

$$A_L = \frac{1 - \beta \sec(2\theta)}{1 - \beta \cos(2\theta)} A'_0 \cos(\omega'_L t') \exp(-r'/\delta'). \quad (2.12)$$

Writing the boosted frame space-time coordinates in terms of the lab frame coordinates,

$$ct' = \gamma(ct - \beta x), \quad (2.13)$$

$$x' = \gamma(x - \beta ct), \quad (2.14)$$

yields

$$A_L = A_0 \cos(\omega_L t - kx) \exp\left(-\frac{\sqrt{(x - \beta ct)^2 + (y/\gamma)^2}}{\delta}\right), \quad (2.15)$$

where

$$A_0 = \frac{1 - \beta \sec(2\theta)}{1 - \beta \cos(2\theta)} A'_0, \quad (2.16)$$

$$\omega_L = \gamma \omega'_L, \quad (2.17)$$

$$k = \frac{\beta \gamma \omega'_L}{c}, \quad (2.18)$$

$$\delta = \frac{\delta'}{\gamma}. \quad (2.19)$$

The oscillatory term in equation 2.15 demonstrates the propagation of vector potential zeros within the plasma target. From the structure of this term it

would appear that these zeros are expelled from the plasma along the specular direction at a speed

$$v_\phi = \frac{\omega_L}{k} = \frac{c}{\beta} = -\frac{c^2}{v_f}. \quad (2.20)$$

While in their original ZVP paper Baeva laid some doubt on their version of this calculation, instead suggesting similarity theory predicts zeroes propagate at speed c [121], the theory of High Harmonic Generation rejects this alternative. It is well known that the emission of reflected radiation occurs primarily at the point where the transverse vector potential passes through zero [119] but equally that the width of the radiated pulse depends on the advance time emission point [125]. If the zeroes moved at speed c , then the observed emitted pulse would be infinitely thin, producing radiation with excellent coherency in all cases. In practice however, simulations have suggested advanced time bunch widths are finite with the width reducing as the laser intensity is increased [125]. This is precisely what is predicted by equation 2.20, as the laser intensity increases, v_f increases and thus the zeroes propagate closer to the speed of light, reducing the advanced time bunch width.

To summarise, for a sufficiently intense laser pulse, electrons on the radiated surface of a solid target are accelerated by the laser to relativistic velocities at a fraction of a laser pulse cycle and therefore electrons both follow similar trajectories and are able to respond adiabatically to the $\mathbf{J} \times \mathbf{B}$ force of the laser pulse. They form into a high charge density spatially thin coherent electron bunch on the front surface of the plasma but displaced inwards from the approximately immobile ions via the ponderomotive pressure of the laser. This charge separation generates a longitudinal electrostatic pseudocapacitor field that confines electrons to a potential well on the front surface of the plasma, preventing further propagation of the electron bunch into the plasma bulk. When the zero of the vector potential passes through the electron bunch, the ponderomotive pressure instantaneously vanishes and electrons are ejected specularly from the target, copropagating with the zeroes and gaining energy as they discharge the pseudocapacitor field. The electron bunch is then rotated by the laser pulse and launched into the bulk at high energy, as it does so emitting coherent synchrotron radiation in transmission and reflection.

2.2.1 ZVP electron bunch energies

In [121], Baeva *et al* propose energy scalings for electron bunches produced in the ZVP regime as a function of the incident laser pulse intensity and plasma density. Later this was then extended to three-dimensions (3D) by Savin *et al* [120]. What follows is that discussion with closer consideration of both the constants of proportionality and their consequences.

Consider again the semi-infinite block of plasma presented in figure 1.2, normally irradiated by a laser pulse with wavelength λ_L and peak electric field, E_L . It is now the ponderomotive pressure of the laser that displaces the electron fluid. The electron surface moves inwards until the pressure exerted by the peak instantaneous ponderomotive pressure of the laser pulse cycle,

$$\mathbf{P}_L = \epsilon_0 E_L^2 \hat{\mathbf{x}} = \epsilon_0 \left(\frac{a_0 \omega_L m_e c}{e} \right)^2 \hat{\mathbf{x}} \quad (2.21)$$

is equal and opposite to the pressure exerted by the pseudo-capacitor field,

$$\mathbf{P}_C = \frac{QE_C}{\sigma} \hat{\mathbf{x}} = - \frac{(en_e \Delta x)^2}{\epsilon_0} \hat{\mathbf{x}} \quad (2.22)$$

from equations 1.16 and 1.17. Equating the magnitudes of \mathbf{P}_L and \mathbf{P}_C , the maximum displacement inwards of electrons is

$$\Delta x \hat{\mathbf{x}} = \frac{c}{\omega_L} \frac{a_0}{\bar{n}_e} \hat{\mathbf{x}} = \frac{1}{kS} \hat{\mathbf{x}}, \quad (2.23)$$

where k is the wave-vector of the laser pulse. Correspondingly,

$$E_C = \frac{en_e}{\epsilon_0} \Delta x = \frac{\omega_L c m_e a_0}{e} = E_L. \quad (2.24)$$

Applying the results of equations 2.23 and 2.24, when the ponderomotive pressure vanishes and the electron bunch is launched across the pseudo-capacitor, the relativistic kinetic energy gained by a single electron is

$$T = \int \mathbf{F} \cdot d\mathbf{s} = \int_{\Delta x}^0 -eE_C dx = \int_{\Delta x}^0 -\frac{en_e x}{\epsilon_0} dx = \frac{1}{2} m_e c^2 \frac{a_0^2}{\bar{n}_e} \quad (2.25)$$

or an electron gamma factor,

$$\gamma = \frac{1}{\sqrt{1 - \beta^2}} = 1 + \frac{a_0^2}{2\bar{n}_e}. \quad (2.26)$$

Assuming all displaced electrons are captured by the potential well and launched as a coherent bunch, the total number of electrons in the bunch is

$$N_e = n_e \sigma \Delta x = \frac{\sigma a_0 n_c}{k} = \sigma \epsilon_0 E_L \quad (2.27)$$

and hence, the total kinetic energy of the electron bunch is

$$U_{ZVP} = N_e T = \frac{\sigma n_c}{k} \times \frac{1}{2} m_e c^2 \frac{a_0^3}{\bar{n}_e}. \quad (2.28)$$

It is now interesting to compare equation 2.28 to the laser energy deposited upon the plasma surface and therefore consider what fraction of the laser energy can be absorbed via the ZVP mechanism. Using $E_C = E_L$, equation 2.28 can be rewritten as

$$U_{ZVP} = \frac{1}{2\omega_L S} \sigma c \epsilon_0 E_L^2. \quad (2.29)$$

For the case of normal incidence, bunches are produced at a frequency of $2\omega_L$, naturally following the frequency of the $\mathbf{J} \times \mathbf{B}$ force. Assuming a sinusoidal plane wave incident with surface area σ , the energy available during the pushing phase (a quarter-cycle) is

$$U_{L,1/4} = \sigma \frac{T}{4} \langle I_L \rangle = \frac{2\pi}{8\omega_L} \sigma c \epsilon_0 E_L^2. \quad (2.30)$$

Hence,

$$\eta_{ZVP} = \frac{U_{ZVP}}{U_{L,1/4}} = \frac{2}{\pi S}. \quad (2.31)$$

Interestingly, this analytical result predicts the trend observed by A. Savin [122] in PIC simulations both in magnitude and in scaling. Indeed, A. Savin demonstrated

$$\eta_{ZVP} \sim S^{-1.000(3)}, \quad (2.32)$$

however, this result led A. Savin to conclude that increasing S reduces absorption, increasing the energy in the reflected HHG beam thus increasing high harmonic efficiency, seemingly in tension with the results of other works [115, 125]. The resolution arises from awareness of two distinct conversion efficiencies that describe the reflected harmonic spectrum: the total conversion efficiency into the full reflected beam and the conversion efficiency for individual harmonics. While the total

conversion into the reflected beam decreases for decreasing S , the slope of the harmonic spectrum also decreases, reducing HHG efficiency. Indeed, high X-ray harmonic efficiency necessitates high reflection inefficiencies due to the production of ZVP electron bunches as higher energy bunches produce more coherent reflected radiation [125], a caveat not often considered in the quest for higher-order harmonics. The impact of the ZVP mechanism on HHG will be discussed in great detail in the following chapter.

The expressions for energies in equations 2.25 and 2.28 require the electron bunch to fully discharge the pseudo-capacitor before interaction with the subsequent laser pulse peak. Since the electron bunch travels at speed $\approx c$, the peak displacement (and thus the pseudo-capacitor width) must satisfy

$$\Delta x \leq \frac{\lambda}{8}. \quad (2.33)$$

Using equation 2.23, it is clear equation 2.33 is satisfied for $S \geq 1.3$ for normal incidence.

2.2.2 ZVP bunches oblique incidence scaling and internal bunch structure

This section is inspired by ideas from the work of Gonoskov *et al* [115] and Vincenti *et al* [117] to extend the theory of the ZVP mechanism for energy absorption to the more practical¹ case of oblique incidence.

Provided the plasma-vacuum boundary is sufficiently steep, the plasma electrons will respond adiabatically to the laser pulse and arrange themselves to form a pseudocapacitor longitudinal electric field E_C at the plasma surface. At all points in this adiabatic ‘pushing’ phase, the surface electrons will be in a quasi-static equilibrium *i.e.* there will be a balance between the electromagnetic forces on them. Consider again the laser pulse incident on a solid density plasma existing for $x > 0$ at angle θ . Transforming to the frame of reference in which the laser is normally incident (quantities in this frame are indicated by the primed symbol), the electron

¹Not only is this more feasible in experiment but has been shown to optimise HHG [115].

and ion bulk plasma species stream at velocity $\mathbf{v}_d = -c \sin \theta \hat{\mathbf{y}}$. Applying the Lorentz force law along the longitudinal direction ($\hat{\mathbf{x}}$), for a displacement of the electron fluid x'_e (one assumes that the expression for a single electron at the surface describes the surface since all electrons follow similar trajectories), travelling at speed \mathbf{v}' ,

$$-e(\mathbf{v}'(x'_e) \times (\mathbf{B}'_L(x'_e) + \mathbf{B}'_i(x'_e)) \cdot \hat{\mathbf{x}} + E'_C(x'_e)) = 0, \quad (2.34)$$

where the laser magnetic field,

$$B'_L = \frac{m_e \omega'_L a_0 \sin(\omega'_L t' - k' x'_e)}{e} \hat{\mathbf{z}} \quad (2.35)$$

and B_i is the magnetic field generated by the uncompensated ion current, $\mathbf{J}_i = Zn'_i(x'_e)\mathbf{v}_d$, where the electron fluid has been displaced. As before, from equation 1.17,

$$E'_C = \frac{en'_e x'_e}{\epsilon_0}. \quad (2.36)$$

Applying Maxwell-Ampère's Law, equation 1.1c, and noting that by symmetry there can be no variation in the magnetic field with y' or z' , it becomes clear that

$$-\frac{d(\mathbf{B}'_i)_{z'}}{dx'} = \mu_0(\mathbf{J}_i)_{y'}. \quad (2.37)$$

Integrating equation 2.37 from $-\infty$ to x'_e , noting that $\mathbf{B}_i = 0$ at infinity and assuming a constant density profile n'_i for $x > 0$ with $Zn_i = n_e$,

$$\mathbf{B}'_i(x'_e) = \mu_0 en'_e x'_e c \sin(\theta) \hat{\mathbf{z}}. \quad (2.38)$$

Using equations 2.35, 2.36 and 2.38 and making the reasonable approximation that the relativistic electrons on the surface move at speed $v'_y \approx \pm c$ at peak displacement ($x'_e = x'_p$), 2.34 can be written as

$$-e \left(\pm c \left(\pm \frac{m_e \omega'_L a_0}{e} + \mu_0 en'_e x'_p c \sin \theta \right) + \frac{en'_e x'_p}{\epsilon_0} \right) = 0. \quad (2.39)$$

For the laser to be in the pushing phase, the first term must be negative, corresponding to \mathbf{v}' and \mathbf{B}'_L having the opposite sign, hence,

$$c \left(-\frac{m_e \omega'_L a_0}{e} \pm \mu_0 en'_e x'_p c \sin \theta \right) + \frac{en'_e x'_p}{\epsilon_0} = 0, \quad (2.40)$$

where here the \pm tracks the sign of \mathbf{v}' . After some manipulation, one arrives at

$$x'_p = \frac{1}{k'S'(1 \pm \sin \theta)}. \quad (2.41)$$

Transforming back to the lab frame,

$$x_p = \frac{\cos^2 \theta}{kS(1 \pm \sin \theta)}. \quad (2.42)$$

Convincingly this reduces to equation 2.23 for $\theta = 0$ and predicts the suppression and enhancement of the two surface oscillations per laser pulse cycle. Explicitly, for a laser pulse propagating at $y = x \tan \theta$, the peak displacement of the electron surface is enhanced for \mathbf{B}_L in the $+\hat{\mathbf{z}}$ -direction and suppressed for \mathbf{B}_L in the $-\hat{\mathbf{z}}$ -direction.

Again, integrating to find the work done as the electron bunch accelerates across the pseudocapacitor,

$$T(\theta) = \int \mathbf{F} \cdot d\mathbf{s} = \frac{1}{2} m_e c^2 \frac{a_0^2}{\bar{n}_e} \frac{\cos^4 \theta}{(1 \pm \sin \theta)^2}. \quad (2.43)$$

While it was to be expected that a component of the electric field acting into or out of the plasma would change the magnitude of the displacement, this result suggests that increasing the angle of incidence can increase the electron energy gain in the enhanced cycle more than the decrease in the suppressed cycle. Note that this is to be expected as it is known that HHG efficiency is improved for non-zero angle of incidence [115, 125]. It would be interesting to explore whether the presence of an external magnetic field could be applied to mimic the effect of oblique incidence by replacing the magnetic field due to the uncompensated ion current.

While this model would suggest an optimal angle for electron energy and therefore of HHG of $\pi/2$, if $\theta > \pi/4$, then, if the relativistic electron bunch is travelling at c along the specular reflection direction, the subsequent laser peak amplitude will never ‘catch up’ with the electron bunch, and electrons can escape, generating high charge electron bunches in reflection as observed in experiment by Lin *et al* [112], but reducing the efficiency of HHG.

Finally, the total bunch energy as a function of θ ,

$$U_{ZVP}(\theta) = \frac{\sigma n_c}{k} \times \frac{1}{2} m_e c^2 \frac{a_0^3}{\bar{n}_e} \frac{\cos^6 \theta}{(1 \pm \sin \theta)^3}. \quad (2.44)$$

Thus oblique incidence can increase laser absorption efficiency for higher S plasmas which are currently more easily accessed compared to the more optimal low S plasmas.

2.2.3 Defining characteristics of the ZVP mechanism

In her original paper on the ZVP mechanism, T. Baeva *et al* [121] outlined 6 defining characteristics of the ZVP mechanism, namely,

1. The existence of vector potential zeros moving through the skin layer in the laboratory frame;
2. The existence of zeroes in the incident laser pulse vector potential required for the formation of fast electron bunches;
3. The generation of fast electron bunches with ultra-short temporal duration;
4. That such fast electron bunches follow the energy scalings of equations 2.25 and total energy 2.28;
5. Injection of the fast electron bunches is along the propagation axis of the laser pulse;
6. There must be an intrinsic link must exist between the fast electron bunches and coherent X-ray HHG;

with the moving zeros within the skin layer being the defining delineator between this post-ponderomotive regime of laser pulse energy absorption and all other proposed mechanisms. While such observational requirements are far beyond the reaches of current experimental know-how, numerical simulations in both 1- [121] and 2-dimensions [120] have confirmed the above points. Now is presented the first 3D simulations attempting to demonstrate these criteria.

2.3 Numerical simulations of the ZVP mechanism

This thesis relies on the analysis of 1,2 and 3D PIC simulations, primarily using the massively-parallel and open-source simulation code Smilei [74]. Simulation parameters will be provided throughout.

2.3.1 The ZVP mechanism in 3D3V

The 3D simulation results are presented in figure 2.3 alongside comparison to an equivalent 2D simulation. Simulation parameters are given in table 2.1, such parameters are compatible with the 10 PW ELI-NP state-of-the-art short pulse laser facility [126] and foam targets. Figure 2.3c) clearly demonstrates the existence of high energy density electron bunches propagating through the plasma bulk in the direction of the laser pulse. Note that this ZVP criterion is a direct consequence of conservation of transverse momentum inside the plasma bulk where the laser fields cannot propagate. Figure 2.3b) shows these bunches escape to the rear of the bulk but lose energy as they do so. Looking now at figure 2.3e) and the internal structure of the plasma bulk. These bunches drive two-stream and filamentation instabilities [127]. The bulk propagating bunches are accompanied by higher density electron bunches to either side of the plasma block with the side switching every half laser pulse cycle.

The thickness of the target does not impact the interaction and is chosen for computational efficiency, indeed it is standard to consider such targets of thickness $\geq \lambda_L$ as bulk targets [70], however, for sufficiently long pulse durations, the effect of hole boring necessitates thicker targets to make this approximation as will be required in the following chapter.

For the 3D simulations only, particles were initialised randomly instead of regularly to avoid numerical errors. Regularly initialised plasma blocks in 3D simulations blow apart very quickly due to spurious large amplitude fields generated on the large plasma surface due to macroscopic electron-ion charge separation at initialisation. 2D simulations with randomly initialised particles tend to produce nano-structures reminiscent of cosmic filaments. This would appear erroneous

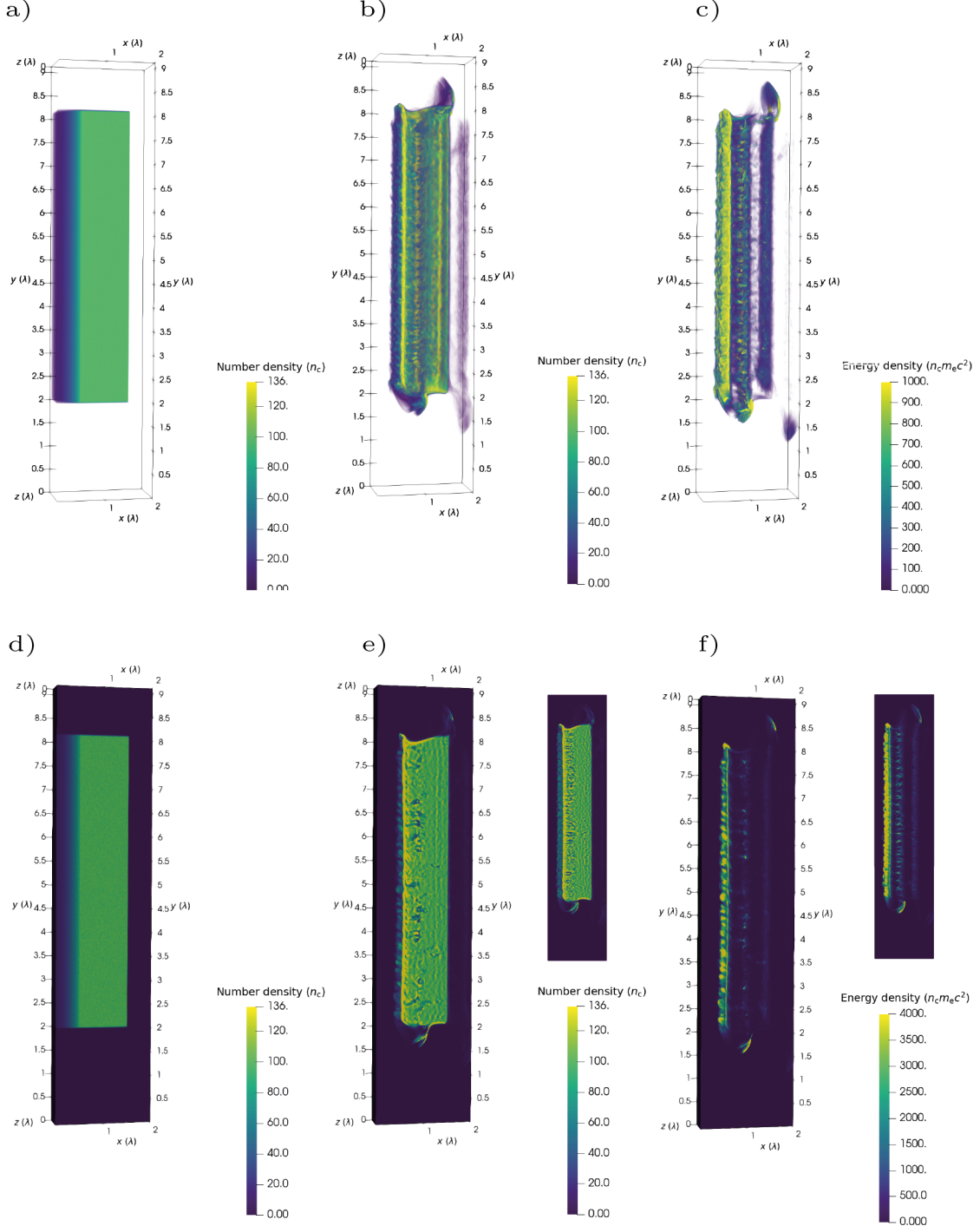


Figure 2.3: Simulation results from a 3D PIC simulation of the ZVP mechanism. a) The initialised electron number density. b) The electron number density several cycles later, the plasma bulk is intact, however there is evidence of instabilities and electron bunches propagating through and around the plasma. c) The electron kinetic energy density at the same timestep. Note that the scale has been clipped to enable observation of both electron bunches propagating through and around the plasma bulk. Significantly higher energy density, corresponding to a higher charge density and attosecond duration for the electron bunches propagating around the bulk. d-f) Plots clipped through $z = \lambda_L/2$ for a-c) respectively for better clarity on the internal structure of the plasma bulk. The accompanying plots for figure e) and f) are corresponding 2D PIC simulation results.

Laser (3D, normal incidence)		
Parameters	Real	Sim
Wavelength, λ (nm)	1060	2π
Angular frequency, ω_L (fs $^{-1}$)	1.8	1
Beam waist, w_L (nm)	6λ	12π
Focal point, (x_f, y_f, z_f) (nm)	$(0.5\lambda, 5\lambda, 0.5\lambda)$	$(\pi, 10\pi, \pi)$
Spatial envelope, E_i , $i = y, z$	$E_i \sim e^{-(i-i_f)^2/w_L^2}$	
Temporal envelope, E_t	$E_t \sim e^{-(t-4\lambda/c)^2/(4\lambda/3c)^2}$	
Simulation box		
Size, $x \times y \times z$ (nm)	$2\lambda \times 9\lambda \times \lambda$	$4\pi \times 18\pi \times 2\pi$
Sim length (fs)	35.22	20π
Spatial resolution, Δx (nm)	$\lambda/128 = 8.28$	0.0491
Temporal resolution, Δt (as)	$\Delta x/11c = 2.51$	0.00446
Collisionless, pre-ionised randomly-initialised aluminium plasma		
Electron x profile, $n(x)$	$\begin{cases} n_e & \text{for } 2\lambda \leq x \leq 3\lambda, \\ n_e e^{(x-2\lambda)/0.2\lambda} & \text{for } x \leq 2\lambda. \end{cases}$	
Electron y profile, $n(y)$	$\begin{cases} 1 & \text{for } 2\lambda \leq y \leq 8\lambda, \\ 0 & \text{otherwise.} \end{cases}$	
Electron z profile, $n(z)$	$\begin{cases} 1 & \text{for } 0.125\lambda \leq z \leq 0.875\lambda, \\ 0 & \text{otherwise.} \end{cases}$	
Ion profile, $n_i(x, y, z)$	$n_i = n(x)n(y)n(z)/13$	
Macro-electrons per cell	729	
Macro-ions per cell	8	
Ion temperature, T_i (keV)	0	0
Electron temperature, T_e (keV)	10	0.02
Stability criteria		
$\lambda_D/\Delta x$	0.288	
$1/\Delta t \omega_p$	24.4	
$\Delta x/c\Delta t$	11	
Macro-particles in the Debye sphere	210	

Table 2.1: Simulation parameters in both real and normalised Smilei simulation units for the 3D3V simulations.

as it is not present in equivalent 3D simulations and is likely due to the lack of degrees of freedom available in the system. This error can be reduced by increasing the plasma temperature.

The plasma specifications were chosen to minimise computational load while ensuring numerical convergence, requiring over 100 billion macroparticles. The electron temperature is raised significantly higher than that which would be expected in such a laser-plasma system so as to resolve the Debye length. Anticipated plasma temperatures are calculated using 1D HYADES simulations in the following chapter. While this temperature is unphysical and will lead to some small plasma expansion over the course of the simulation, the temperature remains negligible compared to that imparted to the electron bunches by the laser pulse. The striking similarity between the 2 and 3D simulation results is a natural consequence of the 2D nature of the interaction geometry. It is, however, still reassuring to show that previous work withstands the stringent test of real universe geometry and the ZVP mechanism is not lost in the chaos.

Convergence of 3D simulations

The 3D simulation parameters were chosen to be consistent with previous work on the ZVP mechanism, however, such simulations are cumbersome, limiting the number of simulations it is feasible to run. In order to query the defining characteristics outlined by Baeva, a lower resolution simulation was performed with similar parameters to the initial simulation. Comparisons between the simulation outputs are made in figure B.1 in appendix B.1. Good convergence is qualitatively demonstrated by the presence of characteristic features of the ZVP mechanism. While the instabilities are similar in structure, the change in seeding changes their exact positions. As instabilities are not the focus of this thesis this variation is of no cause for concern, however, while the characteristics remain similar, some caution must be taken with any quantitative results.

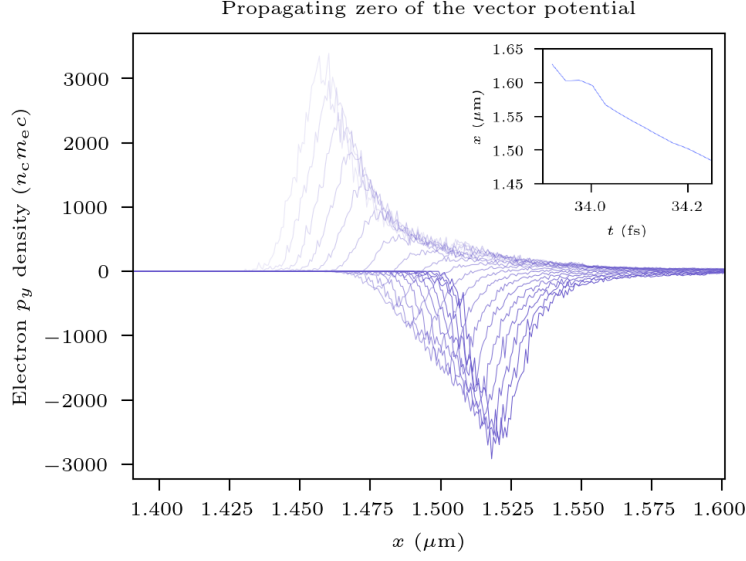


Figure 2.4: Propagation of zeroes through the ablating ZVP electron bunch via the proxy of transverse momentum conservation. The zero of the vector potential exists where the transverse momentum is macroscopically zero. Each line represents a timestep with time increasing with decreasing colour. With increasing time the bunch and the zero move in the $-\hat{x}$ -direction with the zero overtaking the electron bunch. The inset tracks the position of the zero of the vector potential with time.

Confirmation of ZVP in 3D

Figure 2.4 tracks the transverse momentum distribution along the polarisation axis of the laser pulse of an electron bunch during its ablative journey, clearly demonstrating the existence of a singular zero of the vector potential propagating through the electron bunch and away from the plasma bulk.

The zero propagates at a speed of $\approx 1.4c$. In this simulation, the zero propagates through the bunch before it finishes crossing the pseudocapacitor and thus before it has acquired its maximum velocity. As previously discussed this reduces the coherency of the emitted radiation, this provides a new perspective from which to consider optimisation of HHG.

Further simulation results are presented in figure 2.5.

In figures 2.5a)-d), comparisons are made in the electron energy distributions for simulations with zeros present in the vector potential (linearly polarised) and without (circularly polarised). Clearly zeroes are required for the formation of high

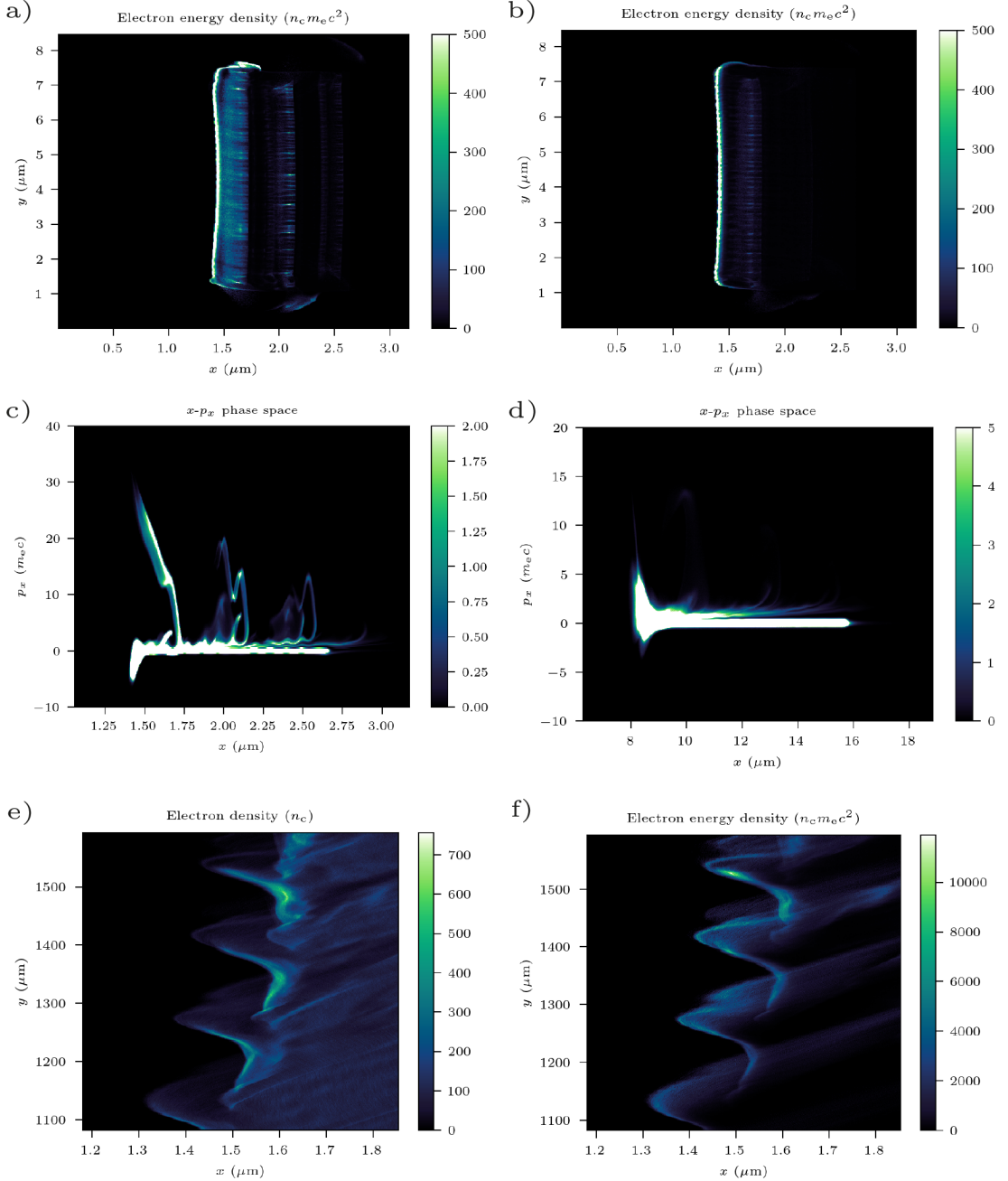


Figure 2.5: Electron dynamics in a 3D PIC simulation. a) and b) Electron energy density for linearly and circularly polarised laser pulses respectively. c) and d) Electron longitudinal momentum for linearly and circularly polarised laser pulses respectively. e) Electron density at the plasma surface streaked in time. f) Electron energy density at the plasma surface streaked in time.

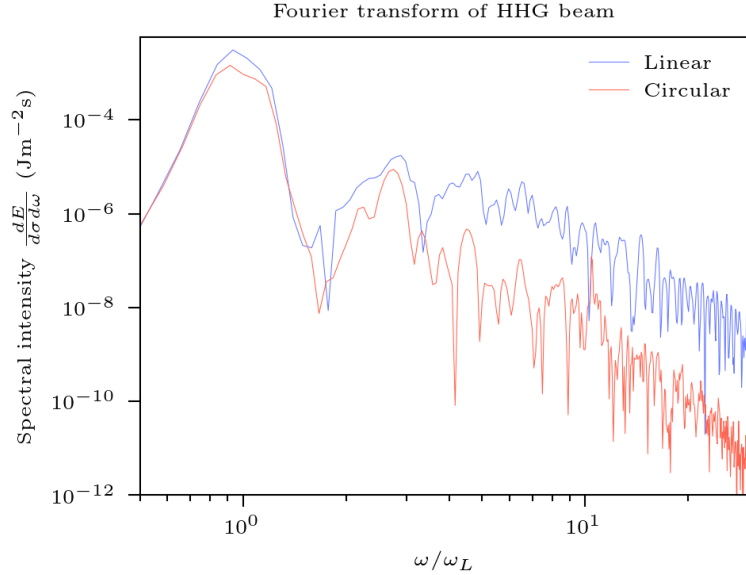


Figure 2.6: The Fourier transform of the reflected laser pulse in 3D PIC simulations both with and without zeroes in the vector potential.

energy, short duration attosecond bunches. From figure 2.5a) it is clear that electron bunches are injected and propagate through the plasma bulk in the laser propagation direction. Figure 2.5c) demonstrates the quasi-monoenergeticity of the high energy electron bunches as initially identified in 1D by Baeva. Although the shape in the phase space is more complex in 3D, the attosecond duration at a given energy is retained. Figures 2.5e) and f) describe the surface dynamics. One can observe the high density bunches on the front surface with the peak in energy density occurring after acceleration across the pseudocapacitor. Figure 2.5f) also explains the shape of the spectrum of figure 2.5c), low energy electrons are turned back first and as all bunch electrons are ultrarelativistic, the higher energy electrons trail behind.

Finally, figure 2.6 compares the spectra of the reflected light in the presence and absence of zeros of the vector potential.

Unfortunately the simulation resolution is too low to resolve the individual harmonics however, the spectrum from the circularly polarised light is typically over two orders of magnitude below that for linearly polarised light. Thus, all defining characteristics of the ZVP mechanism have been identified in 3D simulations with

the notable exception of the energy scalings. Next generation supercomputers will be required to perform such parameter scans.

2.4 The ZVP electron bunch

Following the success in reproducing the key features of the ZVP mechanism and demonstrated consistency between 2 and 3D equivalent simulations, the remainder of this chapter will predominantly utilise 2D simulations to interrogate the interaction further. Previous work on the ZVP mechanism has highlighted the high energy and short duration of electron bunches, now full characterisation of such bunches is performed. A ZVP electron bunch is an electron bunch produced via the ZVP mechanism. Once produced and accelerated across the pseudocapacitor field, it is launched back in the laser propagation direction. While the bunch has no spatial separation over energies when propagating with the zero of the vector potential, the turning point of the electrons is longitudinal momentum dependent due to the Coulomb attraction of the ions after overshooting the pseudocapacitor field. Baeva *et al* showed that the electron bunch has a quasi-monoenergetic spectrum: there is a one-to-one relationship between energy and position with the higher energies trailing the lower energies. The full bunch is confined to 130 as while a single energy confined to 5 as. If, however, the plasma bulk is transversely mass-limited relative to the laser spot size, when rotated back towards the plasma block, some of the electron bunch will overshoot and escape the potential well without significant stretching of the bunch in time as can be seen in figure 2.3. Such electron bunches retain their high charge density and ultra-short duration. ZVP electron bunches can therefore be placed into two categories: ultra-high charge, ultra-short duration electron bunches from mass-limited targets, hereafter labelled mass-limited electron bunches, of interest due to their unique properties, and bulk propagating bunches, hereafter labelled bulk bunches, which have lower charge densities, are imprinted with instabilities and are instead of interest due to their connection to energy absorption and reflection in this post-ponderomotive

regime. To investigate these two bunch types further, 2D PIC simulations were performed, see appendix for parameters.

Attosecond nano-Coulomb mass-limited electron bunches

Figure 2.7 describes a typical mass-limited ZVP electron bunch qualitatively. The electron bunch under interrogation is ultra-relativistic with a mean energy of 51(11) MeV and a duration of 35 as. It propagates at an angle of -393 rad relative to the laser propagation direction, *i.e.* the x -axis, and has a transverse geometric emittance in the simulation plane (the x - y plane) of 35(7) nm rad. The calculation of the transverse geometric emittance, a measure of the quality of the electron beam, is given in appendix A.3. Note that while the bunch does not propagate in the laser propagation direction, this does not mean it must be rejected under consideration of the ZVP bunch conditions. Indeed, the bunch must propagate at some angle to the laser due to conservation of canonical momentum while it remains in thrall of the laser pulse. For an equivalent bunch in a corresponding 3D simulation, the transverse geometric emittance in the z plane is 15(11) nm rad. This electron bunch has a total charge of 0.35 nC for a slab of plasma of thickness 0.75λ in the z -direction. Noting again the two-dimensional nature of the interaction geometry, and that electrons less than twice the relativistic Larmor radius,

$$r_L = \frac{\gamma m_e v}{e|\mathbf{B}|}, \quad (2.45)$$

where γ and v correspond to the electron velocity, when rotated back towards the plasma will escape to the side, the total number of electrons in the mass-limited bunch is

$$N = 2n_e r_L L_z \Delta x, \quad (2.46)$$

where L_z is the width of the plasma in the z -direction. Using equation 2.23 for Δx and 2.26 for γ and approximating $v \approx c$ for the ultra-relativistic electron bunch,

$$N = 2\gamma n_c \frac{L_z}{k^2}. \quad (2.47)$$

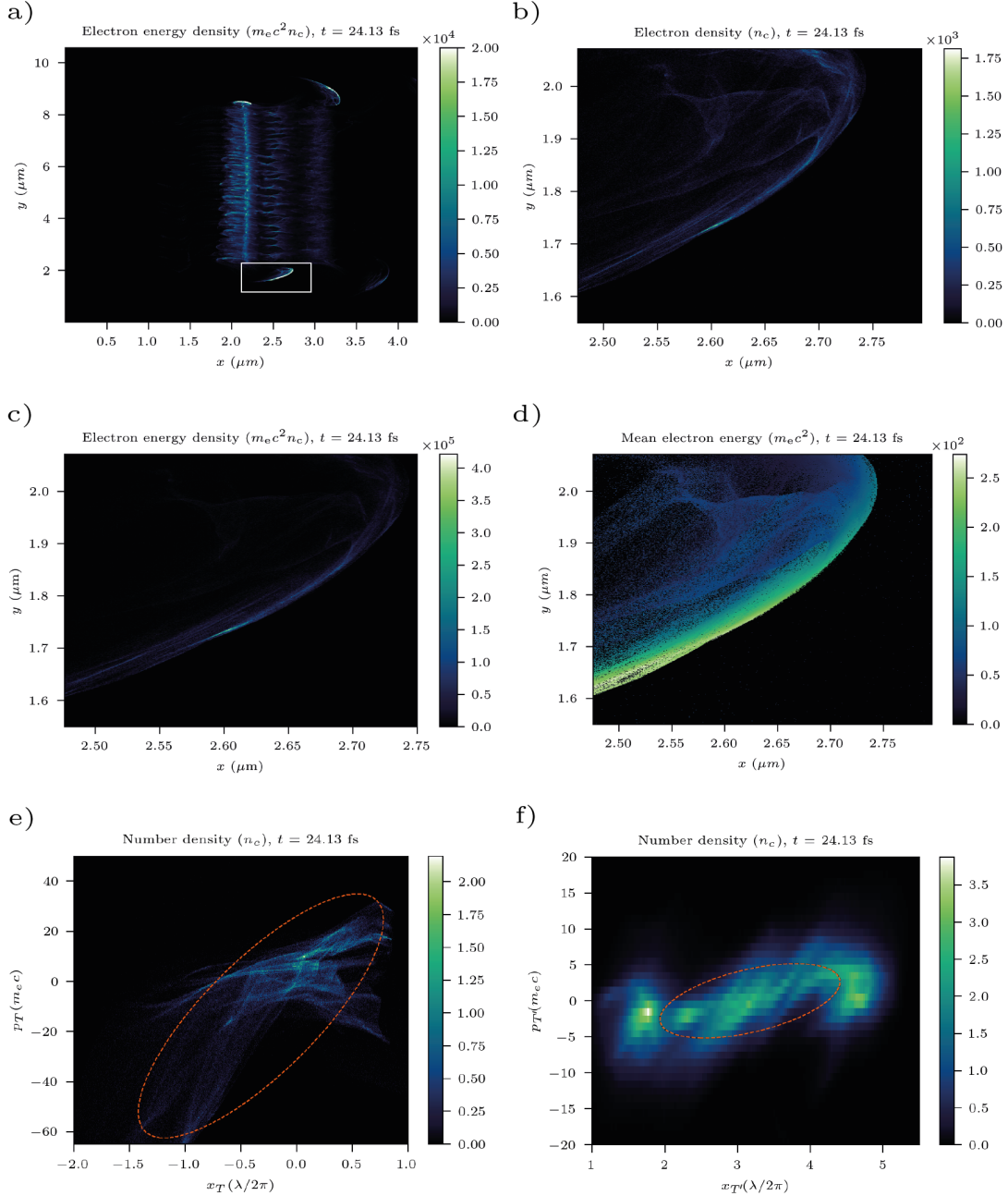


Figure 2.7: 2D PIC simulation results qualitatively describing typical mass-limited ZVP electron bunch structure. a) Electron energy density for the full simulation window, corresponds to figure 2.3f). The box highlights the bunch presented in the following plots. b) Electron number density of the electron bunch. c) Electron energy density of the electron bunch, the colourbar scale has been increased compared to figure a) to demonstrate the internal structure. d) The mean electron energy across the electron bunch, suggesting a position dependent energy or quasi-monoenergetic nature to the electron bunch [121]. Cells with no macroparticles are black. e) The transverse phase space in the 2D simulation plane. The ellipse describes the calculated emittance. The skew of the ellipse is a consequence of a low density tail on the phase space beyond the bottom left corner. f) This plot was extracted from the equivalent 3D simulation and describes the transverse emittance in the z -direction. Again the ellipse marks the emittance. The relatively well-defined border to the phase space and the mild tilt (indicating only mild divergence) are direct consequences of the 2D nature of the interaction.

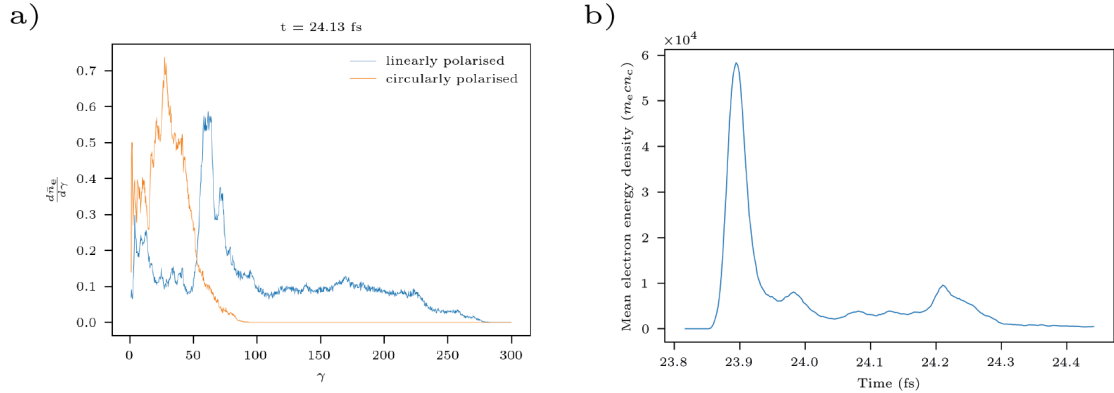


Figure 2.8: a) Energy spectra for mass-limited electron bunches formed via linearly and circularly polarised laser pulses. b) Mean energy density streaked in time through the centre of a mass-limited ZVP electron bunch demonstrating the attosecond duration.

For these simulation parameters, this corresponds to a total bunch charge, $Q = eN$, of 0.37 nC, a remarkably successful prediction of the ZVP model. Equation 2.47 tells us there is no limit to the

Equation 2.47 can be rewritten in terms of fundamental constants as

$$N = 2(1 + 0.5 \frac{a_0^2}{n_e}) L_z \frac{m_e \epsilon_0 c^2}{e^2}. \quad (2.48)$$

Counter-intuitively, it would appear the total charge scales inversely with the plasma density. Instead, charge can be increased either by increasing the laser pulse intensity or L_z . Indeed, provided the laser pulse intensity remains relativistic, the focal spot can be increased indefinitely and there is no limit to the mass-limited electron bunch total charge. For a realistic laser pulse with beam width 10λ incident on a larger laser block, equation 2.48 predicts a charge of 9.3 nC.

Figure 2.8a compares the electron bunch energy to an equivalent bunch produced by a circularly polarised laser pulse². The mean electron bunch energy is over three times lower as there is no ZVP acceleration phase and there is no quasi-monochromatic structure [121]. Figure 2.8b demonstrates the attosecond duration of the electron bunch.

²A circularly polarised laser pulse will expel electrons from a mass-limited target in a corkscrew shape, the bunch is therefore only loosely equivalent.

Applications: from electron bunches to attosecond light

There are a plethora of applications for high charge, attosecond electron bunches, primarily enabling the resolution of attosecond scale phenomena [128]. Already femtosecond pump, attosecond probe experiments are underway [129, 130] but the higher intensities and charge densities accessible in the laser-solid regime compared to laser-gas interactions [112, 125] would dramatically advance the field by enabling atto-pump atto-probe experiments [108]. Potential applications include: electron microscopy and atomic diffraction to temporally resolve photoelectric processes such as Bragg diffraction [131], ultra-fast electron radiography to probe the evolution of the formation of magnetic fields in dynamical systems [132] or for XFEL seeding [113]: the record XFEL X-ray pulse duration stands at 280 attoseconds [133], substantially longer than the durations accessible using this technique. Electron bunches are also a promising alternative for radiotherapy due to their superior penetration depth in biotissues compared to X-rays [134].

Analogously to the HHG process, rapid acceleration of an electron bunch generates a burst of radiation whose properties (brightness, coherency, duration, spectrum) are determined by the corresponding properties of the electron bunch (charge, emittance, duration and energy). Thus globally electron bunches are used as a diagnostic tool in synchrotrons and XFELs. Other acceleration mechanisms for X-ray generation include: bremmstrahlung radiation from firing the electron bunch at a secondary high- Z target [135], interaction with a counter-propagating laser pulse [136, 137] or injection into a laser or plasma wakefield accelerator **CITE**, including accessing the solid density plasma wakefield regime [112]. The mass-limited electron bunches produced via the ZVP mechanism have transverse emittances comparable in all planes to those conditioned in state-of-the-art nano-Coulomb electron bunch accelerators [138, 139]. Such facilities typically produce electron bunches with geometric emittances of \sim mm rad prior to damping ring injection [140] and \sim nm rad post-injection [138]. Thus, the mass-limited ZVP electron bunches are ideal candidates for the production of bright X-rays of unprecedentedly

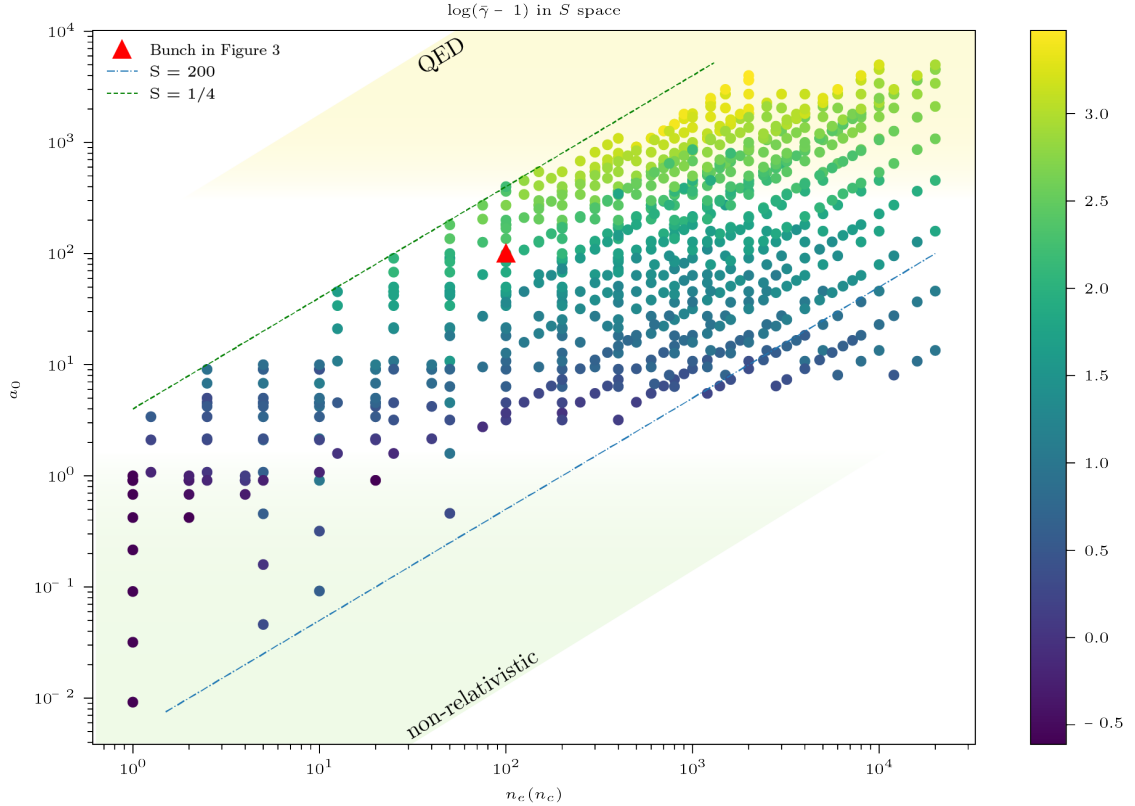


Figure 2.9: Mean mass-limited ZVP electron bunch normalised kinetic energies extracted from 2D PIC simulations. The bunch detailed in figure 2.7 is highlighted.

short duration and are suitable for the study of the new regime of attosecond science with applications to physical, chemical and biological systems.

Parameter scan of electron bunch mean energy

Since ZVP energy scaling is a fundamental identifier of ZVP bunches, it is important to confirm that mass-limited electron bunches follow the same scaling relations as has previously been confirmed for bulk ZVP electrons in both 1D [121] and 2D [120] PIC simulations. The mean mass-limited electron bunch kinetic energies were extracted from 120 2D PIC simulations and are plotted in figure 2.9. Particle merging was turned on for macro-photons and macro-electrons for $a_0 \geq 1800$ to prevent overloading of the available supercomputer memory due to the vast number of particles produced in this SF-QED regime. The dependence on both a_0 and n_e demonstrates these electron bunches are accelerated by a non-ponderomotive mechanism. The parameter scan took plasma block densities ranging from the

critical plasma density to well-beyond solid density for the aluminium target and with laser pulse peak intensities ranging from non-relativistic ($a_0 < 1$) through to the Quantum Electro-Dynamics (QED) plasma regime ($a_0 > 300$) up to a peak $a_0 = 5000$ to investigate the change in scaling observed by Savin *et al* [141] at the onset of QED effects. This study is also the first to extract specific bunch energies as opposed to total simulation box energy gain, representing a far more focused test of ZVP theory.

Care must be taken however as the energy of such electron bunches cannot be directly compared to the ZVP energy relations as as aforementioned, after escaping the potential, the electron bunch experiences further direct laser acceleration before reaching the detection point. Indeed, Thévenet *et al* [114] suggested that attosecond electron bunches produced in reflection exhibit precisely the phase and energy properties required to ‘surf’ the reflected laser pulse and experience vast acceleration gradients over the Rayleigh length of the laser pulse. This process is known as Vacuum Laser Acceleration. It seems highly likely that this process occurs for electron bunches produced in transmission. This seemingly unfortunately situation in reality provide a fully optical scheme to create GeV nano-Coulomb electron bunches from the most basic of setups: a laser and a solid density target.

Returning to the determination of the electron bunch energy at the measurement point, consider now the journey of the electron bunch after expulsion from the plasma bulk. It is rotated back towards the plasma bulk by the magnetic field of the subsequent peak of the laser pulse, then travelling at approximately c it surfs the peak, experiencing an approximately constant accelerating electric field from the laser pulse at some fraction f of the laser field peak. The work done by this field is then

$$\Delta T = \int e\mathbf{E} \cdot d\mathbf{x}. \quad (2.49)$$

Note that for this process, the laser pulse electric field and electron bunch direction of travel will always be aligned no matter to which side of the plasma bulk the

electrons are accelerated to and therefore ΔT will always increase the energy of the electron bunch, thus,

$$\Delta T = efE_L\Delta y, \quad (2.50)$$

where Δy is the distance along y from the plasma edge to the detection point. Accounting for the Gaussian spatial profile of the laser, $a(t) = a_0 \exp(-y^2/(6\lambda)^2)$ at focus, the gamma factor after both acceleration phases for this simulation setup is then

$$\gamma = 1 + (0.30) \times \frac{a_0^2}{\bar{n}_e} + (1.2f) \times a'_0. \quad (2.51)$$

Here the primed vector potential refers to the intensity of the subsequent peak of the laser pulse. This final term could be neglected or at least reduced somewhat once super-Gaussian spatial laser pulses become standard in this intensity regime or by using a suitable plasma separator [142], as applied in [143]. Both acceleration phases fail to meet the criteria of the Lawson-Woodward theorem. The ZVP phase is dependent on the existence of electrostatic forces, while the secondary phase occurs for a finite interaction region.

Fitting equation 2.51 to the PIC simulation data presented in figure 2.9 finds

$$\gamma = 1 + (0.46 \pm 0.02) \times \frac{a_0^2}{\bar{n}_e} + (0.28 \pm 0.01) \times a'_0 \quad (2.52)$$

with an r^2 -value of 0.818. This fit suggests $f = 0.22 \pm 0.01$. The electric field experienced for a random selection of electrons in a bunch was extracted from one simulation. Encouragingly, the mean attenuation of the electric field they experience is 0.20 ± 0.05 , to calculate this attenuation directly falls beyond the scope of ZVP theory.

This is the first demonstration of ZVP theory to calculate absolute values and not only the scaling relationship. Such order of magnitude calculation is essential to compare this model of absorption to others and thus determine the dominant mode for absorption. It is certainly remarkable that such a simple theory for energy absorption has such predictive success in this highly non-linear and seemingly chaotic many particle system. It is interesting that increasing laser intensity to

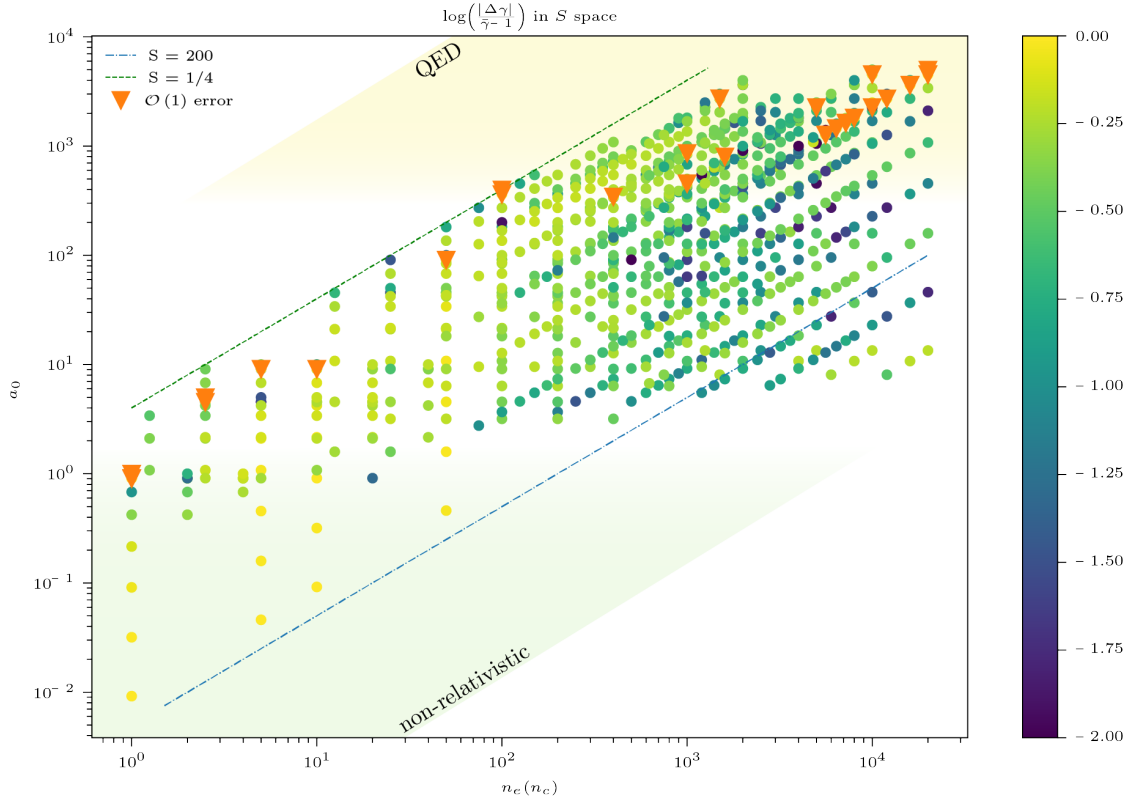


Figure 2.10: The relative errors for each mean energy data point compared to figure 2.9. The orange triangles indicate data points for which the model fails to predict the mean energy.

such extremes will, at least for a short time, cause relativistic effects that simplify the dynamics before the total annihilation of a target.

The relative error between data and theory is plotted in figure 2.10. Those points marked by an orange triangle have associated errors of over an order of magnitude. Reassuringly, such points occur only after the onset of QED effects, known to impact the ZVP mechanism [141] and for $S < 1$, that is, where the plasma becomes relativistically transparent to the laser pulse, a fundamentally different regime. Equally, for non-relativistic laser intensities, where assumptions of electron coherency cannot be made, are poorly fit by the model. It is particularly interesting that there is no indication that large S causes a breakdown of the model, extending the applicability of the model further than previously considered and opening up the field to a wider range of conditions, such as that of shock compressed plasmas. To summarise, it would appear the ZVP model is valid for $10 \leq a_0 \leq 300$ and $S \geq 1$.

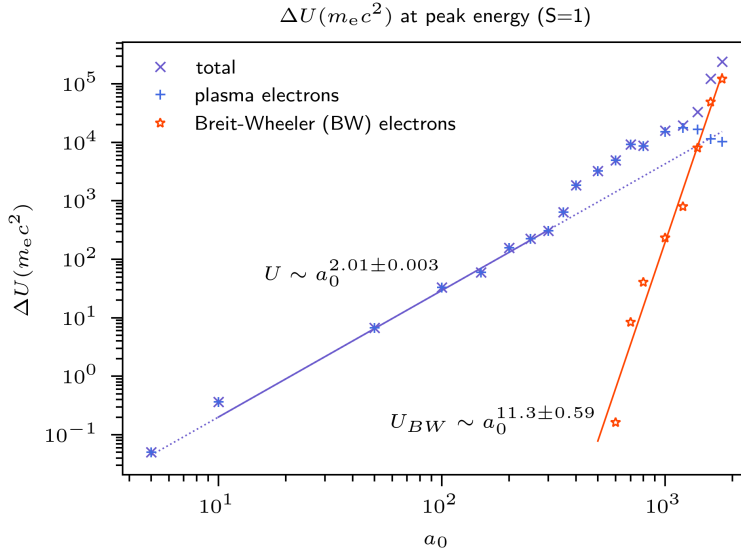


Figure 2.11: Peak instantaneous bulk electron bunch total energy escaping to the plasma bulk rear.

2.4.1 Energy absorption in the ZVP regime

As stated previously the laser-plasma coupling exists in a state of adiabaticity with the exception of the ZVP acceleration phase and hence equation 2.28 describes the absorption of laser pulse energy. For normal incidence, the rate of energy transfer is therefore

$$R = \frac{U\omega_L}{\pi}, \quad (2.53)$$

since two bunches are produced per laser cycle. To demonstrate the scaling for U in 2D PIC simulations, peak instantaneous electron bunch energies escaping to the rear of the bulk were extracted from those PIC simulations with $S = 1$. For constant S ,

$$U \sim a_0^2. \quad (2.54)$$

Energies are plotted in figure 2.11. Fitting the total energy within the range of validity established for the ZVP model finds

$$U \sim a_0^{2.01 \pm 0.003}, \quad (2.55)$$

reproducing with great success the anticipated scaling within the ZVP regime. It is also quite satisfying that the number of electrons and bunch mean energies

both follow their anticipated ZVP scalings, further evidence this is not a simple ponderomotive effect. By extracting specific bunch total energies, rather than just the peak energies of the plasma block as a whole as was performed in previous studies, this is a far more direct confirmation of energy absorption by the ZVP mechanism into electron bunches. This is highlighted by the difference in results obtained for this study compared to a previous study by Savin *et al* [141] when investigating the QED regime as will be discussed later. It was not possible to reproduce the constants of equation 2.28 as the neutralising return current in the plasma bulk generates an electrostatic field on the rear side of the plasma block, decelerating bulk electron bunches as they escape the plasma. It should be possible to calculate the deceleration by considering the number of electrons expelled by the plasma. It is, however, clear from the simulations that at least some electrons in the escaping bunch are trapped by this rear-side potential well reducing its magnitude.

While equation 2.28 describes energy absorption into hot electron bunches, the coupling of such hot collisionless electrons to the bulk plasma given the lack of collisionality is naturally indirect. There are two key mechanisms [144]. Firstly, via a cooler resistive return current of electrons that neutralises the current of the injected hot electrons that escape the potential well of the front surface (**cite this, the reference in sherlock 2014 is not great**). Since all hot electrons travel at approximately speed c , the magnitude of the return current depends not on the total energy absorbed but instead on the total number of electrons injected, as given by equation 2.27, depending linearly on laser spot area and the electric field magnitude and not on the plasma density³. Secondly, via the formation of large amplitude bulk plasma waves induced in the wake of the hot electron bunches. Sherlock *et al* [144] calculate the magnitude of the induced wakefield to be

$$E_W = \frac{eN_e c}{\omega_p \epsilon_0} = \sigma \sqrt{\frac{m_e \epsilon_0}{n_e}} E_L, \quad (2.56)$$

³Note that for a sufficiently thin target, the return current induces an electrostatic field on the back surface of the target which can then reflect hot electron bunches and decelerate them to the point of a return to collisionality. This is a reality for the PIC simulations explored in this thesis, however, since realistic targets are much thicker this shall be neglected.

where here the bunch velocity has been set to c , bulk electrons will be accelerated by E_W and their kinetic energy converted to heat via collisions. Interestingly, this reproduces the mid temperature electron scaling with density that was observed by Chrisman *et al* [145] in their study of hot electron energy coupling in cone-guided fast ignition of inertial fusion targets. This is a different possible explanation to their self-declared ‘hand waving argument’. Excluding this study, such formulations for heat transfer to the plasma bulk within the ZVP regime remain untested in simulations.

Note also that as the laser pulse intensity rises, the fraction of energy absorbed by the ion species increases. Savin [122] determined for $S = 1/2$, $a_0 = 100$, that this would be almost 20%. Energy is absorbed by ions via the hole boring mechanism as described elsewhere in this thesis.

2.4.2 Unpacking the QED effects of figure 2.11

In Savin’s acclaimed paper [141], they determined theoretically and demonstrated in simulation that at $a_0 = 300$, $n_e = 50n_c$, there is a transition from standard ZVP scalings to an enhanced QED scaling associated with Breit-Wheeler (BW) electrons increasing the pseudocapacitor plate charge. Explicitely,

$$T \sim \frac{a_0^5}{\bar{n}_e}. \quad (2.57)$$

Such a scaling shift was not observed for the large parameter scan presented in figure 2.9. Simulations revealed this was likely due to only few BW pairs being produced towards the plasma edges and hence no additional gain in energy from crossing the pseudocapacitor at those points. Another concern is Savin’s study was conducted within the regime of relativistic transparency where it is unclear whether the ZVP potential well can be maintained and was not explored in this study. The final consideration is the well known effect of radiation trapping due to RR [146], also observed in these PIC simulations. After acceleration across the pseudocapacitor, the electron bunch encounters the subsequent laser peak. If the electron bunch gamma factor and laser intensity are both large enough, electrons radiate a significant fraction of their energy and are thus stopped in

their tracks. Unable now escape the potential well at the plasma surface they are trapped and are not observed to escape the plasma until the laser pulse intensity reduces. Such an effect would not impact Savin's scalings but would of course inhibit the observation of the scaling for electrons escaping to the sides and rear of the plasma block. Note that should this be the case and the collisionless electron bunches remain within the plasma bulk, Savin's ZVP QED model truly applies directly to energy absorption by the plasma bulk.

Returning now to figure 2.11, there are two interesting aspects. Firstly the sudden jump in total energy at $a_0 \approx 300$. This cannot be explained by ZVP theory nor QED theory since the jump is observed with QED effects switched off. Secondly, the even sharper jump in total electron bunch energy above $a_0 = 1000$. Decomposing the total energy into bulk electrons (here referring to electrons from the plasma bulk that undergo ZVP) and those produced via the BW process, this is clearly a QED effect. Energy in BW produced electrons scales at a staggering

$$U_{\text{BW}} \sim a_0^{11.3 \pm 0.8}, \quad (2.58)$$

while the energy of bulk plasma electrons decreases. Perhaps this is a signal of Savin's QED ZVP electron bunches only at a higher energy due to the substantially greater plasma density of these simulations. The reduction in bulk electron energy can be attributed to an oversaturation of the front surface with BW electrons.

Combining equations 1.54 and 2.28 and assuming the electron radiates all its energy to the photon, for the ZVP mechanism, at the point of emission one finds

$$\chi_\gamma = \frac{\sqrt{2}|\mathbf{E}|}{E_S} \frac{a_0^2}{\bar{n}_e}. \quad (2.59)$$

The probability of BW pair production begins to rapidly increase around $\chi = 1$, therefore, the transition to QED will occur at

$$a_0 \approx \left(\frac{E_S}{\sqrt{2}} \frac{e\bar{n}_e}{m_e c \omega_L} \right)^{1/3} = \left(\frac{a_s \bar{n}_e}{\sqrt{2}} \right)^{1/3}, \quad (2.60)$$

where $a_s = 7.73 \times 10^5$ is the normalised vector potential associated with the Schwinger Field, thus explaining the transition to QED at higher intensities in this

work compared to Savin's. Following Savin's theory, one expects

$$U_{\text{QED}} \sim \frac{a_0^7}{S}, \quad (2.61)$$

therefore much work is required to understand and unify these results, starting with the application of the methods of this analysis to the parameter space explored by Savin. Undoubtedly, the advent of next generation exa-watt scale lasers and access to this regime will be exceedingly interesting if such scalings in bunch energy can be maintained.

Linear Breit-Wheeler can safely be neglected, there is simply not enough energy in the system. For two interacting photons of energy E_1, E_2 , by consideration of four-momenta, the threshold condition for pair production is

$$E_1 E_2 \geq (m_e c^2)^2. \quad (2.62)$$

For a near-infrared laser photon of energy $\hbar\omega_L$, the interacting photon must have an energy in excess of 200 GeV. Despite the extreme acceleration gradients considered in this thesis, the ZVP mechanism predicts photons of energies no greater than 10 GeV and thus linear Breit-Wheeler is suppressed.

He *et al* [147] identified an alternative mechanism for linear BW using solid density targets, where forwards- and back-scattered high energy radiation reaction produced photons interact within a hollowed out plasma channel. In the geometry of interest in this thesis, while photons are produced in both directions, their production is localised to the plasma surface and at no points do their paths cross and thus this mechanism does not occur.

2.4.3 Errors

To get some sense of the stability of the parameter scan, new simulations with tweaked parameters were created to explore the effects of including collisions, increasing the temperature to resolve the Debye length and particle merging. The results are presented in figure 2.12. In general including collisions had little to no effect on the results and changing the Debye length had a small but not

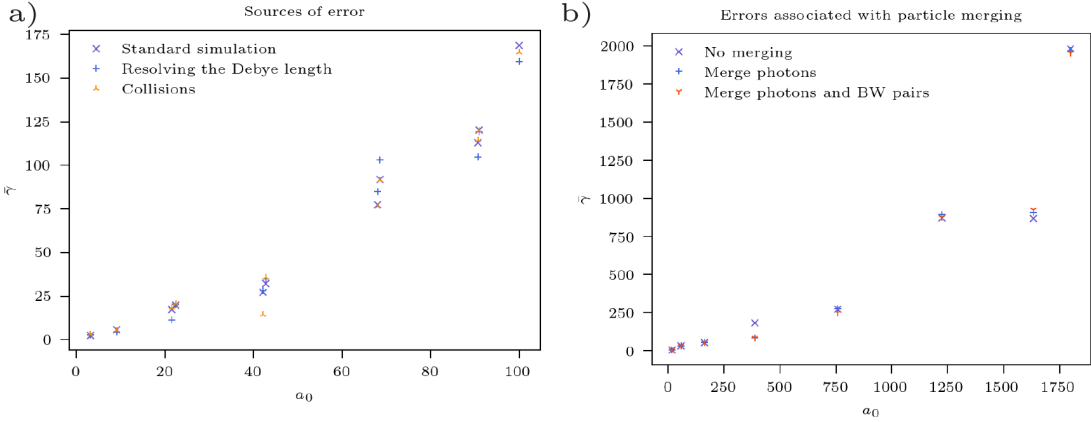


Figure 2.12: An exploration of ZVP 2D PIC simulation stability. a) Electron bunch mean energies extracted from simulations with a_0 , $\bar{n}_e = 100$. Here, the x -axis is the normalised vector potential of the laser pulse cycle that made them, this is why there appears to be results stacked. b) Electron bunch mean energies extracted from simulations with a_0 , $\bar{n}_e = 1800$ both with and without particle merging.

systematic effect on the results. Note that while numerical heating is not directly dependent on laser intensity, increases to a_0 would increase the electron bunch density. Thus, resolving the Debye length of the ultra-high density (orders of magnitude greater than solid density) electron bunches produced by the higher laser pulse intensities considered here is a non-trivial but potentially interesting exercise. Particle merging was essential for simulations with $a_0 > 1800$. At least at $a_0 = 1800$ it would appear particle merging had negligible impact, however it is likely the error would increase with a_0 .

2.5 Planned future work

Nothing is true unless it is measured and by now the reader should have a healthy level of skepticism for state-of-the-art PIC codes and their inherent proliferation of uncertainty. After a successful proposal application, four weeks of beam time have been awarded on the GEMINI-PW laser facility at the Central Laser Facility (CLF) [148]. Next July, the study of mass-limited ZVP electron bunches will be put to the test as part of a three-pronged experimental campaign, the main experimental goals are

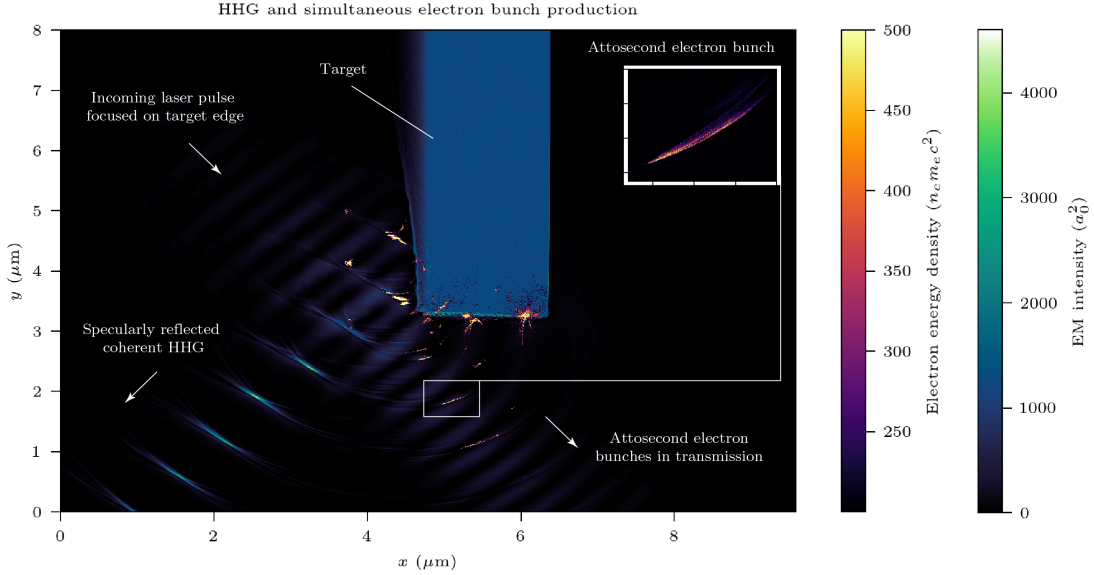


Figure 2.13: A simulation of the planned GEMINI-PW experimental setup for the measurement of ZVP electron bunches. This novel setup enables the simultaneous measurement of attosecond ZVP electron bunches and their coherent emission of X-ray light. The GEMINI-PW laser pulse is incident at 45° on the low density polyethylene target with a preplasma scale length of $0.2\lambda_L$. For this angle of incidence, transmitted bunches and specularly reflected X-ray harmonics are produced at a frequency of ω_L .

1. to characterise the X-ray HHG emission from the reflection of a relativistic laser of a solid target, following on from a recent experiment at the ORION laser facility at AWE [16], which is discussed in great detail in the following chapter;
2. to simultaneously measure and correlate HHG and the ZVP electron bunches responsible for the HHG using a novel experimental setup;
3. to apply the attosecond X-ray HHG beam as a diagnostic tool in a proof of principle warm dense matter experiment.

Preparations are now underway. The requirements for this experiment are simple: a relativistically intense high contrast laser pulse ($a_0 \geq 10$) of a few femtoseconds duration incident on a solid target with surface perturbations small compared to the wavelength of the laser pulse. A simulation describing the experimental setup for the ZVP bunch measurement is given in figure 2.13. By focusing the laser onto the edge of a transversely mass-limited target, the emitted electron bunch energies

will be maximised. Simulations suggest it should be possible to simultaneously measure the specularly reflected HHG and the attosecond ZVP electron bunches that produce it. Directly linking the bunch qualities to the properties of the HHG.

Remaining actions include the performance of PIC code simulation parameter scans in the new geometry. While normal incidence was most convenient for these initial simulations, oblique incidence is more optimal for HHG [115, 125] and as can be understood from equations 2.43 and 2.44, the new energy scaling expressions for the ZVP mechanism at oblique incidence. Not only is oblique preferable but it is essential to mitigate damage to the laser optics via back-reflection. The HHG beam intensity at focus can be over 1000 times that of the incident laser pulse [149]. It is necessary, therefore, to test the new predictions for oblique incidence energy scalings and total electron bunch charge as well as the angle of bunch ejection, the non-zero transverse vector potential of the laser will prevent the bunch from propagating directly along the transmission axis. It would also be useful to perform a parameter scan of preplasma scale length. In this work so far, it was assumed that the optima for electron bunch production are simply those for HHG given the intrinsic link between the two. **CITE THESE.**

GEMINI-PW laser facility

The GEMINI-PW laser facility housed at the CLF is a petawatt class facility consisting of two 30 fs beams each delivering a maximum focused intensity of $2 \times 10^{21} \text{ W cm}^{-2}$ at a repetition rate of 0.05 Hz. Such high frequency of operation has led to a paradigm shift in high power laser physics experimentation with the arrival of statistically significant results.

Targets

A range of thick, flat solid targets are proposed to probe the density parameter space: diamond, a selection of plastics (polymethyl methacrylate, low and high density polyethylene and polycarbonate) and mirrored targets, which produced interesting and slightly unexpected results in the ORION experiment. It would also be interesting to produce foam targets gaining access the optimal low S regime

[150]. Target wheels will be used to take full advantage of the high shot rate of the GEMINI-PW laser. It is anticipated that due to focal spot jitter, not all shots will hit the target edges.

Diagnostics

The electron bunches will be measured using an electron spectrometer placed a few centimetres from the target to measure the time-integrated energy spectrum. The spectrometer will be shielded from the laser pulse and any HHG in transmission using a flash coated kapton foil which should not significantly hinder the MeV electron bunches produced in the interaction. Mordovanakis *et al* used Image Plate stacks to obtain the electron bunch structure and emission angle, it may be necessary to perform this first to accurately position the spectrometer. While resolving attosecond durations remains an outstanding challenge of experimental science, it may be possible to measure the total duration of the train of attosecond electron bunches by measuring the characteristics of coherent optical transition radiation produced by the electrons upon incidence on a secondary target [112]. The X-ray HHG emission will be measured using the OHREX spectrometer [151] on loan from ORION, a spherically bent crystal spectrometer with ultra-high resolution and high-signal-to-noise ratio. Lower order harmonics will be measured using angularly resolved EUV spectrometers. Note that in the absence of attosecond resolution diagnostics, measuring the harmonic spectrum of the coherent HHG is the only way to reconstruct the temporal shape of the pulse. Simulations have suggested that the reflected spectrum produced by Coherent Synchrotron Emission of the electron bunches is approximately Fourier-limited [119]. Off-axis spectrometers should be used to compare the signals to the background emission and to measure the plasma temperature [152]. A quarter wave plate could be used to convert the incoming laser pulse to a circular polarisation to compare the signals to those detected in the absence of zeros in the vector potential.

Preplasma scale lengths and prepulse control

Observation of the ZVP mechanism requires a sufficiently steep density gradients at the laser-plasma interface. A potential drawback of Chirped Pulse Amplification (CPA) laser systems is the existence of prepulses that heat targets, causing them to expand significantly before arrival of the main pulse. To increase the laser contrast, to the point where there is no preplasma formation, GEMINI-PW utilises a Double Plasma Mirror setup [153]. Each mirror is an anti-reflection coated optic placed in the path of the laser beam, acting as an optical switch. As the laser fluence passes the damage threshold of the optic, plasma forms on the front surface and the mirror starts to reflect. As it has been suggested that there is an optimum scale length for HHG, the second GEMINI-PW beam will be used to generate a controllable prepulse to tailor the plasma surface. Investigation of preplasma generation will occur in parallel to the main experimental goals.

2.6 Conclusions

The Zero Vector Potential mechanism describes the post-ponderomotive rapid absorption of ultra-relativistic laser energy by a solid density overdense, collisionless and fully ionised plasma on the timescales of ion immobility. The defining characteristics of the mechanism have been identified in 3D PIC simulations including the observation of a zero of the vector potential propagating at speed $\approx 1.4c$ through a high density ZVP electron bunch at the front surface of the plasma early in ablative journey of the electron bunch. Simulations have suggested that from currently operating 10 PW short pulse laser facilities and foam targets, the ZVP mechanism can produce a train of attosecond duration, nano-Coulomb electron bunches, each with a transverse emittance of a few nm rad. Such charge and quality is comparable to state-of-the-art electron bunch accelerators but on paradigm shifting timescales. Such timescales being those on which atomic processes occur, these electron bunches could be manipulated to literally ‘shed light’ onto fundamental biological and

chemical processes. Via a massive 2D PIC parameter scan the energies of such mass-limited electron bunches have been compared to those predicted by the ZVP model, identifying a range of validity for the model, specifically $a_0 > 10$, $S > 1$. These simulations were also used to confirm the energy absorption scaling in 2D up to and into the QED regime. Finally, details were provided on the planned GEMINI-PW experiment where ZVP electron bunches and ZVP absorption could be observed for the first time. Taking a slight rollback in laser power, the following chapter will now switch gears from absorption to the reflection of radiation from a solid target in the discussion of a recent experiment at the moderately relativistic ORION laser facility.

3

Miscellaneous notes

Contents

3.1	To do	69
3.2	ORION experiment	71
3.2.1	Frames of reference	71
3.2.2	ORION interaction geometry	75
3.2.3	Condition on validity of hole boring expression	77
3.3	Thinking about the ZVP calculation	78
3.4	Things I may want to include or random notes	79

3.1 To do

1. HYADES simulations
2. Add more citations
3. Similarity theory details in appendix
4. Add details on CPA and OPCPA
5. Simulation algorithms (details in appendix?)
6. Velocity transformations derivation (appendix)
7. Sources of error system

8. Ponderomotive heating mechanisms
9. Fix QED section
10. Particle merging
11. Radiating particles and relativistic larmor radius
12. smieli performance plot
13. A collisionless fully ionised plasma
14. Basic derivation of the Schwinger limit
15. Calculating collision frequency
16. Feynmann diagrams
17. Add some detail of vectorisation

On the ZVP front

1. Fix diagrams
2. Go through discussions
3. Add errors plot
4. Check out new sims
5. Conclusion
6. Shape of transverse momentum (more parabolic compared to linear and explanation of bunch holding together), Sharp front edge then parabolic (or even exponential decay - it is defo exponential)
7. a0 convention, when max and when varying in time
8. Editing

3.2 ORION experiment

The following derivation determines the polarisation of the ORION laser pulses in the experiment and the boosted frame quantities for the PIC simulations.

I will have a whole subsection devoted to the different frames of reference of relevance and then a second one about normalised units. What follows now is the derivation of the boosted frame in which the laser is incident normally relative to the lab frame where the laser is incident obliquely.

I will try to use a consistent convention for coordinate system as much as possible.

3.2.1 Frames of reference

Other frames of reference include, HB front surface at rest frame, ablating front frame, smilei frames.

When writing out the pistonning equation in full in thesis, include analysis in Robinson 2009 to do it for multiple ion species.

I should go over this and use third year relativity notes to formalised and make more consistent.

While some of this section may seem trivial, it is frequently miscalculated in the literature, it therefore seems of great importance to provide a full derivation.

The following is inspired by [154], here they give the formula for k and ω .

In [155] they determine the normalised vector potential, if defined similarly in the new frame, then it is frame invariant. This fails to consider what about the fact that the vector potential is in reality more complex and is not simply the temporal integral of the electric field. Nonetheless it is still reasonable to define it so if what is of real importance (as is usually important) is in fact the fields and it is simply being used as a way to normalise the field intensity.

Consider a photon incident on a plasma block at angle θ as in figure 3.1. A boost is applied with velocity \mathbf{v} to a frame such that the photon is normally incident on the now streaming plasma at velocity $-\mathbf{v}$. The velocity transformation for the

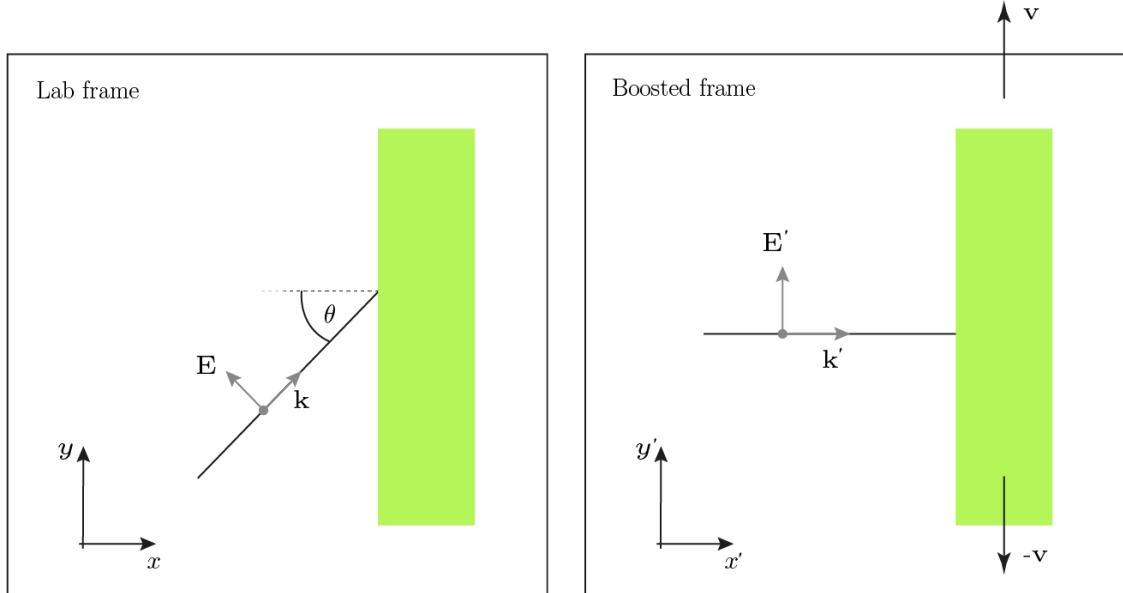


Figure 3.1

photon's velocity, \mathbf{u} , parallel to the boost is

$$\mathbf{u}'_{\parallel} = \frac{\mathbf{u}_{\parallel} - \mathbf{v}}{1 - \mathbf{u} \cdot \mathbf{v}/c^2}. \quad (3.1)$$

Setting $\mathbf{u}'_{\parallel} = 0$, it is clear that

$$\mathbf{v} = \mathbf{u}_{\parallel} = c \sin \theta \hat{\mathbf{y}} \quad (3.2)$$

in this geometry and

$$\gamma_{\mathbf{v}} = \frac{1}{\sqrt{1 - \mathbf{v}^2/c^2}} = \sec \theta. \quad (3.3)$$

Noting that since Snell's law is frame invariant, the photon remains normal as it propagates into the skin depth of the plasma, a frame in which the interaction reduces to a 1D problem has been successfully found for all $\theta < \pi/2$. Those familiar with the topic may wonder how this is possible considering the ‘ripples’ that are observed on the plasma surface for oblique incidence. The explanation for this is of course the relativity of simultaneity. It remains to determine how do all the relevant quantities transform as such a boost is applied. Starting with an easy one: the photon's wave four-vector is

$$\mathbf{K}^{\mu} = \left(\frac{\omega}{c}, \mathbf{k} \right) \quad (3.4)$$

and thus the frequency transforms as

$$\frac{\omega}{c} = \gamma_v \left(\frac{\omega'}{c} - \frac{\mathbf{v} \cdot \mathbf{k}'}{c} \right). \quad (3.5)$$

Since $\mathbf{v} \cdot \mathbf{k}' = 0$,

$$\omega' = \omega \cos \theta. \quad (3.6)$$

As

$$n'_c = \frac{m_e(\omega')^2}{4\pi e^2}, \quad (3.7)$$

$$n'_c = n_c \cos^2 \theta, \quad (3.8)$$

while the plasma block will be Lorentz contracted along $\hat{\mathbf{y}}$, hence the number density of electrons will increase as,

$$n'_e = \frac{n'_e}{\cos \theta}, \quad (3.9)$$

leading to the perhaps unexpected

$$\bar{n}'_e = \frac{\bar{n}_e}{\cos^3 \theta}. \quad (3.10)$$

Time is dilated

$$t' = \frac{t}{\cos \theta}. \quad (3.11)$$

Consider now the more general case (I should just simply replace my diagram with a 3D one that incorporates this initially) where the photon's electric field is rotated out of the x - y plane, *i.e.*

$$\mathbf{E} = E_0(-\cos \phi \sin \theta, \cos \phi \cos \theta, \sin \phi) \quad (3.12)$$

and correspondingly

$$\mathbf{B} = \frac{\hat{\mathbf{k}} \times \mathbf{E}}{c} = \frac{E_0}{c}(\sin \phi \sin \theta, -\sin \phi \cos \theta, \cos \phi). \quad (3.13)$$

The Lorentz transformations for electro-magnetic fields are

$$\mathbf{E}'_{||} = \mathbf{E}_{||}, \quad (3.14)$$

$$\mathbf{B}'_{\parallel} = \mathbf{B}_{\parallel}, \quad (3.15)$$

$$\mathbf{E}'_{\perp} = \gamma_{\mathbf{v}}(\mathbf{E}_{\perp} + \mathbf{v} \times \mathbf{B}), \quad (3.16)$$

$$\mathbf{B}'_{\perp} = \gamma_{\mathbf{v}}(\mathbf{B}_{\perp} - \mathbf{v} \times \mathbf{E}/c^2). \quad (3.17)$$

Using the above expressions for \mathbf{E}_{\perp} and \mathbf{E}_{\parallel} and transforming to the boosted frame,

$$\mathbf{E}' = E_0 \cos \theta (0, \cos \phi, \sin \phi). \quad (3.18)$$

As anticipated for normal incidence there is no component of the E-field normal to the surface. Conveniently, the polarisation of the incident photon is unchanged despite having components both parallel and perpendicular to the transformation and

$$|\mathbf{E}'| = |\mathbf{E}| \cos \theta. \quad (3.19)$$

The picture can now be completed. Since

$$a'_0 = \frac{e|\mathbf{E}'|}{m_e e \omega'} \quad (3.20)$$

it follows that

$$a'_0 = a_0, \quad (3.21)$$

$$S' = \frac{S}{\cos^3 \theta}. \quad (3.22)$$

Four-potential transformation

Consider a laser pulse obliquely incident, angle θ , it has 4-vector potential $\mathbf{A}^{\mu} = (0, A \sin \theta, A \cos \theta, 0)$, where $A = A_0 \sin(\mathbf{k} \cdot \mathbf{x} - \omega t)$ and $\mathbf{k} = (k \cos \theta, k \sin \theta, 0)$. Applying the lorentz transformation, in the frame where the laser pulse is normally incident,

$$\mathbf{A}'^{\mu} = (-\gamma \beta A \cos \theta / c, -A \sin \theta, \gamma A \cos \theta, 0) = (-A \sin \theta, -A \sin \theta, A, 0) \quad (3.23)$$

since $\beta = \sin \theta$ in the positive y direction and $\gamma = 1/\cos \theta$.

Therefore,

$$\mathbf{E}' / \cos(\mathbf{k} \cdot \mathbf{x} - \omega t) = -\sin \theta \cos \theta k A_0 \hat{\mathbf{x}} - \sin \theta \cos \theta \omega A_0 \hat{\mathbf{x}} + A_0 \omega \cos \theta = A_0 \omega', \quad (3.24)$$

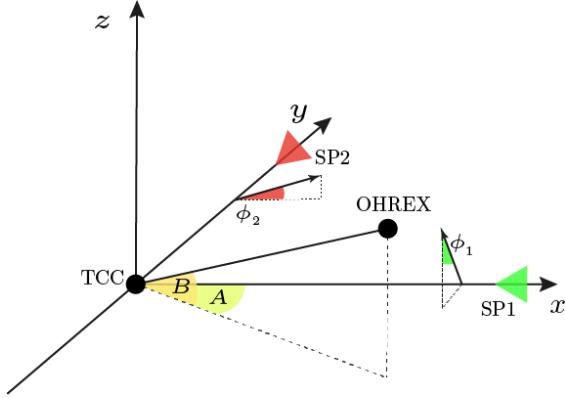


Figure 3.2: ORION target chamber geometry showing the location of the target (TCC) and OHREX spectrometer and the green (SP1) and infra-red (SP2) beamlines and their corresponding polarisations.

since $\sin(\mathbf{k} \cdot \mathbf{x} - \omega t) = \sin(x' k \cos \theta - \omega t' \cos \theta)$ Note I have been sloppy here with factors of c .

Do it does look at though the vector potential amplitude is unchanged by the transformation but it is more subtle, it is useful to define an $a'_0 = eE/m_e\omega$ to normalise the electric field intensity but note that this cannot be converted into the actual vector potential, it is just a useful construct.

Also note that whatever the transverse vector potential is in the boosted normal incidence frame is simply whatever the amplitude of the vector potential is in the oblique incidence frame.

3.2.2 ORION interaction geometry

The ORION target chamber has its own defined geometry with the target located at the origin, described in figure 3.2. The polarisation angles are $\phi_1 = 11.8^\circ$ and $\phi_2 = 16.4^\circ$. Following reflection of the infra-red beam off the plasma mirror, both the green and infra-red lasers propagate in the $-\hat{\mathbf{x}}$ -direction towards the origin. The OHREX crystal is located at

$$\mathbf{r}_{\text{OHREX}} = r_0(\cos B \cos A, -\cos B \sin A, \sin B), \quad (3.25)$$

where $r_0 = 2.4\text{ m}$, $A = 26.82^\circ$ and $B = 18.15^\circ$, setting the rotation angle of the target. This was achieved using the ORION Multi-Target-Mounts. Alignment

was performed by Ed Gumbrell and no further details will be provided here on that process.

The interaction plane is therefore defined by the vector

$$\mathbf{n} = \frac{\mathbf{r}_{\text{OHREX}}}{r_0} \times \hat{\mathbf{x}} = (0, \sin B, \cos B \sin A). \quad (3.26)$$

The cosine rule can be applied to determine the polarisation of the laser pulses in the interaction plane, for polarisation vector $\hat{\mathbf{E}}$,

$$\frac{\mathbf{n}}{|\mathbf{n}|} \cdot \hat{\mathbf{E}} = \cos \theta, \quad (3.27)$$

where θ defines the angle between the polarisation vector and the vector normal to the interaction plane. This corresponds to angles out of the interaction plane of 42.2 or the SP1 beam (rotating anticlockwise out of the interaction plane when looking from TCC to parabola) and 19.6 or the SP2 beam (rotating clockwise out of the interaction plane when looking from TCC to parabola). Again applying the cosine rule, the angle of incidence is 16

Next up: Polarisation on OHREX interaction plane.

The same method can be applied to determine the polarisation of the OHREX crystal interaction plane. The OHREX crystals have a nominal Bragg angle of 51.3

I still need to know the exact orientation of the OHREX but assuming it is vertical, the interaction plane is defined by

$$\mathbf{n}_O = \frac{\mathbf{r}_{\text{OHREX}}}{r_0} \times \hat{\mathbf{z}} = (-\sin A, -\cos A, 0), \quad (3.28)$$

once it has been normalised.

Then again applying the cosine rule, this plane corresponds to angles out of the interaction plane of 10.5° for SP1 and 58.9° for SP2.

It has been assumed that the non-linear RPM mechanism retains the polarisation of the incident laser pulse in the reflected harmonic beam.

Then since the OHREX crystal reflection is a linear process, we can decompose our incident beam into its polarisation constituents and consider what their combined intensity post reflection at the detector plane will be.

Also discuss the fabulous result that generally one can simply extract the results in the Smilei units and multiply by the relevant factors of the frame of interest and thus not worry too much about frame transformations.

Also check the boosted frame results against the bouchard thesis.

Once I have finished this section I must redo boosted section since I have made a mistake there and rethink a bit about optimum theta.

I must also at some point just state that a hat indicates a normalised vector.

3.2.3 Condition on validity of hole boring expression

Robinson *et al* [156] consider for what case is the expression they derive for hole boring valid. The case they are interested in is what happens if the energy available for an ion to gain from crossing the pseudo-capacitor is less than the kinetic energy associated with the hole boring velocity. Their analysis applies for non-relativistic hole boring velocities and circular polarised laser pulses. This theory is now updated for the ZVP mechanism (linear polarised and relativistic ion velocities).

The so-called ‘piston’ which leads to ion hole boring is the pseudocapacitor field. In section 2.2.1, the development of that field is discussed quantitatively. The peak electric field is

$$E_C = E_L = \sqrt{\frac{I}{\epsilon_0 c}} \quad (3.29)$$

and the peak displacement of electrons is

$$\Delta x = \frac{\epsilon_0 E_C}{en_e}. \quad (3.30)$$

Considering instead the relativistic kinetic energy gained by an ion were it to fully cross the pseudocapacitor, following equation 2.25,

$$T_i = Z_i \times \frac{1}{2} m_e c^2 \frac{a_0^2}{n_e} = \frac{IZ_i}{2cn_{mathrm{e}}}. \quad (3.31)$$

(The equation above needs more thinking about)

Ions are reflected provided,

$$T_i > \frac{1}{2} m_i v_{HB}^2. \quad (3.32)$$

Hmm ok so in Vincenti, they approximate electron mass as much less than ion mass and therefore neglect it in the momentum calculation. It also looks like they have not done full relativistic calculation, so I cannot yet say I have that. But carrying on the derivation using Vincenti expression for simplicity:

The hole-boring velocity as calculated by Vincenti *et al* [117] is

$$\frac{v_{\text{HB}}}{c} = \sqrt{\frac{R \cos \theta}{2}} \quad (3.33)$$

So come back to this section, once I have fully written out the hole boring calculation in full, include also the multiple ion species stuff and this condition.

The upshot of this condition is something like: require no low charge to mass ratio ions (ie v heavy ions) and fully ionisation, these conditions are satisfied in this area of study.

To arrive at that result, useful parts include: composite mass density $\rho = \sum_i m_i n_i$, $m_i = A_i / N_A$ and $A_i \approx 2Z_i$ for most low mass ions relevant in these plasmas.

3.3 Thinking about the ZVP calculation

When I run sims on oblique incidence, this is another theorem that could be interesting to test.

Consider now that the surface moves inwards at speed c . In a time Δt , an energy $\sim B_L^2 \Delta t$ is incident on the surface. If at such a point, there exists a pseudocapacitor with electric field $E_C \sim n_e x_e$, then the work done by pushing it inwards is $\sim E_C n_e x_e \Delta x \sim E_C^2 \Delta t$, since surface moving inwards at speed c . Thus by conservation of energy, the reflected field is $B_R^2 = B_L^2 - E_C^2$. Note that at max displacement this cannot possibly be the case and we do see that the surface stops moving inwards, however this could be due to a reduction in the laser pulse intensity since the peak has passed. Thus this could be a reasonable approximation of the phenomena.

Then the force equilibrium expression in the boosted frame is

$$-B_L - \sqrt{B_L^2 - E_C^2} \pm B_i + E_C \quad (3.34)$$

working this through one finds,

$$x_p = \frac{\cos^2 \theta}{kS} \frac{2(1 \pm \sin \theta)}{\sin^2 \theta \pm 2 \sin \theta + 2} \quad (3.35)$$

$$T \sim \left(\frac{\cos^2 \theta}{kS} \frac{2(1 \pm \sin \theta)}{\sin^2 \theta \pm 2 \sin \theta + 2} \right) \quad (3.36)$$

And thus now predicting an optimum for electron energy at $\theta \approx 30^\circ$. That is quite different. It also looks nicer so I would like this to be right.

Another thing I still need to do is gonoskov technique to get bunch thickness, also do ZVP calculation in the exponential preplasma.

3.4 Things I may want to include or random notes

Note that ZVP does not describe the peak energies in the bunches, then JxB applies, since there are always some electrons outside of the well defined sharp boundary when the density is not high enough to impose adiabaticity.

Appendices

A

General plasma physics

Contents

A.1	Lorentz transformations of electromagnetic fields	83
A.2	The headlight effect	84
A.3	Geometric transverse emittance	84

A.1 Lorentz transformations of electromagnetic fields

The Lorentz transformations for electromagnetic field components parallel, \parallel , and perpendicular, \perp , to a frame of reference boost of velocity \mathbf{v} are [73]

$$\mathbf{E}'_{\parallel} = \mathbf{E}_{\parallel}, \quad (\text{A.1})$$

$$\mathbf{B}'_{\parallel} = \mathbf{B}_{\parallel}, \quad (\text{A.2})$$

$$\mathbf{E}'_{\perp} = \gamma_{\mathbf{v}}(\mathbf{E}_{\perp} + \mathbf{v} \times \mathbf{B}), \quad (\text{A.3})$$

$$\mathbf{B}'_{\perp} = \gamma_{\mathbf{v}}(\mathbf{B}_{\perp} - \mathbf{v} \times \mathbf{E}/c^2). \quad (\text{A.4})$$

A.2 The headlight effect

The headlight effect describes the beaming of an isotropically emitting source travelling at some velocity relative to an observer. Consider the geometry of figure 2.2 with the source (the laser pulse) travelling at an angle 2θ to the observer (in this case, the ablating front). A photon with energy E emitted from the rest frame of the source (the laboratory frame in this case) has a 4-momentum

$$\mathbf{P}_\mu = \left(\frac{E}{c}, \frac{E}{c} \cos 2\theta, \frac{E}{c} \sin 2\theta \right). \quad (\text{A.5})$$

As the interaction geometry is confined to a 2D plane, the z -component can be safely neglected. Applying the lorentz boost of equation 1.30,

$$\begin{aligned} \frac{E'}{c} &= \gamma \left(\frac{E}{c} - \beta \frac{E}{c} \cos 2\theta \right) \\ \frac{E'}{c} \cos 2\theta' &= \gamma \left(\frac{E}{c} \cos 2\theta - \beta \frac{E}{c} \right). \end{aligned} \quad (\text{A.6})$$

Solving these equations for the angle in the boosted frame,

$$\cos 2\theta' = \frac{\cos 2\theta - \beta}{1 - \beta \cos 2\theta}. \quad (\text{A.7})$$

A.3 Geometric transverse emittance

A beam¹ of particles is fully described by its six-dimensional particle phase space distribution

$$\rho(\mathbf{x}, \mathbf{p}) = \rho(x, p_x, y, p_y, z, p_z), \quad (\text{A.8})$$

where $\mathbf{p} = p_x \hat{\mathbf{x}} + p_y \hat{\mathbf{y}} + p_z \hat{\mathbf{z}}$ is the canonical momentum [157]. Under the Hamilton formalism, for ideal conditions, the six-dimensional volume of the beam in this space, termed the *emittance*, arises as a conserved quantity and is therefore a useful quantity to describe the beam quality. (something to do with it affecting the ability to focus the beam?? check the papers) It is useful to rotate the coordinate system so as to align with the beam's propagation. The distribution can be written as

$$\rho(\mathbf{x}', \mathbf{p}') = \rho(x_L, p_L, x_T, p_T, x_{T'}, p_{T'}), \quad (\text{A.9})$$

¹In this section it is electron beams and not bunches that are referred to to demonstrate the generality of these concepts.

where L is longitudinal to the beam's propagation direction, and T and T' are two orthogonal directions transverse to the beam's propagation. Where discussed in this thesis, T' will unanimously refer to the z -direction, that is, the additional direction in 3D simulations, all such simulations are designed such that the z -direction is transverse to the beam propagation direction.

Recording a six-dimensional phase space in experiment is impossible while in simulations it is almost prohibitively costly in terms of data storage. Hence, it is common practice to project the distribution onto three orthogonal sub-spaces corresponding to each spatial axis, L, T and T' and compute the area on each. Note that since the electron beam is ultra-relativistic, all electrons propagate at approximately c and therefore it is the transverse and not the longitudinal emittance that describes the beam's quality. As a particle beam does not typically exist with well-defined borders, the area used to describe the emittance is restricted to an ellipse containing only the high-density core of the distribution. For a subspace i , where $i = T$ or T' , Floettmann *et al* [158] derive the *transverse normalised emittance* as

$$\epsilon_{n,rms}^i = \frac{1}{m_e c} \sqrt{\langle x_i^2 \rangle \langle p_i^2 \rangle - \langle x_i p_i \rangle^2}, \quad (\text{A.10})$$

where $\langle \rangle$ is the second central moment of the particle distribution,

$$\langle ab \rangle = \frac{\int ab\rho(\mathbf{x}', \mathbf{p}')dV}{\int \rho(\mathbf{x}', \mathbf{p}')dV} - \frac{\int a\rho(\mathbf{x}', \mathbf{p}')dV \int b\rho(\mathbf{x}', \mathbf{p}')dV}{(\int \rho(\mathbf{x}', \mathbf{p}')dV)^2}, \quad (\text{A.11})$$

here $dV = \Pi_j dx_j dp_j$ for $j = L, T, T'$.

When working with emittances, most frequently in the literature it is the *transverse geometric emittance*, ϵ_{rms}^i that is discussed. This is a natural consequence of it being more readily accessible in experiments [**McDonald Methods of emittance measurement 1989**]. The geometric and normalised emittances are related via

$$\epsilon_{rms}^i = \frac{\epsilon_{rms}^i}{\gamma \beta_L}, \quad (\text{A.12})$$

where $\gamma = 1/\sqrt{1-\beta^2}$ refers to the beam's mean energy and $\beta_L \approx c$ is the ultrarelativistic beam's longitudinal speed.

The Courant-Snyder invariant which describes the ellipse that corresponds to the emittance is²

$$\epsilon_{\text{rms}}^i = \gamma x_i^2 + 2\alpha x x' \beta x_i'^2, \quad (\text{A.13})$$

here the coordinates are x_i and $x'_i = p_i/p_L$ [159]. The Twiss parameters are

$$\alpha = -\frac{\langle x_i x'_i \rangle}{\epsilon_{\text{rms}}^i}, \quad (\text{A.14})$$

$$\beta = \frac{\langle x_i \rangle}{\epsilon_{\text{rms}}^i} \quad (\text{A.15})$$

and

$$\gamma = \frac{\langle x_i'^2 \rangle}{\epsilon_{\text{rms}}^i}. \quad (\text{A.16})$$

Thus the shape of the ellipse and the divergence of the beam can be determined.

²Regrettably β and γ are the standard notations for the Twiss parameters, at all other locations in this thesis, these parameters will refer to the standard relativistic beta and gamma factors of objects respectively.

B

PIC simulations

Contents

B.1 Convergence of 3D PIC simulations	87
---	----

B.1 Convergence of 3D PIC simulations

To reduce the computation cost of the large 3D simulations, a lower resolution version of the original 3D simulation was performed. Results are presented in figure B.1, demonstrating reasonable convergence.

B.1. Convergence of 3D PIC simulations

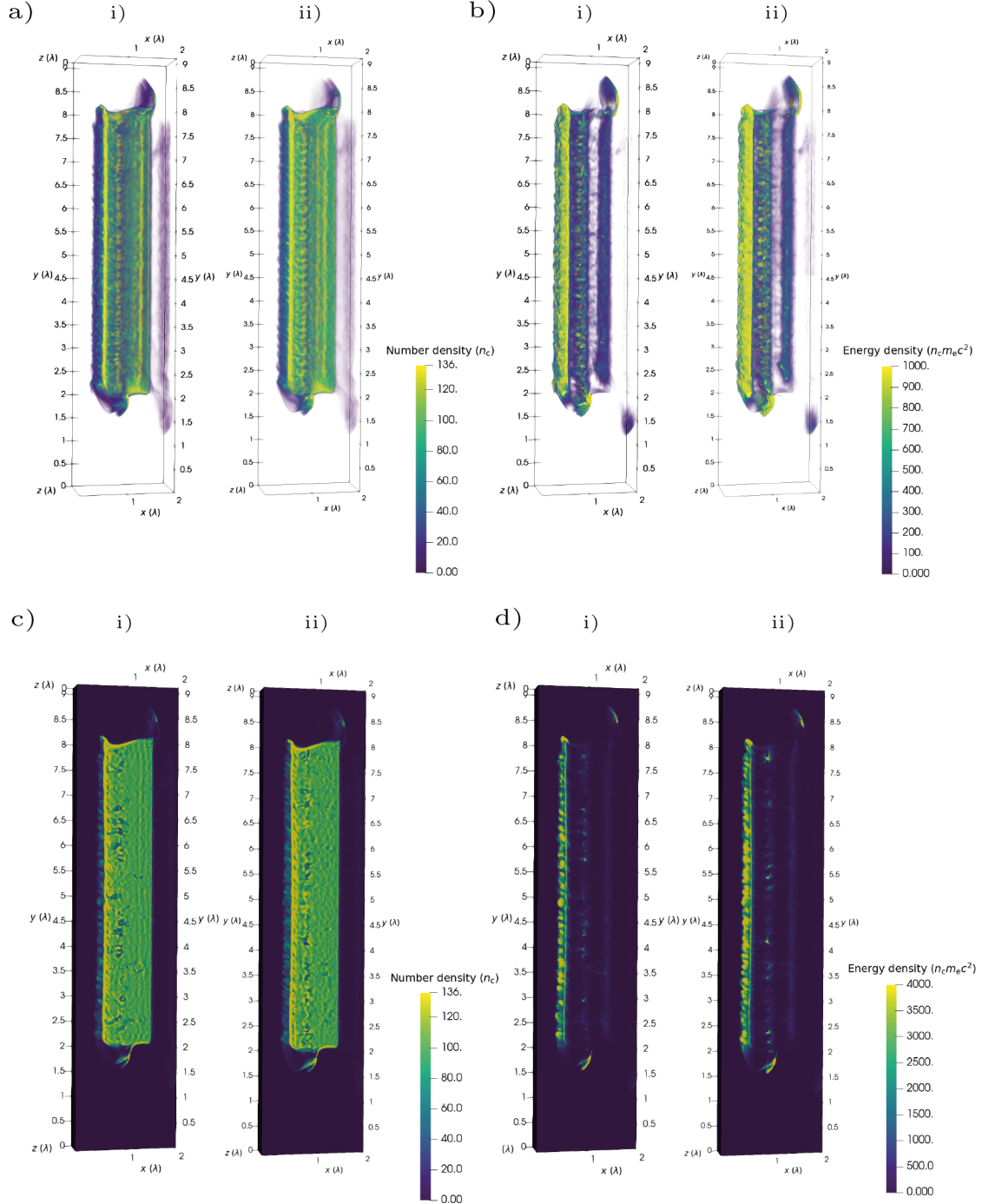


Figure B.1: Comparison between the initial 3D simulation and a lower resolution version. a) Electron number density. b) Kinetic energy density. c) and d) are slices of a) and b) respectively. *i)* Initial simulation. *ii)* Lower resolution simulation. Good convergence is demonstrated.

References

- [1] Douglas Kothe, Stephen Lee, and Irene Qualters. “Exascale Computing in the United States”. In: *Computing in Science & Engineering* 21.1 (Jan. 2019), pp. 17–29. (Visited on 09/26/2023).
- [2] Donna Strickland and Gerard Mourou. “Compression of Amplified Chirped Optical Pulses”. In: *Optics Communications* 55.6 (Oct. 1985), pp. 447–449. (Visited on 08/31/2023).
- [3] I.N. Ross, P. Matousek, and J.L. Collier. “Optical Parametric Chirped Pulse Amplification”. In: *Conference on Lasers and Electro-Optics (CLEO 2000). Technical Digest. Postconference Edition. TOPS Vol.39 (IEEE Cat. No.00CH37088)*. San Francisco, CA, USA: IEEE, 2000, p. 249. (Visited on 09/26/2023).
- [4] S. Fourmaux et al. “Pedestal Cleaning for High Laser Pulse Contrast Ratio with a 100 TW Class Laser System”. In: *Optics Express* 19.9 (Apr. 2011), p. 8486. (Visited on 09/20/2023).
- [5] Yong Wang et al. “085 PW Laser Operation at 33 Hz and High-Contrast Ultrahigh-Intensity $\lambda = 400$ nm Second-Harmonic Beamline”. In: *Optics Letters* 42.19 (Oct. 2017), p. 3828. (Visited on 09/19/2023).
- [6] G. Tiscareno et al. “The Ohio State University Scarlet Laser Facility - Open To External Users Via LaserNetUS”. In: 2020 (Jan. 2020), CP15.001. (Visited on 09/19/2023).
- [7] Jae Hee Sung et al. “42 PW, 20 fs Ti:Sapphire Laser at 01 Hz”. In: *Optics Letters* 42.11 (June 2017), p. 2058. (Visited on 09/19/2023).
- [8] Ian N. Ross et al. “Generation of Terawatt Pulses by Use of Optical Parametric Chirped Pulse Amplification”. In: *Applied Optics* 39.15 (May 2000), p. 2422. (Visited on 09/20/2023).
- [9] Xiaodong Yang et al. “Multiterawatt Laser System Based on Optical Parametric Chirped Pulse Amplification”. In: *Optics Letters* 27.13 (July 2002), p. 1135. (Visited on 09/20/2023).
- [10] Stefan Witte et al. “A Source of 2 Terawatt, 2.7 Cycle Laser Pulses Based on Noncollinear Optical Parametric Chirped Pulse Amplification”. In: *Optics Express* 14.18 (2006), pp. 8168–8177.
- [11] C. Stoeckl et al. “High-Energy Petawatt Project at the University of Rochester’s Laboratory for Laser Energetics”. In: *Fusion Science and Technology* 49.3 (Apr. 2006), pp. 367–373. (Visited on 09/19/2023).
- [12] V V Lozhkarev et al. “Compact 0.56 Petawatt Laser System Based on Optical Parametric Chirped Pulse Amplification in KD*P Crystals”. In: *Laser Physics Letters* 4.6 (June 2007), pp. 421–427. (Visited on 09/20/2023).

- [13] Daniel Herrmann et al. “Generation of Sub-Three-Cycle, 16 TW Light Pulses by Using Noncollinear Optical Parametric Chirped-Pulse Amplification”. In: *Optics Letters* 34.16 (Aug. 2009), p. 2459. (Visited on 09/20/2023).
- [14] Giedrius Andriukaitis et al. “90 GW Peak Power Few-Cycle Mid-Infrared Pulses from an Optical Parametric Amplifier”. In: *Optics Letters* 36.15 (Aug. 2011), p. 2755. (Visited on 09/20/2023).
- [15] Kun Zhao et al. “Generation of 120 GW Mid-Infrared Pulses from a Widely Tunable Noncollinear Optical Parametric Amplifier”. In: *Optics Letters* 38.13 (July 2013), p. 2159. (Visited on 09/20/2023).
- [16] Nicholas Hopps et al. “Overview of Laser Systems for the Orion Facility at the AWE”. In: *Applied Optics* 52.15 (May 2013), p. 3597. (Visited on 09/11/2023).
- [17] Nicolas Thiré et al. “10 mJ 5-Cycle Pulses at $1.8 \mu\text{m}$ through Optical Parametric Amplification”. In: *Applied Physics Letters* 106.9 (Mar. 2015), p. 091110. (Visited on 09/20/2023).
- [18] Yanchun Yin et al. “High-Efficiency Optical Parametric Chirped-Pulse Amplifier in BiB₃O₆ for Generation of 3 mJ, Two-Cycle, Carrier-Envelope-Phase-Stable Pulses at 17 Mm”. In: *Optics Letters* 41.6 (Mar. 2016), p. 1142. (Visited on 09/20/2023).
- [19] S Gales et al. “The Extreme Light Infrastructure—Nuclear Physics (ELI-NP) Facility: New Horizons in Physics with 10 PW Ultra-Intense Lasers and 20 MeV Brilliant Gamma Beams”. In: *Reports on Progress in Physics* 81.9 (Sept. 2018), p. 094301. (Visited on 09/19/2023).
- [20] *OMEGA Facility*. Lle.rochester.edu/omega facility.
- [21] J. Ren et al. “A Compact Double-Pass Raman Backscattering Amplifier/Compressor”. In: *Physics of Plasmas* 15.5 (May 2008), p. 056702. (Visited on 09/20/2023).
- [22] L. Lancia et al. “Experimental Evidence of Short Light Pulse Amplification Using Strong-Coupling Stimulated Brillouin Scattering in the Pump Depletion Regime”. In: *Physical Review Letters* 104.2 (Jan. 2010), p. 025001. (Visited on 09/20/2023).
- [23] L. Lancia et al. “Signatures of the Self-Similar Regime of Strongly Coupled Stimulated Brillouin Scattering for Efficient Short Laser Pulse Amplification”. In: *Physical Review Letters* 116.7 (Feb. 2016), p. 075001. (Visited on 09/20/2023).
- [24] J.-R. Marquès et al. “Joule-Level High-Efficiency Energy Transfer to Subpicosecond Laser Pulses by a Plasma-Based Amplifier”. In: *Physical Review X* 9.2 (Apr. 2019), p. 021008. (Visited on 09/20/2023).
- [25] Francis Théberge et al. “Tunable Ultrashort Laser Pulses Generated through Filamentation in Gases”. In: *Physical Review Letters* 97.2 (July 2006), p. 023904. (Visited on 09/20/2023).
- [26] Sergei A. Trushin et al. “Sub-10-Fs Supercontinuum Radiation Generated by Filamentation of Few-Cycle 800 Nm Pulses in Argon”. In: *Optics Letters* 32.16 (Aug. 2007), p. 2432. (Visited on 09/20/2023).
- [27] T I Oh et al. “Intense Terahertz Generation in Two-Color Laser Filamentation: Energy Scaling with Terawatt Laser Systems”. In: *New Journal of Physics* 15.7 (July 2013), p. 075002. (Visited on 09/20/2023).

- [28] Takuya Horio, Roman Spesyvtsev, and Toshinori Suzuki. “Generation of Sub-17 fs Vacuum Ultraviolet Pulses at 133 nm Using Cascaded Four-Wave Mixing through Filamentation in Ne”. In: *Optics Letters* 39.20 (Oct. 2014), p. 6021. (Visited on 09/20/2023).
- [29] Eiji Takahashi, Yasuo Nabekawa, and Katsumi Midorikawa. “Generation of 10- μ J Coherent Extreme-Ultraviolet Light by Use of High-Order Harmonics”. In: *Optics Letters* 27.21 (Nov. 2002), p. 1920. (Visited on 09/20/2023).
- [30] E. Goulielmakis et al. “Single-Cycle Nonlinear Optics”. In: *Science* 320.5883 (June 2008), pp. 1614–1617. (Visited on 09/20/2023).
- [31] E. Skantzakis et al. “Coherent Continuum Extreme Ultraviolet Radiation in the Sub-100-nJ Range Generated by a High-Power Many-Cycle Laser Field”. In: *Optics Letters* 34.11 (June 2009), p. 1732. (Visited on 09/20/2023).
- [32] F. Ferrari et al. “High-Energy Isolated Attosecond Pulses Generated by above-Saturation Few-Cycle Fields”. In: *Nature Photonics* 4.12 (Dec. 2010), pp. 875–879. (Visited on 09/20/2023).
- [33] Eiji J. Takahashi et al. “Attosecond Nonlinear Optics Using Gigawatt-Scale Isolated Attosecond Pulses”. In: *Nature Communications* 4.1 (Oct. 2013), p. 2691. (Visited on 09/19/2023).
- [34] Dimitar Popmintchev et al. “Ultraviolet Surprise: Efficient Soft x-Ray High-Harmonic Generation in Multiply Ionized Plasmas”. In: *Science* 350.6265 (Dec. 2015), pp. 1225–1231. (Visited on 09/20/2023).
- [35] Y. Nomura et al. “Attosecond Phase Locking of Harmonics Emitted from Laser-Produced Plasmas”. In: *Nature Physics* 5.2 (Feb. 2009), pp. 124–128. (Visited on 09/20/2023).
- [36] J Bierbach et al. “Generation of 10 μ W Relativistic Surface High-Harmonic Radiation at a Repetition Rate of 10 Hz”. In: *New Journal of Physics* 14.6 (June 2012), p. 065005. (Visited on 09/20/2023).
- [37] P. Heissler et al. “Multi- μ J Harmonic Emission Energy from Laser-Driven Plasma”. In: *Applied Physics B* 118.2 (Feb. 2015), pp. 195–201. (Visited on 09/20/2023).
- [38] M. Yeung et al. “Experimental Observation of Attosecond Control over Relativistic Electron Bunches with Two-Colour Fields”. In: *Nature Photonics* 11.1 (Jan. 2017), pp. 32–35. (Visited on 09/04/2023).
- [39] Olga Jahn et al. “Towards Intense Isolated Attosecond Pulses from Relativistic Surface High Harmonics”. In: *Optica* 6.3 (Mar. 2019), p. 280. (Visited on 09/20/2023).
- [40] B. Rus et al. “Efficient, High-Brightness Soft-x-Ray Laser at 21.2 nm”. In: *Physical Review A* 55.5 (May 1997), pp. 3858–3873. (Visited on 09/20/2023).
- [41] S. Sebban et al. “Full Characterization of a High-Gain Saturated x-Ray Laser at 13.9 nm”. In: *Physical Review A* 61.4 (Mar. 2000), p. 043810. (Visited on 09/20/2023).
- [42] B. Rus. “Multi-Millijoule, Highly Coherent X-ray Laser at 21 nm as a Routine Tool for Applications”. In: *AIP Conference Proceedings*. Vol. 641. Aspen, Colorado (USA): AIP, 2002, pp. 182–190. (Visited on 09/20/2023).

- [43] Ph. Zeitoun et al. “A High-Intensity Highly Coherent Soft X-ray Femtosecond Laser Seeded by a High Harmonic Beam”. In: *Nature* 431.7007 (Sept. 2004), pp. 426–429. (Visited on 09/20/2023).
- [44] Y. Wang et al. “High-Brightness Injection-Seeded Soft-X-Ray-Laser Amplifier Using a Solid Target”. In: *Physical Review Letters* 97.12 (Sept. 2006), p. 123901. (Visited on 09/20/2023).
- [45] Nina Rohringer et al. “Atomic Inner-Shell X-ray Laser at 1.46 Nanometres Pumped by an X-ray Free-Electron Laser”. In: *Nature* 481.7382 (Jan. 2012), pp. 488–491. (Visited on 09/20/2023).
- [46] V. Ayvazyan et al. “First Operation of a Free-Electron Laser Generating GW Power Radiation at 32 Nm Wavelength”. In: *The European Physical Journal D* 37.2 (Feb. 2006), pp. 297–303. (Visited on 09/20/2023).
- [47] W. Ackermann et al. “Operation of a Free-Electron Laser from the Extreme Ultraviolet to the Water Window”. In: *Nature Photonics* 1.6 (June 2007), pp. 336–342. (Visited on 09/20/2023).
- [48] P. Emma et al. “First Lasing and Operation of an Ångstrom-Wavelength Free-Electron Laser”. In: *Nature Photonics* 4.9 (Sept. 2010), pp. 641–647. (Visited on 09/20/2023).
- [49] *Flash Free-Electron Laser*. flash.desy.de.
- [50] *FELIX Laboratory: Overview and Specifications*. ru.nl/felix/facility/overview-specification/.
- [51] S. Kneip et al. “Observation of Synchrotron Radiation from Electrons Accelerated in a Petawatt-Laser-Generated Plasma Cavity”. In: *Physical Review Letters* 100.10 (Mar. 2008), p. 105006. (Visited on 09/20/2023).
- [52] S. Kneip et al. “Bright Spatially Coherent Synchrotron X-rays from a Table-Top Source”. In: *Nature Physics* 6.12 (Dec. 2010), pp. 980–983. (Visited on 09/20/2023).
- [53] J. Ju et al. “Enhancement of X-Rays Generated by a Guided Laser Wakefield Accelerator inside Capillary Tubes”. In: *Applied Physics Letters* 100.19 (May 2012), p. 191106. (Visited on 09/20/2023).
- [54] L. M. Chen et al. “Bright Betatron X-ray Radiation from a Laser-Driven-Clustering Gas Target”. In: *Scientific Reports* 3.1 (May 2013), p. 1912. (Visited on 09/20/2023).
- [55] Xiaoming Wang et al. “Quasi-Monoenergetic Laser-Plasma Acceleration of Electrons to 2 GeV”. In: *Nature Communications* 4.1 (June 2013), p. 1988. (Visited on 09/20/2023).
- [56] J. M. Cole et al. “Laser-Wakefield Accelerators as Hard x-Ray Sources for 3D Medical Imaging of Human Bone”. In: *Scientific Reports* 5.1 (Aug. 2015), p. 13244. (Visited on 09/20/2023).
- [57] J. Wenz et al. “Quantitative X-ray Phase-Contrast Microtomography from a Compact Laser-Driven Betatron Source”. In: *Nature Communications* 6.1 (July 2015), p. 7568. (Visited on 09/20/2023).
- [58] K. Ta Phuoc et al. “All-Optical Compton Gamma-Ray Source”. In: *Nature Photonics* 6.5 (May 2012), pp. 308–311. (Visited on 09/20/2023).

- [59] S. Chen et al. “MeV-Energy X Rays from Inverse Compton Scattering with Laser-Wakefield Accelerated Electrons”. In: *Physical Review Letters* 110.15 (Apr. 2013), p. 155003. (Visited on 09/20/2023).
- [60] Hai-En Tsai et al. “Compact Tunable Compton X-Ray Source from Laser-Plasma Accelerator and Plasma Mirror”. In: *Physics of Plasmas* 22.2 (Feb. 2015), p. 023106. (Visited on 09/20/2023).
- [61] Mikhail N. Polyanskiy, Igor V. Pogorelsky, and Vitaly Yakimenko. “Picosecond Pulse Amplification in Isotopic CO₂ Active Medium”. In: *Optics Express* 19.8 (Apr. 2011), p. 7717. (Visited on 09/20/2023).
- [62] D. Haberberger, S. Tochitsky, and C. Joshi. “Fifteen Terawatt Picosecond CO₂ Laser System”. In: *Optics Express* 18.17 (Aug. 2010), p. 17865. (Visited on 09/20/2023).
- [63] J. H. Gownia, M. Kaschke, and P. P. Sorokin. “Amplification of 193-Nm Femtosecond Seed Pulses Generated by Third-Order, Nonresonant, Difference-Frequency Mixing in Xenon”. In: *Optics Letters* 17.5 (Mar. 1992), p. 337. (Visited on 09/20/2023).
- [64] M. Kando et al. “Enhancement of Photon Number Reflected by the Relativistic Flying Mirror”. In: *Physical Review Letters* 103.23 (Dec. 2009), p. 235003. (Visited on 09/20/2023).
- [65] Stephen Obenschain et al. “High-Energy Krypton Fluoride Lasers for Inertial Fusion”. In: *Applied Optics* 54.31 (Nov. 2015), F103. (Visited on 09/20/2023).
- [66] R. M. G. M. Trines et al. “Simulations of Efficient Raman Amplification into the Multipetawatt Regime”. In: *Nature Physics* 7.1 (Jan. 2011), pp. 87–92. (Visited on 09/20/2023).
- [67] J. Kawanaka et al. “Conceptual Design of Sub-Exa-Watt System by Using Optical Parametric Chirped Pulse Amplification”. In: *Journal of Physics: Conference Series* 688 (Mar. 2016), p. 012044. (Visited on 09/20/2023).
- [68] Toshiki Tajima. “Marriage of a 20keV Superconducting XFEL with a 100PW Laser”. In: *SPIE* (Apr. 2018).
- [69] *Net Electricity Consumption Worldwide in Select Years from 1980 to 2022 (in Terawatt-Hours)*. <https://www.statista.com/statistics/280704/world-power-consumption/>. (Visited on 09/26/2023).
- [70] F. Dollar et al. “Enhanced Laser Absorption from Radiation Pressure in Intense Laser Plasma Interactions”. In: *New Journal of Physics* 19.6 (June 2017).
- [71] P. R. Drake and Peter Norreys. “Focus on High Energy Density Physics”. In: *New Journal of Physics* 16 (2014).
- [72] Francis F. Chen. *Introduction to Plasma Physics and Controlled Fusion*. Cham: Springer International Publishing, 2016. (Visited on 09/26/2023).
- [73] Andrew M. Steane. *Relativity Made Relatively Easy*. OUP Oxford, Oct. 2012.
- [74] J. Derouillat et al. “Smilei : A Collaborative, Open-Source, Multi-Purpose Particle-in-Cell Code for Plasma Simulation”. In: *Computer Physics Communications* 222 (Jan. 2018), pp. 351–373. (Visited on 08/15/2023).

- [75] E. Esarey, C. B. Schroeder, and W. P. Leemans. “Physics of Laser-Driven Plasma-Based Electron Accelerators”. In: *Reviews of Modern Physics* 81.3 (Aug. 2009), pp. 1229–1285. (Visited on 08/31/2023).
- [76] Eduard Atonga et al. “Gravitational Waves from High-Power Twisted Light”. In: (2023). (Visited on 09/26/2023).
- [77] S. Gordienko and A. Pukhov. “Scalings for Ultrarelativistic Laser Plasmas and Quasimonoenergetic Electrons”. In: *Physics of Plasmas* 12.4 (Apr. 2005), p. 043109. (Visited on 09/28/2023).
- [78] V. I. Eremin, A. V. Korzhimanov, and A. V. Kim. “Relativistic Self-Induced Transparency Effect During Ultraintense Laser Interaction with Overdense Plasmas: Why It Occurs and Its Use for Ultrashort Electron Bunch Generation”. In: *Physics of Plasmas* 17.4 (Apr. 2010), p. 043102. arXiv: 0810.4035 [physics]. (Visited on 08/31/2023).
- [79] Herbert Goldstein. *Classical Mechanics*. Pearson Education, 2013.
- [80] Igor V. Sokolov et al. “Dynamics of Emitting Electrons in Strong Electromagnetic Fields”. In: *Physics of Plasmas* 16.9 (Sept. 2009), p. 093115. arXiv: 0904.0405 [physics]. (Visited on 08/01/2023).
- [81] Luca Fedeli et al. “Probing Strong-Field QED with Doppler-boosted PetaWatt-class Lasers”. In: (Dec. 2020). arXiv: 2012.07696.
- [82] F. Niel et al. “From Quantum to Classical Modeling of Radiation Reaction: A Focus on Stochasticity Effects”. In: *Physical Review E* 97.4 (Apr. 2018), p. 043209. (Visited on 10/02/2023).
- [83] V. I. Ritus. “Quantum Effects of the Interaction of Elementary Particles with an Intense Electromagnetic Field”. In: *Journal of Soviet Laser Research* 6.5 (1985), pp. 497–617. (Visited on 10/02/2023).
- [84] Jon T. Larsen and Stephen M. Lane. “HYADES—A Plasma Hydrodynamics Code for Dense Plasma Studies”. In: *Journal of Quantitative Spectroscopy and Radiative Transfer* 51.1-2 (Jan. 1994), pp. 179–186. (Visited on 09/28/2023).
- [85] B. Fryxell et al. “FLASH: An Adaptive Mesh Hydrodynamics Code for Modeling Astrophysical Thermonuclear Flashes”. In: *The Astrophysical Journal Supplement Series* 131.1 (Nov. 2000), pp. 273–334. (Visited on 09/28/2023).
- [86] R. A. Fonseca et al. “OSIRIS: A Three-Dimensional, Fully Relativistic Particle in Cell Code for Modeling Plasma Based Accelerators”. In: *Computational Science — ICCS 2002*. Ed. by Gerhard Goos et al. Vol. 2331. Berlin, Heidelberg: Springer Berlin Heidelberg, 2002, pp. 342–351. (Visited on 09/28/2023).
- [87] Keith Bennett et al. “Users Manual for the EPOCH PIC Codes”. In: *University of Warwick* (2017).
- [88] ARCHER2. <https://www.archer2.ac.uk/>. (Visited on 08/15/2023).
- [89] SCARF Overview. <https://www.scarf.rl.ac.uk>.
- [90] N.J. Sircombe and T.D. Arber. “VALIS: A Split-Conservative Scheme for the Relativistic 2D Vlasov–Maxwell System”. In: *Journal of Computational Physics* 228.13 (July 2009), pp. 4773–4788. (Visited on 09/28/2023).

- [91] A. Bruce Langdon and Charles K. Birdsall. “Theory of Plasma Simulation Using Finite-Size Particles”. In: *The Physics of Fluids* 13.8 (Aug. 1970), pp. 2115–2122. (Visited on 09/13/2023).
- [92] Jay Boris. “Relativistic Plasma Simulation-Optimization of a Hybrid Code”. In: 1970, pp. 3–67. (Visited on 08/31/2023).
- [93] T.Zh. Esirkepov. “Exact Charge Conservation Scheme for Particle-in-Cell Simulation with an Arbitrary Form-Factor”. In: *Computer Physics Communications* 135.2 (Apr. 2001), pp. 144–153. (Visited on 09/28/2023).
- [94] Allen Taflove. “Computational Electromagnetics: The Finite-Difference Time-Domain Method”. In: *The Electrical Engineering Handbook*. Boston: Elsevier Academic Press, 2005, pp. 629–669.
- [95] H. Barucq and B. Hanouzet. “Asymptotic Behavior of Solutions to Maxwell’s System in Bounded Domains with Absorbing Silver–Müller’s Condition on the Exterior Boundary”. In: *Asymptotic Analysis* 15.1 (1997), pp. 25–40. (Visited on 10/03/2023).
- [96] *Collisions*. <https://osiris-code.github.io/osiris/reference/collisions>.
- [97] F. Pérez et al. “Improved Modeling of Relativistic Collisions and Collisional Ionization in Particle-in-Cell Codes”. In: *Physics of Plasmas* 19.8 (Aug. 2012), p. 083104. (Visited on 10/03/2023).
- [98] M. Vranic et al. “Particle Merging Algorithm for PIC Codes”. In: *Computer Physics Communications* 191 (June 2015), pp. 65–73. (Visited on 10/03/2023).
- [99] Hideo Okuda and Charles K. Birdsall. “Collisions in a Plasma of Finite-Size Particles”. In: *The Physics of Fluids* 13.8 (Aug. 1970), pp. 2123–2134. (Visited on 10/03/2023).
- [100] Carlos A. De Moura and Carlos S. Kubrusly, eds. *The Courant–Friedrichs–Lewy (CFL) Condition: 80 Years After Its Discovery*. Boston: Birkhäuser Boston, 2013. (Visited on 10/03/2023).
- [101] Charles K Birdsall and A Bruce Langdon. *Plasma Physics via Computer Simulation*. CRC press, 2004.
- [102] J.U. Brackbill. “On Energy and Momentum Conservation in Particle-in-Cell Plasma Simulation”. In: *Journal of Computational Physics* 317 (July 2016), pp. 405–427. (Visited on 09/21/2023).
- [103] T D Arber et al. “Contemporary Particle-in-Cell Approach to Laser-Plasma Modelling”. In: *Plasma Physics and Controlled Fusion* 57.11 (Nov. 2015), p. 113001. (Visited on 09/16/2023).
- [104] Victor V. Kulagin et al. “Characteristics of Relativistic Electron Mirrors Generated by an Ultrashort Nonadiabatic Laser Pulse from a Nanofilm”. In: *Physical Review E* 80.1 (July 2009), p. 016404. (Visited on 08/31/2023).
- [105] Li-Xiang Hu et al. “Enhanced Dense Attosecond Electron Bunch Generation by Irradiating an Intense Laser on a Cone Target”. In: *Physics of Plasmas* 22 (Apr. 2015), p. 033104.
- [106] Giada Cantono et al. “Extensive Study of Electron Acceleration by Relativistic Surface Plasmons”. In: *Physics of Plasmas* 25.3 (Mar. 2018), p. 031907. arXiv: 1802.05483 [physics]. (Visited on 08/31/2023).

- [107] D. A. Serebryakov, E. N. Nerush, and I. Yu Kostyukov. “Near-Surface Electron Acceleration during Intense Laser-Solid Interaction in the Grazing Incidence Regime”. In: *Physics of Plasmas* 24.12 (Dec. 2017), p. 123115. arXiv: 1708.09833 [physics]. (Visited on 08/31/2023).
- [108] Y. X. Zhang et al. “Giant Isolated Attosecond Pulses from Two-Color Laser-Plasma Interactions”. In: *Physical Review Letters* 124.11 (Mar. 2020), p. 114802. (Visited on 08/31/2023).
- [109] Vojtěch Horný and László Veisz. “Generation of Single Attosecond Relativistic Electron Bunch from Intense Laser Interaction with a Nanosphere”. In: *Plasma Physics and Controlled Fusion* 63.12 (Dec. 2021), p. 125025. (Visited on 10/03/2023).
- [110] J. F. Ong, P. Ghenuche, and K. A. Tanaka. “Electron Transport in a Nanowire Irradiated by an Intense Laser Pulse”. In: *Physical Review Research* 3.3 (Sept. 2021), p. 033262. (Visited on 08/31/2023).
- [111] Victor V. Kulagin et al. “Subrelativistic Infrared and Terahertz Pulses from Petawatt Class Laser Interaction with Complex Nanodimensional Targets”. In: *Relativistic Plasma Waves and Particle Beams as Coherent and Incoherent Radiation Sources IV*. Ed. by Dino A. Jaroszynski and MinSup Hur. Online Only, Czech Republic: SPIE, Apr. 2021, p. 11. (Visited on 08/31/2023).
- [112] Jinpu Lin et al. “Towards Isolated Attosecond Electron Bunches Using Ultrashort-Pulse Laser-Solid Interactions”. In: *Scientific Reports* 10.1 (Oct. 2020), p. 18354. (Visited on 08/31/2023).
- [113] D. E. Cardenas et al. “Sub-Cycle Dynamics in Relativistic Nanoplasma Acceleration”. In: *Scientific Reports* 9.1 (Dec. 2019).
- [114] M. Thévenet et al. “Vacuum Laser Acceleration of Relativistic Electrons Using Plasma Mirror Injectors”. In: *Nature Physics* 12.4 (Apr. 2016), pp. 355–360. arXiv: 1511.05936.
- [115] A. A. Gonoskov et al. “Ultrarelativistic Nanoplasmonics as a Route towards Extreme-Intensity Attosecond Pulses”. In: *Physical Review E* 84.4 (Oct. 2011), p. 046403. (Visited on 07/24/2023).
- [116] D. an der Brügge and A. Pukhov. “Enhanced Relativistic Harmonics by Electron Nanobunching”. In: *Physics of Plasmas* 17.3 (Mar. 2010), p. 033110. arXiv: 1002.3576 [physics]. (Visited on 08/31/2023).
- [117] H. Vincenti et al. “Optical Properties of Relativistic Plasma Mirrors”. In: *Nature Communications* 5 (Mar. 2014). arXiv: 1312.1908.
- [118] Andrea Macchi. “Theory of Light Sail Acceleration by Intense Lasers: An Overview”. In: *High Power Laser Science and Engineering* 2 (Apr. 2014), e10. (Visited on 08/31/2023).
- [119] S. Cousens et al. “Electron Trajectories Associated with Laser-Driven Coherent Synchrotron Emission at the Front Surface of Overdense Plasmas”. In: *Physical Review E* 101.5 (May 2020), p. 053210. (Visited on 08/31/2023).
- [120] A. F. Savin et al. “Attosecond-Scale Absorption at Extreme Intensities”. In: *Physics of Plasmas* 24.11 (Nov. 2017).

- [121] T. Baeva et al. “The Zero Vector Potential Mechanism of Attosecond Absorption”. In: *Physics of Plasmas* 18.5 (May 2011).
- [122] Alex Savin. “Modelling Laser-Plasma Interactions for the Next Generation of High-Power Laser Experiments”. In: (2019).
- [123] S C Wilks et al. *Absorption of Ultra-Intense Laser Pulses*. Tech. rep. 1992.
- [124] T. Baeva, S. Gordienko, and A. Pukhov. “Theory of High-Order Harmonic Generation in Relativistic Laser Interaction with Overdense Plasma”. In: *Physical Review E - Statistical, Nonlinear, and Soft Matter Physics* 74.4 (2006). arXiv: physics/0604228.
- [125] Matthew R. Edwards and Julia M. Mikhailova. “The X-Ray Emission Effectiveness of Plasma Mirrors: Reexamining Power-Law Scaling for Relativistic High-Order Harmonic Generation”. In: *Scientific Reports* 10.1 (Dec. 2020).
- [126] K. A. Tanaka et al. “Current Status and Highlights of the ELI-NP Research Program”. In: *Matter and Radiation at Extremes* 5.2 (Mar. 2020), p. 024402. (Visited on 08/31/2023).
- [127] A. Bret, L. Gremillet, and M. E. Dieckmann. “Multidimensional Electron Beam-Plasma Instabilities in the Relativistic Regime”. In: *Physics of Plasmas* 17.12 (Dec. 2010), p. 120501. (Visited on 08/31/2023).
- [128] Ferenc Krausz and Misha Ivanov. “Attosecond Physics”. In: *Reviews of Modern Physics* 81.1 (Feb. 2009), pp. 163–234. (Visited on 08/31/2023).
- [129] F Calegari et al. “Ultrafast Electron Dynamics in Phenylalanine Initiated by Attosecond Pulses”. In: () .
- [130] Eiji J Takahashi et al. “Nonlinear Attosecond Metrology by Intense Isolated Attosecond Pulses”. In: *IEEE JOURNAL OF SELECTED TOPICS IN QUANTUM ELECTRONICS* 21.5 (2015).
- [131] Yuya Morimoto and Peter Baum. “Diffraction and Microscopy with Attosecond Electron Pulse Trains”. In: *Nature Physics* 14.3 (Mar. 2018), pp. 252–256. (Visited on 09/19/2023).
- [132] W Schumaker. “Ultrafast Electron Radiography of Magnetic Fields in High-Intensity Laser-Solid Interactions”. In: *Physical Review Letters* 110.015003 (2013).
- [133] Joseph Duris et al. “Tunable Isolated Attosecond X-ray Pulses with Gigawatt Peak Power from a Free-Electron Laser”. In: *Nature Photonics* 14.1 (Jan. 2020), pp. 30–36. (Visited on 08/31/2023).
- [134] Y. Glinec et al. “Radiotherapy with Laser-plasma Accelerators: Monte Carlo Simulation of Dose Deposited by an Experimental Quasimonoenergetic Electron Beam”. In: *Medical Physics* 33.1 (Jan. 2006), pp. 155–162. (Visited on 09/19/2023).
- [135] S. Corde et al. “Femtosecond x Rays from Laser-Plasma Accelerators”. In: *Reviews of Modern Physics* 85.1 (Jan. 2013), pp. 1–48. (Visited on 08/31/2023).
- [136] K. Khrennikov et al. “Tunable All-Optical Quasimonochromatic Thomson X-Ray Source in the Nonlinear Regime”. In: *Physical Review Letters* 114.19 (May 2015), p. 195003. (Visited on 09/19/2023).

- [137] V V Kulagin, V N Kornienko, and V A Cherepenin. “Nonlinear Reflection of High-Amplitude Laser Pulses from Relativistic Electron Mirrors”. In: *Quantum Electronics* 46.4 (Apr. 2016), pp. 315–320. (Visited on 08/31/2023).
- [138] Ian Martin. *Diamond Light Source Upgrade*. Frascati, Italy (Remote), 2020.
- [139] He Ping. *The Progress of HEPS Project*. Frascati, Italy (Remote), 2020.
- [140] C Christou. “The Pre-Injector Linac for the Diamond Light Source”. In: (2004).
- [141] Alex F. Savin et al. “Energy Absorption in the Laser-QED Regime”. In: *Scientific Reports* 9.1 (Dec. 2019). arXiv: 1901.08017.
- [142] K. Miyauchi et al. “Laser Electron Acceleration by a Plasma Separator”. In: *Physics of Plasmas* 11.10 (Oct. 2004), pp. 4878–4881. (Visited on 08/31/2023).
- [143] Alexander Andreev, Konstantin Platonov, and Saltanat Sadykova. “Double Relativistic Electron Accelerating Mirror”. In: *Applied Sciences* 3.1 (Feb. 2013), pp. 94–106. (Visited on 08/31/2023).
- [144] M. Sherlock et al. “In-Depth Plasma-Wave Heating of Dense Plasma Irradiated by Short Laser Pulses”. In: *Physical Review Letters* 113.25 (Dec. 2014).
- [145] B. Chrisman, Y. Sentoku, and A. J. Kemp. “Intensity Scaling of Hot Electron Energy Coupling in Cone-Guided Fast Ignition”. In: *Physics of Plasmas* 15.5 (May 2008), p. 056309. (Visited on 09/06/2023).
- [146] L. L. Ji et al. “Radiation-Reaction Trapping of Electrons in Extreme Laser Fields”. In: *Physical Review Letters* 112.14 (Apr. 2014), p. 145003. (Visited on 09/07/2023).
- [147] Y He et al. “A Single-Laser Scheme for Observation of Linear Breit–Wheeler Electron–Positron Pair Creation”. In: *New Journal of Physics* 23.11 (Nov. 2021), p. 115005. (Visited on 10/02/2023).
- [148] *Laser System - Gemini*. <https://www.clf.stfc.ac.uk/Pages/Laser-system-Gemini.aspx#:~:text=Gemini%20is%20an%20extension%20of,carried%20out%20early%20in%202008>.
- [149] Fabien Quéré and Henri Vincenti. “Reflecting Petawatt Lasers off Relativistic Plasma Mirrors: A Realistic Path to the Schwinger Limit”. In: *High Power Laser Science and Engineering* (2021).
- [150] D. Batani et al. “Physics Issues for Shock Ignition”. In: *Nuclear Fusion* 54.5 (May 2014), p. 054009. (Visited on 09/18/2023).
- [151] P. Beiersdorfer et al. “Lineshape Spectroscopy with a Very High Resolution, Very High Signal-to-Noise Crystal Spectrometer”. In: *Review of Scientific Instruments* 87.6 (June 2016).
- [152] K U Akli et al. “A Dual Channel X-ray Spectrometer for Fast Ignition Research”. In: *Journal of Instrumentation* 5.07 (July 2010), P07008–P07008. (Visited on 09/18/2023).
- [153] G. Doumy et al. “Complete Characterization of a Plasma Mirror for the Production of High-Contrast Ultraintense Laser Pulses”. In: *Physical Review E* 69.2 (Feb. 2004), p. 026402. (Visited on 09/06/2023).
- [154] A. Bourdier. “Oblique Incidence of a Strong Electromagnetic Wave on a Cold Inhomogeneous Electron Plasma. Relativistic Effects”. In: *The Physics of Fluids* 26.7 (July 1983), pp. 1804–1807. (Visited on 09/29/2023).

- [155] A. Bourdier and S. Gond. “Dynamics of a Charged Particle in a Linearly Polarized Traveling Electromagnetic Wave”. In: *Physical Review E* 63.3 (Feb. 2001), p. 036609. (Visited on 09/29/2023).
- [156] A. P.L. Robinson, D. H. Kwon, and K. Lancaster. “Hole-Boring Radiation Pressure Acceleration with Two Ion Species”. In: *Plasma Physics and Controlled Fusion* 51.9 (2009).
- [157] K. T. McDonald and D. P. Russell. “Methods of Emittance Measurement”. In: *Frontiers of Particle Beams; Observation, Diagnosis and Correction*. Ed. by M. Month and S. Turner. Vol. 343. Berlin/Heidelberg: Springer-Verlag, 1989, pp. 122–132. (Visited on 08/31/2023).
- [158] Klaus Floettmann. “Some Basic Features of the Beam Emittance”. In: *Physical Review Special Topics - Accelerators and Beams* 6.3 (2003), pp. 80–86.
- [159] Wiedemann. *Particle Accelerator Physics*. New York, NY: Springer Berlin Heidelberg, 2015.